ABSTRACT

Title: **POLYMER-NANOPARTICLE COMPOSITES FOR APPLICATIONS IN FLEXIBLE ELECTRONICS**

Mert Vural, Ph.D., 2016

Directed By: **Professor Peter Kofinas, Fischell Department of Bioengineering**

The aim of this dissertation was to investigate flexible polymer-nanoparticle composites with unique magnetic and electrical properties. Toward this goal, two distinct projects were carried out. The first project explored the magneto-dielectric properties and morphology of flexible polymer-nanoparticle composites that possess high permeability (μ), high permittivity (ε) and minimal dielectric, and magnetic loss ($\tan \delta_{\varepsilon}$, $\tan \delta_{\mu}$). The main materials challenges were the synthesis of magnetic nanoparticle fillers displaying high saturation magnetization (M_s), limited coercivity, and their homogeneous dispersion in a polymeric matrix. Nanostructured magnetic fillers including polycrystalline iron core-shell nanoparticles, and constructively assembled superparamagnetic iron oxide nanoparticles were synthesized, and dispersed uniformly in an elastomer matrix to minimize conductive losses. The resulting composites have demonstrated promising permittivity (22.3), permeability (3), and sustained low dielectric (0.1), magnetic (0.4) loss for frequencies below 2 GHz. This study demonstrated nanocomposites with tunable magnetic resonance frequency, which can be used to develop compact and flexible radio frequency devices with high efficiency.

The second project focused on fundamental research regarding methods for the design of highly conductive polymer-nanoparticle composites that can maintain high electrical conductivity under tensile strain exceeding 100%. We investigated a simple solution spraying method to fabricate stretchable conductors based on elastomeric block copolymer fibers and silver nanoparticles. Silver nanoparticles were assembled both in and around block copolymer fibers forming interconnected dual nanoparticle networks, resulting in both in-fiber conductive pathways and additional conductive pathways on the outer surface of the fibers. Stretchable composites with conductivity values reaching 9000 S/cm maintained 56% of their initial conductivity after 500 cycles at 100% strain. The developed manufacturing method in this research could pave the way towards direct deposition of flexible electronic devices on any shaped substrate. The electrical and electromechanical properties of these dual silver nanoparticle network composites make them promising materials for the future construction of stretchable circuitry for displays, solar cells, antennas, and strain and tactility sensors.

POLYMER-NANOPARTICLE COMPOSITES FOR APPLICATIONS IN FLEXIBLE ELECTRONICS

By

Mert Vural

Dissertation submitted to the Faculty of the Graduate School of the
University of Maryland, College Park, in partial fulfillment
of the requirements for the degree of
Doctor of Philosophy
2016

Advisory Committee:
Professor Peter Kofinas, Chair
Associate Professor Sarah Bergbreiter
Professor Robert M. Briber
Associate Professor Isabel Lloyd
Professor Ichiro Takeuchi

Dedication

To my family, my parents Cantekin and Ruziye Vural, my uncle Mustafa Akkoyunlu, and Isabelle Coppens.

Acknowledgements

I would like to thank Dr. Peter Kofinas for the opportunities, support, and guidance that he provided during the course of my academic life in University of Maryland. I would also like to thank my committee members, for their time, advice, assistance, and counseling. I would like to acknowledge the time, effort, and help of Santiago, Daniel, Joseph, Dalton, and Nadjia, whom I have the opportunity to work in my research projects. I would like to thank my collaborators in Michigan State University and University of Strasbourg for their experimental and intellectual contributions. Finally, I would like to acknowledge members of the Kofinas and Briber labs past and present for their support, collaboration, and intellectual contributions.

Table of Contents

Table of Figures

Chapter 1: Introduction

The aim of this dissertation was to investigate flexible polymer-nanoparticle composites as functional dielectric and conductive materials. Toward this goal, two distinct projects were carried out. The first project focused on developing low loss magneto-dielectric materials with high permittivity (ε) and high permeability (μ) for applications in lightweight and compact radio frequency (RF) systems. The second project investigated highly conductive materials that sustain electrical conductivity under strain for applications in functional electronic devices including deformable circuits, and wearable strain sensors.

Resonant RF antennas and systems, which are commonly employed in hand-held devices, can be scaled down to smaller sizes by improving the propagation constant ($\beta \propto \sqrt{\varepsilon\mu}$) of their dielectric component.[1] The increased propagation constant originating from high ε and μ values results in a decrease in the size corresponding to antenna resonance. Accordingly, magneto-dielectric materials with high permeability, high permittivity, and low loss are required in RF systems to establish devices with smaller size.[1] An important materials approach to maximize the propagation constant with low loss is to employ polymer-nanoparticle composites. These composites effectively reduce conductive loss values by uniformly dispersing magnetic fillers in a polymer matrix.[1] However, current magneto-dielectrics consisting of polymer-nanoparticle composites have demonstrated limited μ and high magnetic loss, because of the low saturation magnetization (M_S) and high coercivity of the filler nanoparticles.[2-6] To establish fillers with high M_S, and limited magnetic anisotropy, we

performed studies on nanostructured iron and iron oxide based fillers in elastomer matrices. As an initial approach, superparamagnetic iron nano-fillers were coated with a protective shell layer consisting of citrate or silver to prevent oxidation of the core material with significant saturation magnetization and low coercivity. As a second approach, we studied raspberry-shaped superparamagnetic iron oxide nanoparticles with saturation magnetization values reaching bulk magnetization of magnetite and maghemite because of their collective assembly accessed by the oriented aggregation during synthesis. These fillers with high magnetization, and low anisotropy were dispersed uniformly in siloxane elastomers allowing us to demonstrate functional magneto-dielectrics with high permeability (3), high permittivity (22.3) and low electromagnetic loss for frequencies below 2 GHz.

The second focus of this dissertation was the investigation of conductive materials with the ability to maintain electrical conductivity under tensile strain. The performance of current stretchable electronic devices is defined by the stability of their electrical contacts under deformation.[7] In order to demonstrate strain-stable electrical contacts with high conductivity, we studied solution-processing methods to fabricate elastomeric fiber networks and to control nucleation and arrangement of silver nanoparticles in these fiber networks. This approach enabled a new fabrication method that allows direct deposition of conductive composites on the substrate of interest using solution-blow spinning to generate fibers, and spray coating to initiate and control nanoparticle nucleation. The resulting composites, couple a variety of electrical and electromechanical characteristics depending on their filler content and fabrication method. These composites can achieve high electrical conductivity values reaching

9000 S/cm ± 200 S/cm, which is sustained at 5100 ± 250 S/cm after 500 cycles at 100% strain. In addition, composites with lower filler content and limited in-fiber nanoparticle percolation maintain significant portion of their initial conductivity of 2000 ± 200 S/cm, after being stretched to 150% strain for 400 cycles.

1.1 Introduction to the Flexible Electronics

Contemporary advances in nanomaterials and their processing with soft materials has enabled the fabrication of flexible and stretchable electronic devices with performances nearing conventional rigid integrated circuits and electronic systems. The first study on flexible electronic devices involving a soft component was based on an organic transistor assembled on bendable films of polyethylene terephthalate.[8] The idea of a deformable soft substrate was followed by the use of microstructured or nanostructured composite electrodes with built-in strain.[9-14] This concept has resulted in electronic devices that can remain operational under more severe modes of deformation including stretching, twisting, and compression.[15-21] More importantly, recent studies on composites consisting of nanomaterials and polymers have demonstrated the possibility to combine desired electrical, magnetic, and electromagnetic properties in a single deformable material, which has enabled more versatile and cheap fabrication methods for deformable devices.[9, 22] In addition, refining the nanomaterial structure and composition in these composites has led to materials with better mechanical, electrical, and magnetic properties, and consequently improved device performance.[6, 11, 22-24]

Establishing control over structure and composition of fillers at the nanoscale is particularly important for developing flexible magneto-dielectric composites for RF

applications. Polymer-nanoparticle composites utilize magnetic nanoparticles with high saturation magnetization and low coercivity as filler material to achieve higher permeability without significantly increasing magnetic loss. These nanoparticles generally consist of iron or iron oxides with crystal sizes smaller than the size of a single magnetic domain to establish high saturation magnetization, and low coercivity.[25-29] However as the dimensions get smaller these particles become more susceptible to oxidation, which alters the structure and composition resulting in lower magnetization and higher magnetic anisotropy.[30, 31] As a result, it is extremely difficult to employ the full potential of magnetic nanoparticles in flexible magneto-dielectric composites.[3, 6, 28, 29, 32, 33]

Another significant limitation in flexible electronics stems from the change in electrical conductivity of conductive materials and composites during deformation. Electrical conductivity and stretchability are properties difficult to combine in a single solid material or composite, due to mechanisms that govern material deformation and electron transport.[34] For conductive solids, electrical conductivity is proportional to the number of delocalized (free) electrons and electron mobility, which is determined by the electronic band diagram and density of crystalline defects.[35] During macroscale stretching the band overlap between conduction and valence bands decreases and reduces the number of delocalized electrons, which leads to a drastic decrease in electrical conductivity.[35-37] In addition, tensile deformation can introduce defects that reduce the mobility of free electrons, and therefore electrical conductivity, due to increased electron scattering.[35] More importantly, these highly conductive solids with structural order are significantly more brittle than amorphous polymeric materials,

which can deform more than ten times of their initial dimensions. However, amorphous polymeric materials are well known insulators.

Conceptually, composite materials consisting of conductive nanomaterials and elastomers are ideal to generate highly conductive materials that can sustain electrical conductivity under tensile strain. An effective combination of conductive nanomaterial and elastomer can overcome the limited stretchability of conductive solids with the mechanical support provided by the elastomer matrix. Several approaches involving composite materials and structures were proposed to establish stretchable conductors including conductive nanowire, nanotube networks backfilled with elastomer, conductive networks of nanomaterials on prestrained substrates, and polymer-nanoparticle composites.[9-12, 32, 33, 38, 39] However, none of them has achieved satisfactory electromechanical properties, due to strain-induced stiffening effects becoming significantly more dominant with increasing nanomaterial concentration, which is necessary to establish high electrical conductivity.[13] Polymer-nanoparticle composites offer a potential platform to establish highly conductive materials that retain electrical properties under tensile deformation, as these composites promote generation of alternative conductive pathways under tensile strain.[38] The conductive pathways that fail upon deformation can be recovered by these alternative conductive pathways, which are different nanoparticle configurations formed during tensile strain.[29, 38] However, the electrical conductivity of polymer-nanoparticle hybrids is restricted by the higher percolation threshold of spherical nanoparticles.[40] To address this limitation, it has been recently demonstrated that a microstructured polymer fiber matrix can decrease the

percolation threshold and improve electrical conductivity of polymer-nanoparticle composites.[11]

1.2 Materials Research in Flexible Electronics

The concept of flexible electronics was established in 1967 without the help of soft materials.[41, 42] The flexibility of electronic devices was initially achieved using components or active materials thinner than 100 μm for assembling electronic devices.[41, 42] The first example was single-crystalline solar cells, which were fabricated using thinner active layers to improve their power/mass ratio for extra-terrestrial applications.[42] Flexible as a term can imply many different forms of deformation including bending, stretching, and twisting, yet these thin flexible electronic devices could only bend.[8, 41, 42] Recent studies have demonstrated flexible strain sensors and actuators, that can remain operational under strain values reaching 1200%.[43] These extremely robust devices were constructed using newly developed nanostructured materials, and mechanically supportive soft components, which sustain material properties and device geometry under excessive deformation.[11, 13, 38, 43] Nanomaterials commonly employed in flexible electronics include carbon nanotubes, graphene, graphene nanoribbons, conductive nanowires, nanoparticles, and magnetic nanowires and nanoparticles all of which induce unique properties and problems originating from nanoscale size effects.[7, 29] It is possible to classify these nanostructured composites as dielectrics, conductors, and semiconductors depending on their properties and utility in devices. In this dissertation, we will focus on specific materials challenges in stretchable

dielectrics, and conductors originating from structure and composition of nanomaterials and their composites, which will be discussed along this Chapter in detail.

1.2.1 Stretchable dielectrics

Fabrication of stretchable radio frequency (RF) antennas is an important challenge for stretchable electronics as a majority of the electronic devices use an RF antenna to link to data and information. Despite an obvious need, the development of stretchable antennas in compact form with performance similar to regular RF antennas has suffered fundamental hurdles. For instance, stretchable RF antennas require a stretchable dielectric material with high permittivity (ε) and permeability (μ) to improve the efficiency and decrease the size of the device. High performance stretchable magneto-dielectric materials can be accomplished using magnetic nano-fillers (nanoparticles) with high saturation magnetization and low anisotropy. These properties result in high permeability and low magnetic loss.[5, 6, 44] High permeability increases the scaling factor of RF antennas allowing fabrication of smaller devices. In addition, low magnetic loss leads to higher radiation efficiency, as the higher portion of the applied energy is converted to electromagnetic radiation. Therefore, it is desirable for a dielectric material of an RF antenna to have the highest possible permeability and lowest possible magnetic loss. Another important attribute is the interfacial coherence between the nanoparticles and the polymer matrix. Good adhesion between the nanoparticles and polymer matrix allows for higher nanoparticle loading, while maintaining the elasticity of the composite.[24, 27] In addition to high performance, stretchable magneto-dielectric composite RF antennas require robust stretchable electrodes to maintain electrical

contact under mechanical deformation.[11, 39, 45] Due to a limited available material spectrum, current state of the art stretchable antenna materials utilize flexible dielectric materials with low ε, μ and stretchable electrodes with decreasing electrical conductivity under strain, which leads to inefficient and bulky devices.[11, 39]

The most important material obstacle in magneto-dielectric composite research stems from limited control over the structure and composition of magnetic fillers. The efforts dedicated to achieve high permeability magneto-dielectric composites mostly employ iron-based nanofillers due to their high saturation magnetization and manageable anisotropy.[5, 6, 46, 47] Bulk iron (Fe), magnetite (Fe_3O_4), and maghemite (γ-Fe_2O_3) have saturation magnetization reaching 218 emu/g, 92 emu/g, 81 emu/g at room temperature, respectively.[25, 48, 49] Magnetic properties are known to be strongly affected by nanometer scaling.[48-50] The coercivity of particles decreases to zero, if the magnetic particle size is reduced below a critical limit ($D_{critical}$), for which the thermal energy is significant enough to rotate the magnetization vector out of the easy axis of the magnetic crystal (Figure 1.1a).[50, 51] However, it is hard to establish and maintain this superparamagnetic state in smaller dimensions, as each Fe-based filler is influenced by compositional changes or magnetization effects, which become more prominent at the nanoscale (Figure 1.1b).[25, 30, 48, 49, 52, 53]

Fe nanoparticles have great potential as magnetic fillers to establish magneto-dielectric composites with high permeability, due to the high saturation magnetization of bulk Fe. However, pure Fe is prone to oxidation under ambient conditions. In addition, the rate of oxidation increases drastically with decreasing Fe filler size.[25, 51] The oxidation of Fe results in fillers with lower saturation magnetization, and as a consequence magneto-

dielectric composites with lower permeability. Additionally, an oxide shell forming around the Fe core can potentially lead to unwanted magnetic interactions including exchange coupling, and surface canting effects.[25, 54-56]

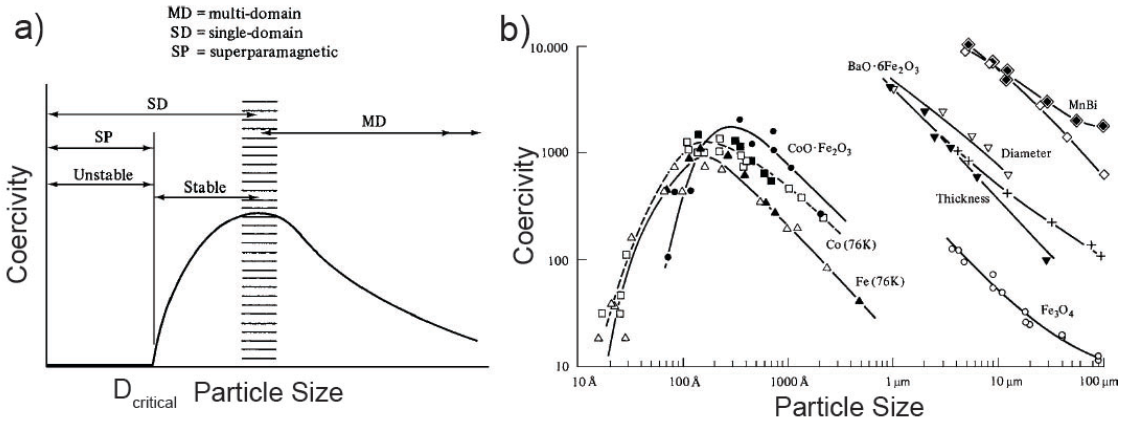

Figure 1.1 a) Schematic illustration of variation in coercivity with particle size. b) Experimental data highlighting the variation of coercivity with particle size.[50]

The coercivity values measured from passivated Fe particles with an oxide layer are much higher than the theoretically estimated coercivity values from anisotropy models.[25, 57, 58] The anisotropy of magnetic materials can be altered using structure and composition.[38, 57-59] For instance, Fe particles consisting of a metallic core and a magnetic oxide shell have demonstrated significant coercivity values, which decreased drastically after removal of the oxide shell.[51] This experiment has shown that magnetic interactions between the metallic core and oxide shell layer generates an exchange term in anisotropy, which needs to be considered with other energy terms when calculating the magnetization reversal of the oxide coated magnetic nanoparticles. It can be shown that if the magnetic shell orders ferrimagnetically or antiferromagnetically and exchange couples to the metallic core, this can potentially result in an increase in the energy required to rotate the magnetization in the nanoparticle.[57] The exchange

coupling between the core and the shell is a function of size, which defines the volumetric ratio of the core to shell.[57] As the shell gets thicker the magnetic crystal requires higher energies to rotate its magnetization.[51, 57]

The magnetic hysteresis experiments performed on Fe particles in nanoscale demonstrate effective anisotropy and coercivity values significantly higher than the bulk.[26, 57] In addition to exchange coupling another phenomenon resulting in higher anisotropy values is spin canting.[57] The oxide layer promotes formation of canted spins at the interface of the Fe core and oxide shell layer (Figure 1.2a).[59, 60] The canted spins also results in a decrease in magnetization values of the Fe particles.[57] Similar to exchange coupling, an increase in the thickness of the oxide layer results in a drastic increase in the influence of spin canting on magnetic properties.[60]

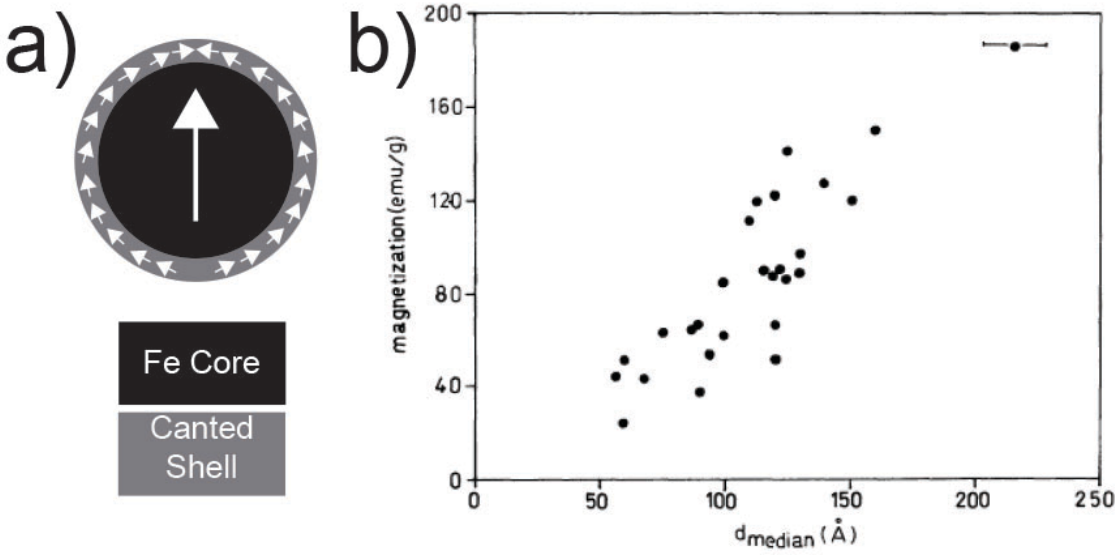

Figure 1.2 a) Illustration of spin canting in nanoparticles. b) Correlation between particle dimensions and magnetization values.[57]

The saturation magnetization of Fe nanoparticles decreases significantly with increasing oxide shell layer thickness.[51, 60] This effect becomes more influential as the particle size decreases, due to an increase in volume ratio of the oxide shell to Fe core (Figure 1.2b).[51, 57] These interactions can lead to a decrease in magnetization and an increase in magnetic anisotropy of the Fe fillers, which results in adverse effects in the performance of magneto-dielectric composites.[2, 44] Another important issue is the synthesis of superparamagnetic Fe nanoparticles that generally involves high temperature, high-pressure thermolysis in oil-based reaction systems.[30, 31, 44] These reactions utilize flammable, and toxic reagents under extreme conditions, which can potentially result in an explosion, and high-energy consumption. Moreover, such reactions are impractical for composite research as they yield nanoparticles in the order of milligrams per synthesis.

Iron oxides are also considered promising magnetic fillers for magneto-dielectric polymer/nanoparticle composites, despite having poor magnetization in nanoparticle form. Magnetic nanoparticles of magnetite exhibit magnetization values significantly lower than the bulk saturation magnetization of 92 emu/g, as a result of surface spin canting, stoichiometric impurities and crystal size effects.[61] There have been several reports that minimize the influence of such effects using complicated synthesis mechanisms to establish control over stoichiometry, and minimize defect formation in superparamagnetic nanoparticles, but these approaches are only able to achieve a saturation magnetization of 82 emu/g.[61, 62] These methods have failed to prevent formation of a more saturated oxide layer at the interface, which resulted in magnetization values lower than the bulk magnetization due to surface spin canting.[63, 64]

Additionally, inter-particle magnetic interactions governed by particle size and particle-to-particle distance can also alter the magnetic properties of iron oxides.[48]

It has been recently demonstrated that maghemite (Fe_2O_3) nanoparticles can approach bulk magnetization values through the formation of a common crystalline orientation at the interface between nanoparticles (collective assembly).[65] This approach has demonstrated small maghemite crystallites with same crystallographic orientation that can coalesce to form nanostructures with high saturation magnetization without increasing the anisotropy. Another important study has revealed this cluster-like structure helps preventing growth of saturated oxide layers on these iron oxide nanostructures.[66] In addition, oriented aggregation of iron oxide nanocrystals can improve structural and magnetic order by preventing volume, surface spin canting.[64, 66, 67]

1.2.2 Stretchable conductors

Stretchable electronic devices consist of stretchable circuitry, and complementary flexible active materials embedded on this stretchable circuit.[15, 17, 18, 68] For efficient operation of stretchable electronic devices it is necessary for stretchable circuits to maintain high electrical conductivity under deformation.[15, 17, 22, 39, 45] However, it is challenging to establish stretchable circuits using a single material with metallic conductivity. Large scale deformation decreases the number of delocalized electrons and electron mobility for materials with metallic conductivity, due to reduced band overlap and increased number of defects.[35-37] These deformation-mediated effects result in a decrease in electrical conductivity. Also, conductive materials are extremely brittle,

since structural order is essential to establish high electrical conductivity.[34, 35] As a consequence of these limitations, composites consisting of a deformable conductive component and an elastomer component were investigated to produce stretchable conductor materials. The deformable conductive components are materials and structures developed to sustain high electrical conductivity under deformation. The elastomer component of the composite enables elastic deformation of the conductive component and the composite. All stretchable conductors are composite materials, yet each approach shows different electrical and mechanical properties.

To clarify the origin of this variability in properties, it is useful to classify stretchable conductors based on the methods of fabrication. Stretchable conductors consist of liquid metal filled microfluidics, lithographically patterned buckled and fractal electrodes, and composites consisting of interconnected conductive nanomaterials and elastomers. Liquid metal filled microfluidics employ soft microfluidic channels to establish circuit designs or patterns. The conductive component is a liquid metal such as Hg or gallium-based alloys.[39, 69-73] These microstructured channels filled with liquid metal sustain electrical conductivity under strain until the mechanical failure of elastomer microfluidic enclosure.[72, 73] The most significant problem involved with these stretchable conductors is electrical failure of the circuit due to a defective site allowing liquid metal to leak out from the soft enclosure. Another important consideration is poor inherent mechanical properties of the liquid metal component, which makes the system more prone to plastic deformation. In summary, these electromechanically promising constructs are more susceptible to mechanical and electrical failure than other approaches that were employed to fabricate stretchable conductors.[29]

Stretchable conductors fabricated using lithographically patterned buckled or fractal conductive structures on stretchable substrates are commonly employed to demonstrate new conceptual electronic devices to highlight the potential of flexible electronics.[15, 17, 19, 20, 68, 74-76] The most striking advantage of this approach is the lithography based fabrication method, which allows easy and precise implementation of active electronic components including diodes, transistors, batteries onto stretchable circuits.[19, 20, 68] These lithographically processed stretchable conductors consist of conductive microstructures assembled using prestrained substrates and fractal geometries. Prestrained substrates are used to generate buckled electrodes by depositing thin linear conductive lines on stretched substrates as these lines bend to a buckled state once the substrate is released.[68] The electrical conductivity is maintained in these constructs until the tensile deformation reaches the prestrain value of the stretched substrate.[68, 77, 78] It is extremely challenging to establish isotropic stretchable conductors using stretched substrates since each mode of deformation requires specific prestrain conditions and conductive lines to mediate respective mode of deformation.[77] Moreover, the drastic difference in Young's modulus of conductive lines and stretchable substrate causes accumulation of a stress field at the interface between the substrate and conductive lines.[78, 79] This results in delamination of the buckled conductive lines from the stretchable substrate.[79] The conductive lines of a stretchable circuit can also be fabricated with a built-in strain using network patterns known as "fractal geometries".[76] Fractal geometries consist of subdivisions with a unit matching the structure of the entire construct. These self-similar geometries can be engineered to withstand a certain amount of tensile strain without deforming plastically.[19, 76] Additionally, these fractal

geometries can be designed to operate under uniaxial, biaxial, and radial deformation, which provides control over isotropic properties of the stretchable electrodes.[76] However, the highest achieved strain for stretchable conductors fabricated using metallic fractal geometries is 75%, which is relatively small deformation in comparison to levels of deformation allowed by composites consisting of interconnected conductive nanomaterials and elastomers.[76] Another important drawback of lithographically processed stretchable circuits is cost, as they need to go through many expensive processing steps for deposition, and patterning. These steps are followed by the subsequent transfer of the circuit from a brittle substrate to a stretchable substrate, which leads to adhesion and alignment problems.[29]

Stretchable conductive composites composed of conductive filler materials, and elastomeric polymer matrix have been studied to construct circuits and devices with strain-stable electrical properties.[9, 10, 12, 13, 32, 33, 38, 45] Metal microparticles, nanoparticles, nanowires, and carbon nanotubes are the most common fillers employed to fabricate stretchable conductive composites. The early stretchable conductors were fabricated by dispersing these nanofillers in an elastomeric matrix. Their electromechanical properties are governed by percolation theory, which effectively describes the interconnectivity of randomly distributed fillers in polymer matrix.[29, 40, 80] The electrical contact between conductive materials in a polymer matrix is determined by the volume fraction of the fillers in polymer:

$$\sigma = \sigma_0 (V_f - V_C)^S \quad (1)$$

The unit σ represents the electrical conductivity of the composite material, σ_o corresponds to the intrinsic conductivity of the filler, S is defined as critical exponent related to structure of the filler, V_f is the filler fraction, and V_c is the percolation threshold to establish interconnectivity between fillers. The electrical current travels along the conductive pathways generated by the interconnected filler network. The structure of the conductive filler is extremely important to determine the percolation threshold, and S factor. Theoretical percolation thresholds for randomly distributed spherical particle, plate, and wire or tube shaped nanofillers are:

$$V_c^{plate} = \frac{\pi D^3}{6(D + D_{IP})^3} \tag{2}$$

$$V_c^{plate} = \frac{27\pi D^2 t}{4(D + D_{IP})^3} \tag{3}$$

$$V_c^{tube} = \frac{\xi \varepsilon_{volume}(\pi D^3/6)}{(D + D_{IP})^3} + \frac{(1-\xi)27\pi D^2 l}{4(l + D_{IP})^3} \approx \frac{\xi \varepsilon_{volume}\pi}{6} + \frac{(1-\xi)27\pi D^2}{4l^2} \tag{4}$$

D represents the diameter of spherical particles, lateral diameter of plates, diameter of wires or outer diameter of tubes; t is the thickness of nanoplates, l is the length of wires or tubes, ξ is the volume fraction of agglomerated nanotubes or wires and ε_{volume} is the volume of agglomerated tubes or wires. D_{IP} corresponds to the critical distance for particle to particle separation for effective electron tunneling, which is typically accepted as 10 nm.[40, 81] This model accurately interprets the influence of changes in filler material geometry on percolation threshold.[29, 40] For instance, the percolation

threshold of spherical nanoparticles increases with increasing diameter (Figure 1.3a, b)).[40] On the contrary the percolation threshold of nanoplates decreases with increasing spherical plate diameter (Figure 1.3c, d).[40]

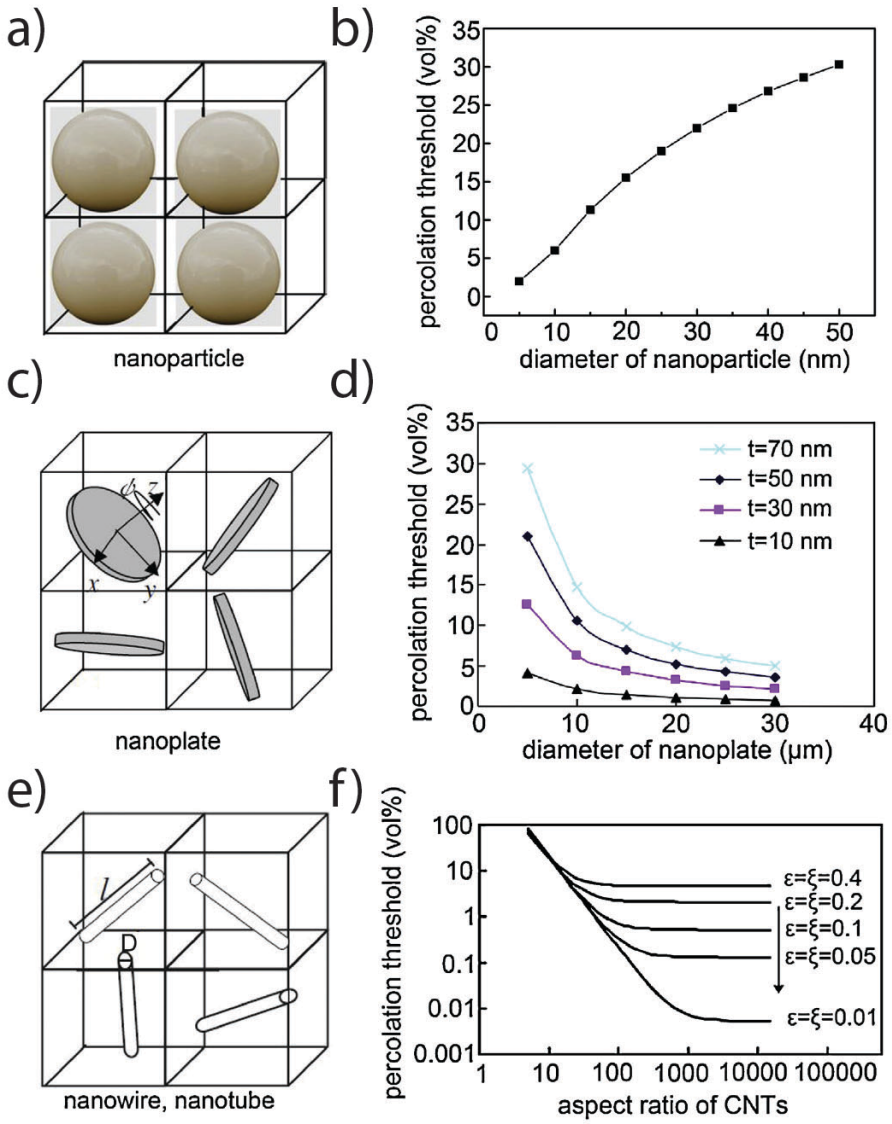

Figure 1.3 Illustration of a) nanoparticles, c) plates, and d) wires placed in a unit cell assuming random distribution of fillers in 3D polymer matrix. Calculated percolation thresholds with respect to b) diameter of nanoparticles, c) diameter, and thickness of plates, and f) aspect ratio, dispersion state of wires or tubes.[40]

The high aspect ratio of one-dimensional nanomaterials makes the effect of D_{IP} negligible, if the aggregation of the fillers is small (ξ=0.01) (Figure 1.3e, f).[80] But highly agglomerated systems increase the percolation threshold drastically, which overpowers the influence of aspect ratio (Figure 1.3e, f).[80] These graphs clearly demonstrates that one-dimensional filler geometries can establish conductive pathways with less filler concentration, which makes metallic nanowires and carbon nanotubes one of the most common filler materials employed to fabricate stretchable conductors.[9, 10, 22, 32, 33, 45] However, composites consisting of one-dimensional filler materials demonstrate more drastic stiffening under strain values, which deteriorate the elastic properties of the composite leading to poor cyclic performance under deformation.[29, 82, 83] In contrast, spherical nanoparticles has more freedom to reorganize themselves in the polymer matrix during mechanical deformation, which impedes the rate of stiffening in composites during deformation in exchange for lower electrical conductivity.[11, 13, 38, 84] These phenomena cast light on the trade-off between stretchability and conductivity of the stretchable conductive composites.[28, 29, 34] Researchers has proposed various approaches to achieve composites with high electrical conductivity, that can be sustained during excessive tensile deformation. The most effective composites employ network structures established using the filler material[10] or the polymer matrix.[11, 84] The network structure governs deformation of composite at early strain values, in which the filler-to-filler distance remains unchanged. When strain values exceed the built-in strain introduced by the network structure, the interconnectivity of the fillers is then determined by percolation theory similar to stretchable conductive composites without

any network structure.[11, 84] This approach can yield highly conductive composites that maintain electrical conductivity under tensile deformation exceeding 100% strain.

1.3 Outline of this Dissertation

The first part of this dissertation focuses on the search for flexible polymer-nanoparticle composites with high propagation constant and low loss at microwave frequencies. The initial studies summarized in Chapter 2 were performed on composites consisting of nanostructured core-shell iron/citrate and iron/silver nanoparticles in elastomer matrices. The results of this work have been published in *Journal of Materials Chemistry C* under the title "Nanostructured Flexible Magneto-dielectrics for Radio Frequency Applications."[85]

The second study on flexible magneto-dielectric materials, presented in Chapter 3, investigated composites with raspberry-shaped iron oxide nanoparticle (RSN) fillers. This work characterized the microstructure, composition, and magnetic properties of raspberry-shaped iron oxide fillers, and electromagnetic properties of their polymer composites. The materials characterization revealed that iron oxide RSN fillers composed of aggregated small nanocrystals with common crystallographic orientation displayed higher saturation magnetization compared to individual iron oxide nanoparticles with coercivity limited below 300 Oe. This resulted in magneto-dielectric composites with permeability values reaching 2.3 and magnetic loss values limited below 0.4 for frequencies up to 1 GHz. In addition, the alteration of iron oxide composition between maghemite and magnetite produced a change in the magnetic resonance of composites.

The second part of this dissertation focuses on stretchable polymer-nanoparticle composites to establish conductive materials that sustain electrical conductivity under tensile deformation. In Chapter 4, we studied solution-processing techniques to generate elastomeric fiber networks and to facilitate controlled nucleation of silver nanoparticles on these fiber networks. The results of this study were published in ACS Nano under the title "Sprayable Elastic Conductors Based on Block Copolymer Silver Nanoparticle Composites."[86]

In Chapter 5, we have investigated solution-processed stretchable conductive fiber mats with high filler concentration, and therefore high electrical conductivity. In order to establish high filler concentration, we dispersed silver nanoparticles in a solution of SIS. Solution blow spinning this mixture yielded composite fiber templates for the initiation of the secondary silver nanoparticle nucleation. The resulting composites have demonstrated electrical conductivity reaching 9000 S/cm that only decreases to 4900 S/cm after 500 cycles of 100% strain. Energy dissipation and electron microscopy studies were performed on these composites to identify the structural changes during deformation, which govern their electromechanical properties. These studies showed that conductive fiber networks sustained high electrical conductivity between large blocks of polymer-nanoparticle composites, which are separated during mechanical deformation.

In Chapter 6, we provided an outlook for this dissertation and highlighted potential future directions for polymer-nanoparticle research regarding functional magneto-dielectric materials and elastic conductors. In the final chapter, a brief summary of the

contributions of this work to materials research in flexible electronics is provided to demonstrate the accomplishments of this research.

Chapter 2: Nanostructured Flexible Magneto-dielectrics for RF Applications

2.1 Introduction

Hybrid materials with high magnetic permeability (μ) and dielectric permittivity (ε) known as magneto-dielectric materials are essential for the development of high efficiency microwave electronic devices and their miniaturization.[1] Polymer-magnetic nanoparticle composites have promise as magneto-dielectric hybrids, due to their low magnetic and dielectric loss, mechanical flexibility, and ease of processability. The polymer matrix prevents particle aggregation, reducing conductivity losses, and provides mechanical flexibility. Magnetic nanoparticles dispersed in a polymer matrix contribute to the permeability and permittivity of the magneto-dielectric composite.[5]

The permeability of polymer-magnetic nanoparticle composites is limited by magnetic resonance frequency (f_{res}) and saturation magnetization (M_s) of the magnetic nanoparticles through the Snoek Limit.[87] The permeability drops significantly for frequencies above f_{res}. For this reason polymer composites containing MnZn and NiZn ferrites or similar materials with high permeability, yet low f_{res} have found limited application in microwave electronics.[88] Additionally, materials with low M_s such as iron oxides cannot achieve sufficient permeability to be utilized for microwave device miniaturization.[5, 89]

The dielectric and magnetic loss of magneto-dielectric composites are important properties that need to be minimized in order to improve the efficiency of microwave electronic devices. Dielectric losses mostly originate from eddy currents generated in

the material. The eddy current generation in polymer-magnetic nanoparticle composites can be reduced by decreasing the size of nanoparticles below a critical dimension (skin depth).[3] It is possible to increase the skin depth of the hybrid material by decreasing the conductivity originating from the percolation of magnetic nanoparticles.[90] As a consequence low conductivity leads to low dielectric loss. The coercivity (H_c) of magnetic nanoparticles induces magnetic losses in polymer-magnetic nanoparticle composites.[91] Magnetic losses can be reduced without sacrificing any magnetization by the use of superparamagnetic nanoparticles. However, it is quite challenging to synthesize superparamagnetic nanoparticles with high M_s. Magnetic materials with high M_s such as ferromagnetic iron cannot maintain their magnetization at dimensions smaller than the critical superparamagnetic size because of excessive oxidation.[30, 31] Polymer-magnetic nanoparticle composites reported in literature consist of either oxidized superparamagnetic nanoparticles with no coercivity and low M_s resulting in low μ, or high M_s ferromagnetic nanoparticles with substantial coercivity leading to high magnetic loss.[5, 44, 89, 92]

In this work, we report on the fabrication of two sets of flexible magneto-dielectric composites with low magnetic and dielectric loss. This is achieved by the dispersion of high M_s, low coercivity air-stable iron (Fe) nanoparticles and iron/silver (Fe/Ag) heterostructures in polydimethylsiloxane (PDMS) matrices. The magneto-dielectric composites made of air-stable Fe/citrate nanoparticles can be adapted to the fabrication of broadband RF antennas, since they possess high μ (3), while maintaining low magnetic (0.29) and dielectric (0.051) loss.[24] Additionally, Fe/citrate nanoparticle composites are shape compliant, allowing tensile elongation up to 15% strain before

failure. Fe/Ag heterostructures formed by thermal annealing of Fe/Ag core-shell nanoparticles were dispersed in PDMS to fabricate magneto-dielectric composites with high μ (2.25) and ε (22.3), but low magnetic (0.24) and dielectric (0.09) loss, which makes them suitable for RF antenna miniaturization.[1, 93] The Fe/Ag heterostructure composites are able to deform plastically under tensile elongation up to 70% strain.

2.2 Experimental

2.2.1 Synthesis of air-stable Fe/citrate nanoparticles

Fe/citrate nanoparticles were synthesized at room temperature from $FeSO_4$ using $NaBH_4$ as the reducing agent. $FeSO_4 \cdot 7H_2O$ (10mmol) and trisodium citrate dihydrate (2mmol) were dissolved in 2.5 L deionized water. The mixture was stirred with a magnetic stirrer for 5 minutes, then $NaBH_4$ (20mmol) was added to the mixture to initiate nanoparticle nucleation. The mixture was allowed to react for 20 minutes, and the nanoparticles were extracted using a rare-earth magnet for sedimentation. The particles were washed with ethanol 10 times, then vacuum dried and stored at atmospheric conditions.

2.2.2 Synthesis of Fe/Ag core-shell nanoparticles and heterostructures

Fe/Ag core-shell nanoparticles were synthesized at room temperature using a similar method. In this procedure Fe/citrate nanoparticles were reacted for 5 minutes instead of 20 minutes, then an aqueous $AgNO_3$ (7ml, 0.5M) solution was injected into the reaction. The mixture was allowed to stir for 20 minutes, and the core-shell

nanoparticles were collected using magnet sedimentation. The collected particles were washed with ethanol 10 times then vacuum dried. The Fe/Ag core-shell nanoparticles were annealed at 600°C under flow of reducing gas (Argon/Hydrogen (95%, 5%)) for 1 hour to form a heterostructure of Fe/Ag core-shell nanoparticle aggregates with a coherent interface. The resulting Fe/Ag heterostructures were kept under atmospheric conditions.

2.2.3 Preparation of flexible magneto-dielectric composites

PDMS (Sylgard 184, Dow Corning) was prepared by mixing base silicone polymer with a curing agent in a 10:1 weight ratio. Dry Fe/citrate nanoparticles or Fe/Ag heterostructures were mixed in the polymer at the desired nanoparticle loading. The polymer particle mixture was poured into a mold, placed in a vacuum desiccator for 30 minutes to remove air bubbles, and cured at 100°C for 4 hours.

2.2.4 Characterization

Transmission Electron Microscope (TEM) (JEOL 2100F), Powder X-Ray Diffraction (XRD)(Bruker C2 Discover-Source: Cu-Kα (λ=0.154nm)) and X-ray photoelectron spectrometer (Kratos Axis 165, Al Kα (1486.6 eV)) were used for structural and elemental characterization of the nanoparticles via imaging, Energy Dispersive X-Ray Spectroscopy (EDS), Selected Area Electron Diffraction (SAED), Powder Diffraction and X-ray Photoelectron Spectroscopy (XPS). Vibrating Sample Magnetometer (VSM; Lakeshore 7400 series) was used to characterize the magnetic properties of the nanoparticles. Dynamic Mechanical Analysis (TA Instruments Q800) was used to

characterize the mechanical properties of the polymer nanoparticle composites. The magneto-dielectric properties of the composites were determined using an Agilent RF impedance/material analyzer (E4991A).

2.3 Results and Discussion

The TEM images and SAED patterns of air-stable Fe/citrate, Fe/Ag core-shell nanoparticles and Fe/Ag heterostructures are presented in Figure 2.1. The air-stable Fe/citrate nanoparticles capped with citrate developed a very thin oxide shell, which helps prevent further oxidation of the Fe core along with the citrate capping layer (Figure 2.1a). The average particle size for the air-stable Fe/citrate nanoparticles was measured to be 100 nm with a standard deviation of 19 nm (100 ± 19 nm). The Fe/Ag core-shell nanoparticles also have an oxide layer similar to the Fe/citrate nanoparticles, which separates the Fe core from the shell layer consisting of Ag nanoparticles (Figure 2.1b). The average diameter for the Fe/Ag core-shell nanoparticles was 120 ± 23 nm, which is slightly higher than the Fe/citrate nanoparticles because of the additional Ag nanoparticles covering the Fe core. The Fe/Ag heterostructures consist of aggregates of Fe/Ag core-shell nanoparticles with the Ag shell layer forming a coherent interface upon annealing at 600°C as illustrated in Figure 2.1c. In addition to TEM, SAED was used to identify the crystalline structure of each sample.

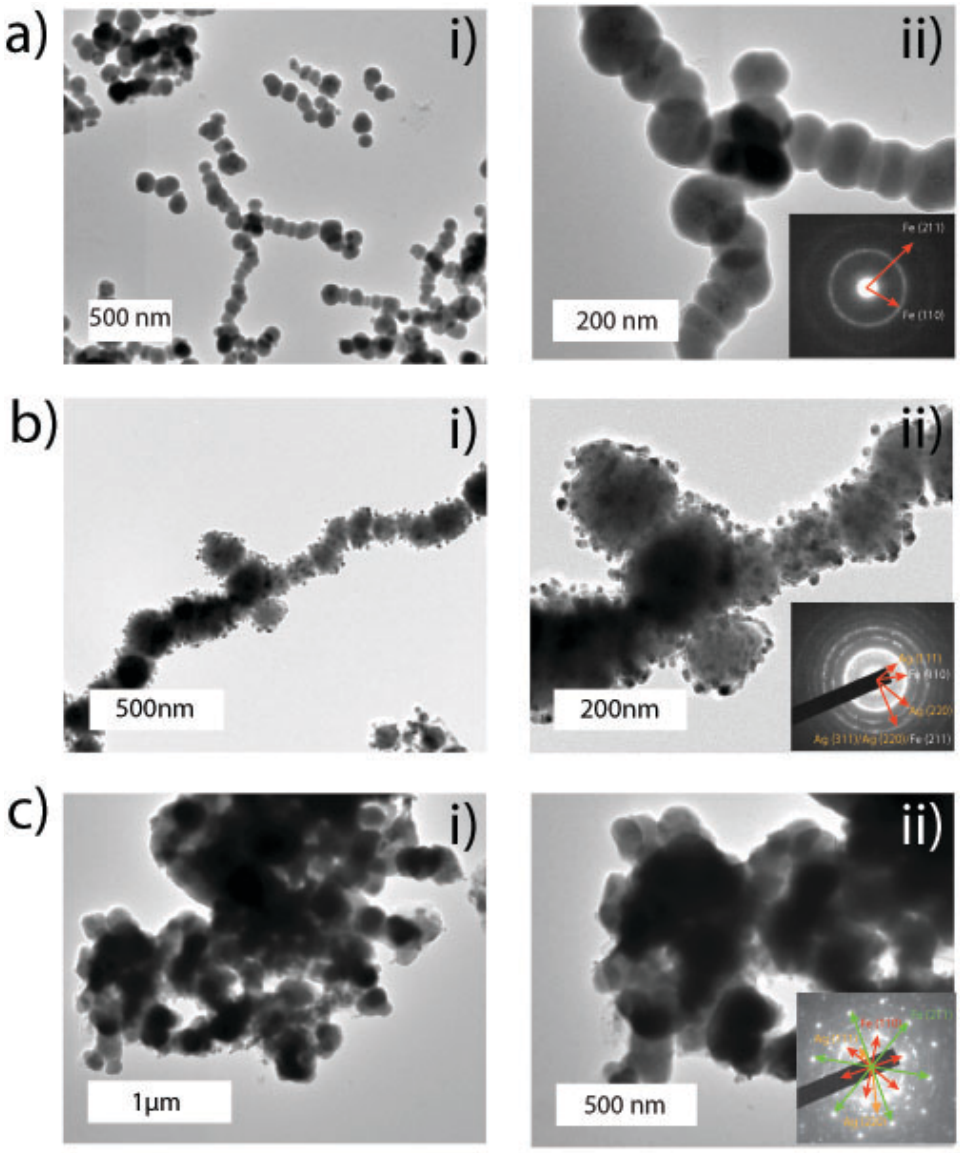

Figure 2.1 TEM images of a) Fe/citrate nanoparticles, b) Fe/Ag core-shell nanoparticles, and c) Fe/Ag heterostructures. The SAED characterization of each particle is placed as an inset.

The SAED pattern of Fe/citrate nanoparticles indicates a microstructure of polycrystalline body centered cubic (bcc) Fe with Debye rings that correspond to crystallographic planes Fe (110) and Fe (211) (Figure 2.1a(ii)-inset). The SAED pattern of Fe/Ag core-shell nanoparticles is an overlay of the polycrystalline bcc Fe pattern on

the polycrystalline Ag pattern (Figure 2.1b(ii)-inset). The Debye rings that represent the crystallographic planes in polycrystalline microstructure of Fe core and Ag shell are shown as an inset in Figure 2.1b(ii). The crystalline structure of Fe/Ag core-shell nanoparticles changed significantly after thermal annealing under reducing gas flow. The crystal size of Ag shell increased after annealing, as inferred by the discontinuous Debye rings of Ag crystalline planes in the SAED pattern of the Fe/Ag heterostructure (Figure 2.1c(ii)-inset). The SAED pattern of the Fe/Ag heterostructure shows Laue diffraction patterns representing Fe crystalline planes instead of Debye rings. This indicates a significant increase in crystal size for the Fe core (Figure 2.1c(ii)-inset).

The average crystal size of the Fe in nanoparticles and heterostructures is an important structural parameter for the characterization and tunability of the magnetic properties (M_s, H_c) for both nanoparticles and heterostructures. Crystals below the critical superparamagnetic to ferromagnetic transition size of 10 nm for Fe result in zero coercivity.[25] However, further reducing the crystal size below the critical transition size leads to a decrease in M_s.[25] Powder X-Ray Diffraction (XRD) was utilized to identify the crystalline structure and crystal size of Fe in each material (Figure 2.2). The average crystal size of Fe in nanoparticles and heterostructures was determined from the diffraction peak of Fe (110) plane using Scherrer's Equation.[94] The XRD data indicates that the core of the nanoparticles consist of polycrystalline iron with an average crystal size of 5 nm for both Fe/citrate nanoparticles and Fe/Ag core-shell nanoparticles. Consistent with SAED patterns, the peaks of the Fe planes become sharper after annealing, which indicates an increase in crystal size. The average crystal size of Fe for

the Fe/Ag heterostructures calculated from XRD data is 9.6 nm, which confirms the increase in crystal size with annealing (Figure 2.2).

The chemical composition of nanoparticles and heterostructures is equally important as the morphology for the displayed magnetic properties. Characterization of chemical composition for each nanoparticle and heterostructure was performed using localized EDS. XPS was used to characterize surface compositions of nanoparticles and heterostructures.

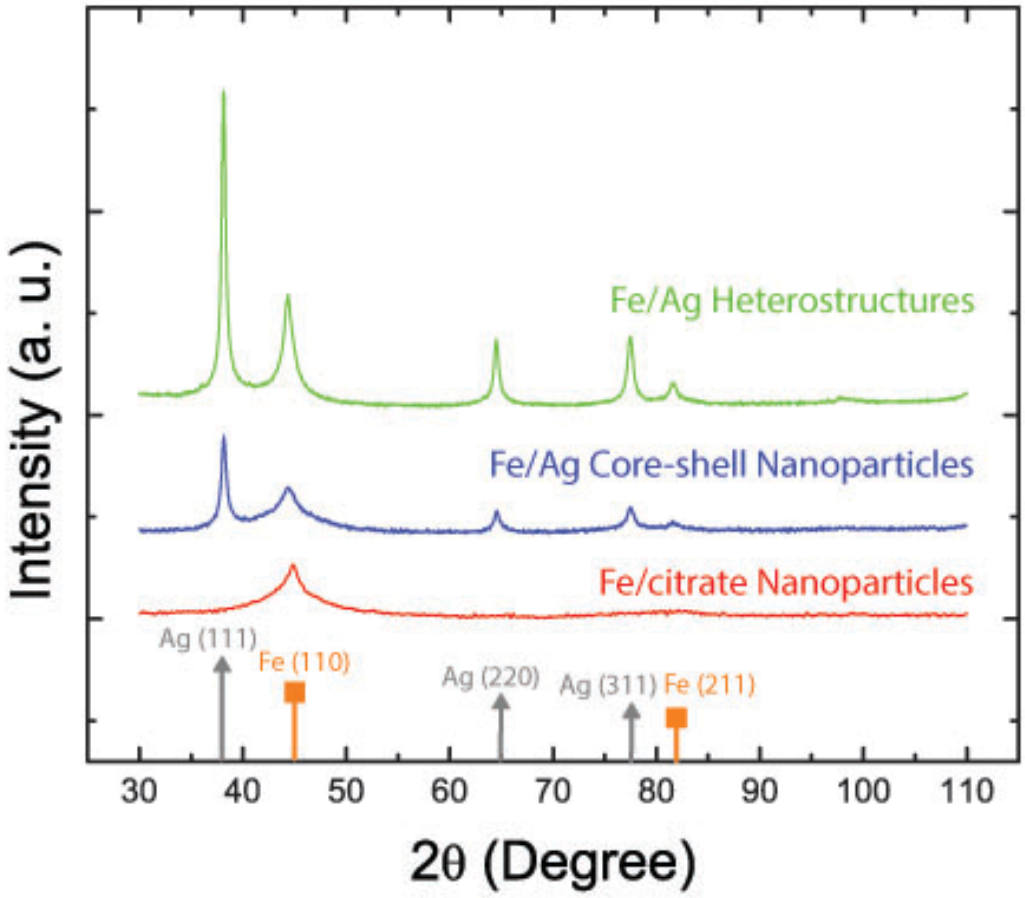

Figure 2.2 Powder X-Ray Diffraction data of Fe/citrate nanoparticles, Fe/Ag core-shell nanoparticles, and Fe/Ag heterostructures.

The STEM images and corresponding elemental EDS map for each nanoparticle and heterostructure are presented in Figure 2.3. The elemental EDS map of Fe/citrate nanoparticles shows a thin oxide layer covering the surface of the Fe core (Figure 2.3a). The oxide layer remains stable after being stored under ambient conditions at room temperature for 6 months (Figure A.1b). Upon annealing Fe/citrate nanoparticles with an analogous procedure for Fe/Ag core-shell nanoparticle annealing, the stable oxide layer grew thicker (Figure A.1b). The elemental EDS map of Fe/Ag core-shell shows a discontinuous shell layer formed by Ag nanoparticles around the Fe core prior to annealing (Figure 2.3b), consistent with the TEM images (Figure 2.1b). However, the EDS map does not indicate a distinct oxide shell (Figure 2.3b). After thermal annealing, the Fe/Ag core-shell nanoparticles form a heterostructure with an Ag shell with better coverage, as illustrated in the elemental EDS map (Figure 2.3c). The EDS map of the Fe/Ag heterostructure shows no obvious signs of oxidation at the surface. The characterization of the surface chemical composition of nanoparticles and heterostructures using XPS reveals the state of oxidation for Fe at the interface between the Fe core and shell layers (Figure 2.4). The XPS data agrees well with EDS for Fe/citrate nanoparticles where both indicate the existence of an oxide layer covering the Fe core (Figure 2.4a-inset). The oxide layer apparent at TEM images of Fe/Ag core-shell nanoparticles (Figure 2.1b) was confirmed by XPS (Figure 2.4b-inset). The oxide layer was identified as Fe_2O_3 from the satellite peak appearing at 718.8 eV for both Fe and Fe/Ag core-shell nanoparticles (Figure 2.4(a,b)).[95] The XPS data also indicates the existence of elemental Fe represented by the peak located at 706.7 eV (Figure 2(a, b)-inset). The existence of elemental Fe confirms that the oxide layer is as thin as the

limited mean free path of X-rays.[96]

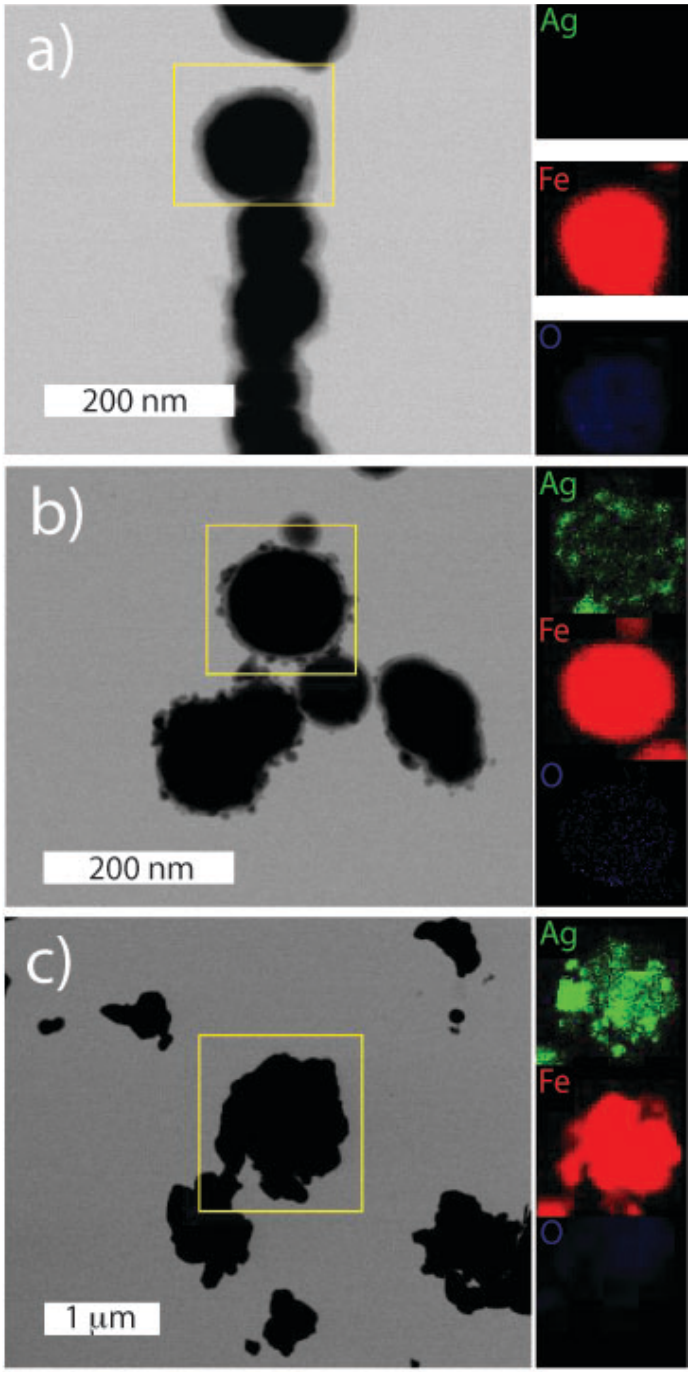

Figure 2.3 Scanning Transmission Electron Microscope (STEM) image and EDS elemental map of a) Fe/citrate nanoparticles, b) Fe/Ag core-shell nanoparticles, and c) Fe/Ag heterostructures.

The XPS data of Fe/Ag heterostructures shows that the state of oxidation and thickness of the oxide layer has changed after annealing (Figure 2.4c). The oxide layer of Fe_2O_3 became Fe_3O_4 after annealing, which can be inferred by the absence of the satellite peak at 718.8 eV (Figure 2.4c-inset). Additionally, the elemental Fe peak became more prominent relative to the oxide related peaks ($Fe(3p_{1/2})$, $Fe(3p_{3/2})$), indicating that the oxide layer becomes thinner after annealing (Figure 2.4c-inset). The change in oxidation state and oxide layer thickness after annealing is consistent with previously reported Fe nanoparticles that were annealed in reducing ambient.[97] The magnetic characterization correlates well with both the morphology and chemical composition of the nanoparticles and heterostructures. The Fe/citrate nanoparticles demonstrated significant M_s (144 emu/g), and high coercivity (420 Oe) (Figure 2.5a). The Fe/Ag core-shell nanoparticles have a lower M_s (98 emu/g) than the Fe/citrate nanoparticles, due to the non-magnetic shell layer of Ag. The coercivity of Fe/Ag core-shell nanoparticles (210 Oe) is smaller than for Fe/citrate nanoparticles because the increase in size of the nanoparticle, reduces the influence of surface anisotropy.[98] The Fe/Ag heterostructures exhibit a higher M_s (120 emu/g) as compared to Fe/Ag core-shell nanoparticles (98 emu/g) due to the increase in average Fe crystal size and decrease in oxide layer thickness after annealing (Figure 2.5a).[44] The increase in Fe crystal size did not build additional coercivity because the average crystal size remained below the critical dimension for superparamagnetic to ferromagnetic transition. Moreover, the shape anisotropy became even less significant for Fe/Ag heterostructures since the size increased significantly as the Fe/Ag core-shell nanoparticles aggregate (Figure 2.1c). As a result, the coercivity of Fe/Ag heterostructures decreased to 58 Oe (Figure 2.5a).

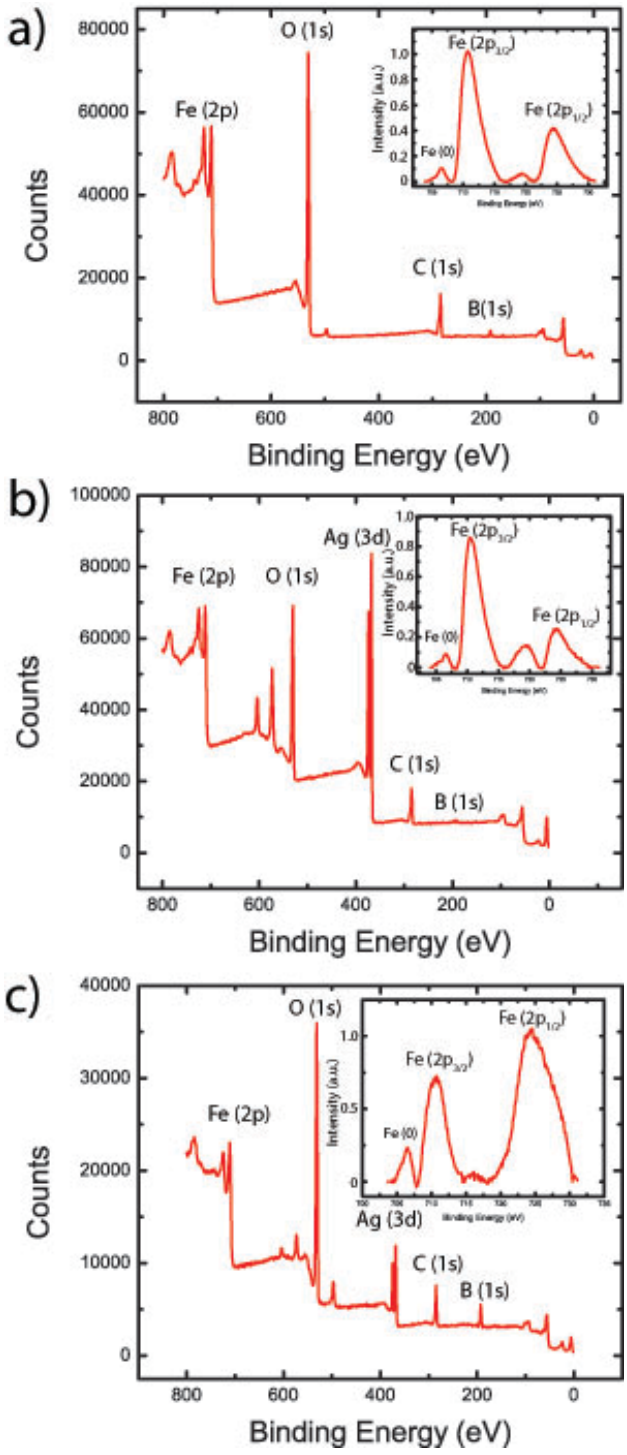

Figure 2.4 XPS spectrum of a) Fe/citrate nanoparticles, b) Fe/Ag core-shell nanoparticles, and c) Fe/Ag heterostructures. Localized XPS spectra around Fe2p region is given as inset.

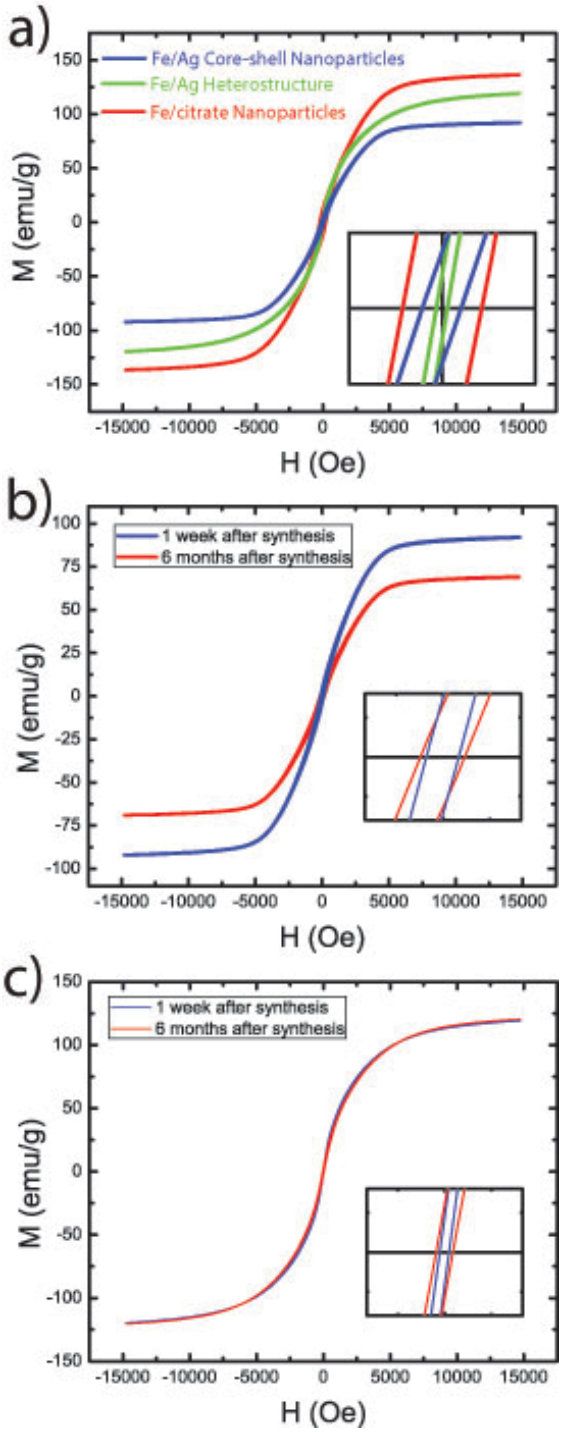

Figure 2.5 a) Room temperature magnetic hysteresis curves for Fe/citrate nanoparticles, Fe/Ag core-shell nanoparticles, and Fe/Ag heterostructures as synthesized. Time dependent magnetic hysteresis curves for b) Fe/Ag core-shell nanoparticles, and c) Fe/Ag heterostructures. The low-field magnetization curve is given as an inset.

The magnetic properties of Fe/Ag core-shell nanoparticles and Fe/Ag heterostructures were evaluated after 6 months, in order to assess the stability of the nanoparticles (Figure 2.5b, c). The M_s of the Fe/Ag core-shell nanoparticle were decreased by 24% as a result of oxidation (Figure 2.5b), which was confirmed by EDS studies (Figure A.2). The coercivity decreased slightly to 200 Oe. The magnetic properties of Fe/Ag heterostructures remained stable over the same period (Figure 2.5c).

The Fe/citrate nanoparticles and Fe/Ag heterostructures were dispersed in a PDMS matrix and cured to form flexible magneto-dielectric composites. The mechanical stress-strain curve for each polymer/nanoparticle composite is presented in Figure 2.6. The Young's modulus of Fe/citrate nanoparticle (1.75 MPa) and Fe/Ag heterostructure (0.79 MPa) composites with nanoparticle loading of 50 wt% is higher than the modulus of the pure PDMS elastomer (0.56 MPa), indicating good adhesion between nanoparticles and the PDMS matrix (Figure 2.6a).[99] Both Fe/citrate nanoparticles and Fe/Ag heterostructure composites with 50 wt% nanoparticle loading exhibit 120% tensile elongation at break (Figure 2.6a). The composites made of Fe/citrate nanoparticles with 75 wt% nanoparticle loading can deform elastically until failure at 15% strain (Figure 6B). On the other hand composites made of Fe/Ag heterostructure composites with 75 wt% nanoparticle loading can deform plastically until failure at a strain of 70% (Figure 2.6b). The Young's modulus of the composites increases with increasing nanoparticle loading; up to 11.1 MPa and 3.3 MPa for Fe/citrate nanoparticle and Fe/Ag heterostructure composites at 75 wt% nanoparticle loading, respectively.

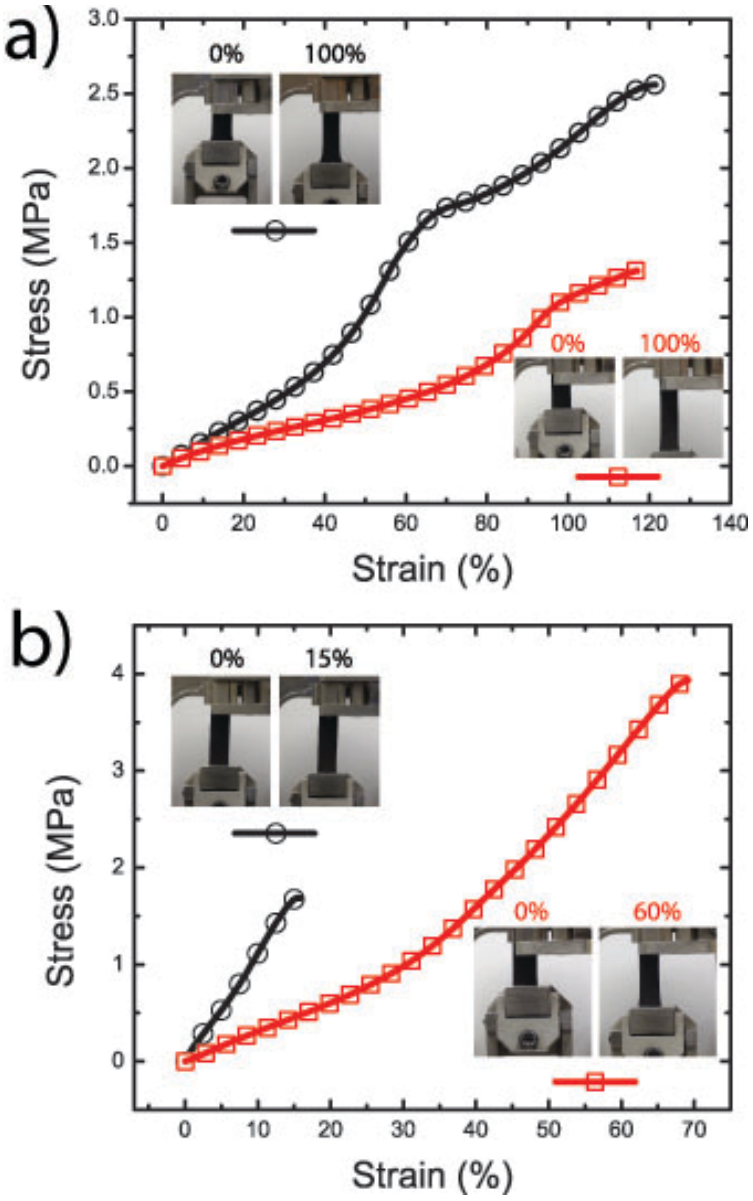

Figure 2.6 Mechanical Stress/Strain curves for Fe/citrate (circles) and Fe/Ag (squares) heterostructure polymer composites with a) 50 wt% and b) 75 wt% nanoparticle loading. The images of elongated composites are given as inset.

The electromagnetic constants (μ, ε) and loss characteristics of both Fe/citrate nanoparticle and Fe/Ag heterostructure composites were measured at a frequency range of 1 MHz to 8 GHz. The ε dispersion relation for composites of Fe/citrate nanoparticles and Fe/Ag heterostructures with 50 wt% nanoparticle loading was flat at this frequency

range with no sign of dielectric resonance or relaxation that could lead to additional dielectric loss ($\tan\delta_\varepsilon = \varepsilon``/\varepsilon`$) (Figure 2.7a). Due to the Ag shell, the ε values of Fe/Ag heterostructure composite (8) is higher than ε of the Fe/citrate nanoparticle composite (4.2) with the same nanoparticle loading of 50 wt%. The dielectric loss values remain low up to a frequency of 3 GHz for both Fe/citrate nanoparticle (0.04) and Fe/Ag heterostructure (0.06) composites with nanoparticle loadings of 50 wt% (Figure 2.7b).

The dielectric loss value of Fe/Ag heterostructure composites increases drastically above 3 GHz due to conductivity losses introduced by the Ag shell. The μ and magnetic loss ($\tan\delta_\mu = \mu``/\mu`$) dispersion relation shows a magnetic relaxation starting at 2.25 GHz for the composites with 50 wt% nanoparticle loading (Figure 2.7a, b). The μ values for both Fe/citrate nanoparticle and Fe/Ag heterostructure composites are promising for RF device fabrication, reaching 1.83 and 1.55 at 1.8 GHz, respectively (Figure 2.7a). The magnetic loss is significantly lower for Fe/citrate nanoparticle (0.06) composites and Fe/Ag heterostructure (0.07) composites at 1.8 GHz (Figure 2.7b). The magnetic loss increases more drastically for Fe/citrate nanoparticle composites at higher frequencies, which is possibly due to hysteresis losses and the influence of the Ag shell on magnetic relaxation by altering interparticle interactions (Figure 2.7b).[100]

The ε and dielectric loss values of the Fe/citrate nanoparticle composite with 75 wt% nanoparticle loading are stable from 1 MHz to 8 GHz (Figure 2.7c, d). However, the ε and dielectric loss dispersion relation of the Fe/Ag heterostructure composite with 75 wt% nanoparticle loading indicate a dielectric relaxation at 4.4 GHz, due to

aggregation of the Fe/Ag heterostructure with increased concentration (Figure 2.7c, d).[101] As a result ε values decrease and the dielectric loss increases significantly for frequencies reaching 4.4 GHz. Even though the dielectric relaxation decreases ε and increases dielectric loss of the Fe/Ag heterostructure composites, they still possess high ε (22.3) and low dielectric loss (0.09) up to 3 GHz.

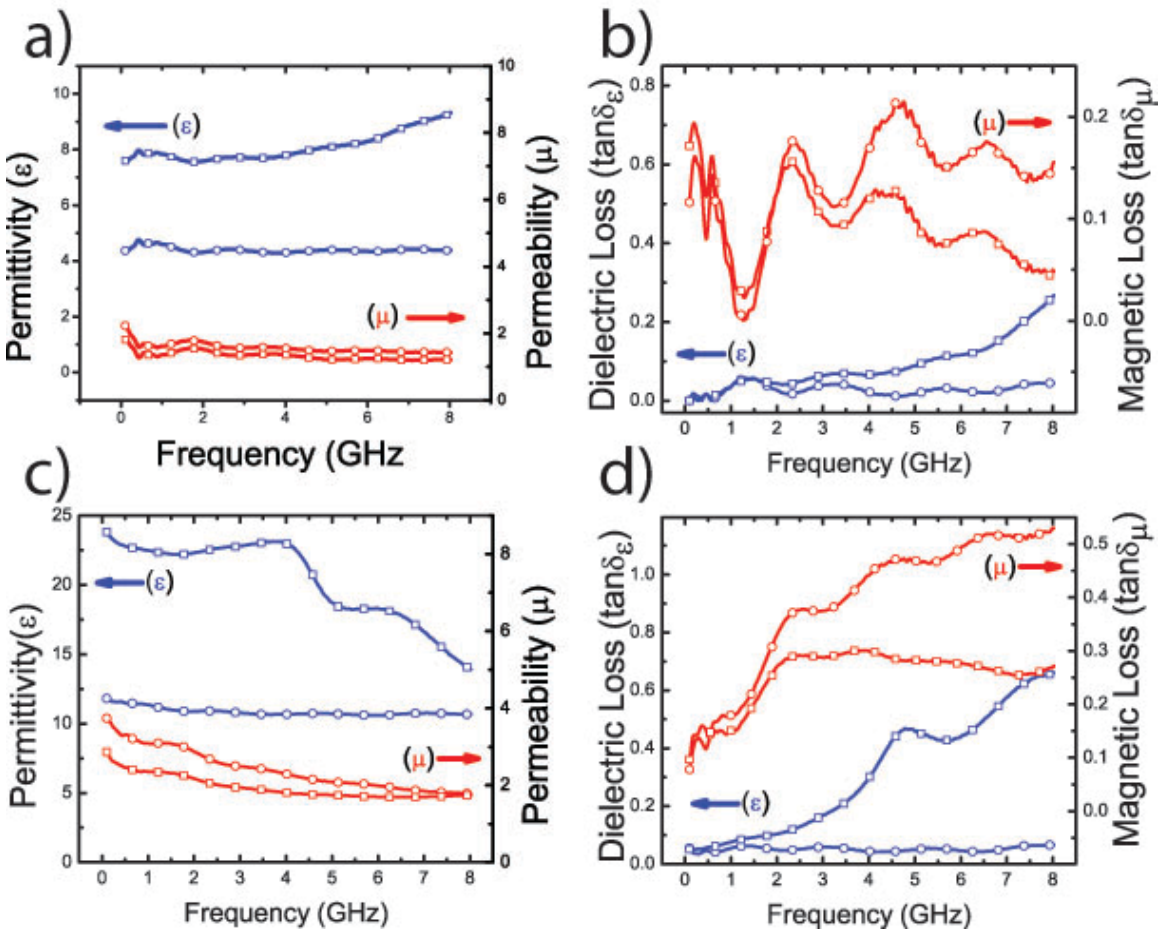

Figure 2.7 a) Dielectric (ε), Magnetic Permeability (μ) dispersion and b) dielectric and magnetic loss values of Fe/citrate (circles) and Fe/Ag heterostructure (squares) composites with 50 wt% nanoparticle loading. c) Dielectric (ε), Magnetic Permeability (μ) dispersion and d) dielectric and magnetic loss values of Fe/citrate (circles) and Fe/Ag heterostructure (squares) composites with 75 wt% nanoparticle loading.

The μ and magnetic loss dispersion relation of composites with 75wt% nanoparticle loading indicates a magnetic relaxation centered at 2.25 GHz similar to composites with 50 wt% nanoparticle loading (Figure 2.7c, d). However, both Fe/citrate nanoparticle and Fe/Ag heterostructures have high μ and low magnetic loss values for frequencies lower than the magnetic relaxation frequency of 2.25 GHz. The Fe/citrate nanoparticle composites with 75 wt% nanoparticle loading have μ and magnetic loss values of 3 and 0.29 at 1.8 GHz, respectively. The Fe/Ag heterostructure composites with 75 wt% nanoparticle loading have a μ of 2.15 and magnetic loss of 0.24 at 1.8 GHz. The magnetic loss remains stable for frequencies beyond the magnetic relaxation for Fe/Ag heterostructure composites unlike Fe/citrate nanoparticle composites, which tend to have higher magnetic loss with increasing frequency (Figure 2.7d). As the particles get more densely packed with increasing concentration, the influence of the Ag shell as a spacer becomes more influential compared to coercivity effects, thus fixing the magnetic loss of Fe/Ag heterostructures at 0.24 beyond 2.25 GHz.[100] Flexible RF antennas have been fabricated using Fe/citrate nanoparticle and Fe/Ag heterostructure composites that operates at frequencies of 1.7 GHz and 1.9 GHz, respectively (Figure A.3). The flexible magneto-dielectric composites fabricated using Fe/citrate nanoparticles reduced the size of the RF antenna operating at 1.7 GHz by 44%. The Fe/Ag heterostructure composite has scaled down the size of the RF antenna with an operation frequency of 1.9 GHz by 38%.

2.4 Conclusions

We have fabricated elastic magneto-dielectric composites with low loss by embedding high M_s, low H_c, air-stable magnetic nanoparticles and heterostructures in an elastomer matrix (PDMS). Fe/citrate nanoparticles and Fe/Ag heterostructures have demonstrated good adhesion with the PDMS matrix. As a result the composites with 50 wt% nanoparticle loading remain flexible up to a tensile elongation of 120%. These composites demonstrated promising ε and μ values with low dielectric and magnetic loss, while still maintaining their flexibility. The utilization of magnetic nanoparticles with appropriate crystal size, while still protecting the magnetic core against oxidation, provide a substantial advantage regarding ε, μ, loss values, and tunability of material properties for various applications in the field of RF communication devices. The composites have reduced the size of RF patch antennas as much as 44%. We believe this simple, yet effective method for designing and processing magneto-dielectric materials with different functionalities can have application in the construction of various communication devices for flexible RF electronics.

Chapter 3: Stretchable Magneto-dielectric Composites Based on Raspberry-Shaped Iron Oxide Nanostructures

3.1 Introduction

Nanostructured polymer-nanoparticle composites have been widely used as conductive and dielectric materials for applications in flexible electronics.[11, 85, 86, 102-104] In particular dielectric polymer-nanoparticle composites with high dielectric constant (ε) and permeability (μ) with low dielectric and magnetic loss show promise in the future development of flexible and compact radio frequency (RF) devices.[3, 5, 6, 44, 85] These composites referred to as flexible magneto-dielectrics utilize magnetic nanoparticle fillers to achieve high permeability and permittivity, while the polymer matrix provides mechanical elasticity, robustness, and separation between nanoparticles to prevent formation of conductive losses.[3-6, 44, 47, 85, 105]

The magnetic properties of the dispersed nanoparticles have significant influence on the frequency dependent electromagnetic properties of magneto-dielectric composites.[106] The permeability of a magneto-dielectric composite is directly proportional to the saturation magnetization of the nanoparticles.[106] Additionally, incorporating nanoparticles with higher magnetic anisotropy in composites results in materials with increased magnetic loss.[106, 107] Another important consideration is the magnetic resonance frequency of the composites, which is determined by the magnetic resonance frequency of the nanoparticles.[107] The permeability of the composite reaches a maximum at its resonance frequency, and decreases significantly for frequencies beyond the magnetic resonance, which is governed by the Snoek's limit.[87] The optimal

magneto-dielectric composite for high efficiency RF devices thus contains magnetic nanoparticles with high saturation magnetization, low coercivity, and tunable magnetic resonance frequency.

Iron oxide materials such as magnetite Fe_3O_4 and its oxidized form, maghemite γ-Fe_2O_3 show promise as magnetic fillers for large scale magneto-dielectric polymer-nanoparticle composite production, because of their low manufacturing cost, high bulk saturation magnetization (M_s), and size dependent coercivity.[48, 108] Additionally, it is possible to adjust the magnetic resonance of the iron oxides by tuning the structure and composition.[107, 109] However, iron oxide fillers prepared as nanoparticles to minimize coercivity exhibit magnetization values significantly lower than their bulk M_s, as a result of stoichiometric impurities and defects.[26, 49, 63, 64] Thus, it is extremely difficult to obtain composites with high μ values, and low magnetic loss using iron oxide nanoparticles.[5, 6, 109] However due to the progress in synthesis methods of nanomaterials, it was possible to enhance the limited magnetic properties of magnetite nanoparticles by synthesizing nanostructures consisting of oriented aggregates of iron oxide nanocrystals.[46, 52, 65-67, 110] These nanostructures are composed of nanocrystals with common crystallographic orientations combined together to form nanoclusters. Such nanostructures are generally synthesized using polyol methods,[52, 67, 110-112] and may display mean size ranging from tenth of nanometers to 800 nm and nanocrystal size between 5 to 20 nm by tuning reaction condition parameters; Depending on their synthesis parameter, they may display a cavity resulting in raspberry-shaped nanostructures (RSNs).[25, 30, 32-35] Their nanostructuration leads to collective magnetization effects, which allows these nanostructures to nearly match the M_s of bulk

magnetite without significantly increasing the magnetic anisotropy of the material.[46, 52, 67, 110]

In this work, we demonstrate a stretchable magneto-dielectric composite with high permeability, low magnetic and dielectric loss, and adjustable magnetic resonance frequency by using iron oxide RSNs as the filler material. Iron oxide RSNs form oriented aggregates/clusters of magnetic nanocrystals with high M_s and low coercivity, which improves the permeability of the composites without significantly increasing their magnetic loss. In addition to beneficial magnetic characteristics, iron oxide RSNs can be assembled from nanoparticles with different phases of magnetic iron oxide, which have distinct natural magnetic resonance. This hybrid structure enables fabrication of composites with different magnetic resonance frequency, which is determined by the nature of the major iron oxide composition of the RSNs.

The iron oxide RSNs have been synthesized by a one-pot modified polyol solvothermal method.[66] The reaction time was used to alter the structure, composition and magnetic properties of the filler iron oxide RSNs. The solvothermal syntheses with reaction periods of 7 and 13 hours, result in spherical hollow clusters with a similar mean size around 250 nm and constituted of iron oxide nanocrystals with a mean nanocrystal size of 5 and 25 nm, respectively. The smaller crystal size particles consist mostly of maghemite (γ-Fe_2O_3), while the larger crystal size particles have a magnetite (Fe_3O_4) rich composition. Both types of RSNs have been chemically functionalized with a citrate-capping agent to favor their dispersion in polydimethylsiloxane (PDMS) matrix. The citrate capped RSNs with different composition and structure were dispersed in PDMS matrix, which was subsequently cross-linked to form magnetite- and

maghemite-rich magneto-dielectric composites. The magnetite- and maghemite-rich magneto-dielectric composites could be stretched up to 155%. Additionally, both composites have demonstrated permeability values exceeding 2 with loss values remaining below 0.1 below the magnetic resonance frequency. The maghemite-rich magneto-dielectric composites have a magnetic resonance centered at 480 MHz. On the other hand, magnetite-rich composites have demonstrated a magnetic resonance slightly higher than 1 GHz. The difference in magnetic resonance frequency of the composites is potentially originating from the different composition of the filler materials, as the experimental magnetic resonance frequency of the composites were found to be close to the theoretical natural magnetic resonance of the dominant iron oxide phase in their filler material.

3.2 Experimental

3.2.1 Materials

Hexahydrate iron (III) chloride ($FeCl_3$, $6H_2O$), urea and ethylene glycol were purchased from Alfa Aesar with purity of 97%, 99.3% and 99%, respectively. Succinic acid (SA) was purchased from Sigma-Aldrich with a purity of ≥99.5%. Sylgard 184 of Dow Corning was used as the uncured polydimethylsiloxane (PDMS) matrix.

3.2.2 Synthesis of raspberry nanostructures

In a typical synthesis $FeCl_3$, $6H_2O$ (30 mmol), succinic acid (10 mmol) and urea (300 mmol) were completely dissolved in ethylene glycol (300 ml) by vigorous mechanical stirring and sonication. The solution was sealed in a Teflon lined stainless steel autoclave (600 mL capacity), slowly heated at 200°C at 1.5°C/min and kept at this temperature for 7 or 13 hours. The autoclave was cooled down to room temperature afterwards by water circulation during 1 h. The powders were separated by centrifugation and washed 3 times with ethanol and 3 times with deionized water to eliminate organic and inorganic impurities. Finally, the powders were freeze-dried to remove water and a black powder was obtained (1500 mg). The synthesis was also scaled up and performed in larger autoclave (2 L) to produce up to 20 g of material.

3.2.3 Citrate functionalization of raspberry nanostructures (RSN)

RSNs were coated with citrate molecules using a procedure previously reported.[116] A 250 ml buffer solution (pH 5) of citric acid (0.14 $mol.l^{-1}$) and potassium citrate (0.26 $mol.l^{-1}$) was prepared. Then, RSNs (1.5 g) were immersed in the solution and stirred for 1 hour to promote the nanoparticle surface coating. After stirring, the RSNs were extracted and washed once by centrifugation with deionized water to remove any excess of citric acid. Finally, the powders were freeze-dried to remove water.

3.2.4 Fabrication of magneto-dielectric composites

PDMS (Sylgard 184, Dow Corning) was prepared by mixing base silicone polymer with a curing agent in a 10:1 weight ratio. Dry RSNs were mixed in the polymer at the desired nanoparticle loading. The polymer particle mixture was poured into a mold, placed in a vacuum desiccator for 30 minutes to remove air bubbles, and cured at 100 °C for 4 hours.

3.2.5 Characterization

Sizes, morphologies and crystal structures were characterized by scanning electron microscopy (SEM) with a JEOL 6700F (point resolution 2 nm), a transmission electron microscopy (TEM) with a JEOL ARM200F microscope operating at 200 kV (point resolution 0.18 nm) and a JEOL 2100F electron microscope working with a 200 kV accelerating voltage equipped with a GATAN GIF 200 electron imaging filter. Selected area electron diffraction (SAED) was performed using a JEOL ARM200F microscope.

Dried powders were placed in a platinum crucible. Specific surface areas of the different samples were determined by N_2 adsorption-desorption measurements at 77 K by using a Micromeritics TriStar 3000 apparatus. Before the measurements, samples were outgassed at 150 °C overnight in order to desorb impurities or moisture from their surface.

Global magnetic measurements were recorded with a Superconducting Quantum Interface Device (SQUID) magnetometer (Quantum Design MPMS-XL 5) and Vibrating Scanning Magnetometer (VSM; Lakeshore 7400 series).

The magneto-dielectric properties of the composites were determined using an Agilent RF impedance/material analyzer (E4991A).

3.3 Results and discussions

The citrate capped RSN filler materials with different structure and composition have been synthesized following a modified polyol solvothermal approach, described in the experimental section.[66] The structure and composition of these filler materials were altered by modulating the reaction time. The structure of the RSNs fillers prepared using two reaction durations was characterized with X-Ray diffraction, Mössbauer spectroscopy and electron microscopies.[66] The scanning electron microscopy (SEM) images revealed that both RSN fillers have an average diameter of about 250 nm (Figure 3.1a, b). The surface roughness apparent in SEM images is indicative of a cluster-like structure. The transmission electron microscopy (TEM) characterization has demonstrated that these nanoclusters possess a hollow core, which validates the raspberry-like shape of this filler material (Figure 3.1a-inset, d). High-resolution TEM (HRTEM) images of the interface between two crystals in these RSN filler materials (Figure 3.2) and selected area electron diffraction (SAED) patterns (Figure 3.1e, f) confirm the oriented attachment of nanocrystals in RSNs. Indeed the HRTEM images clearly demonstrate that crystallographic orientations of nanocrystals are matched at the interface, which is indicative of a common crystal orientation shared by nanocrystals forming the RSN fillers (Figure 3.2). SAED patterns verified the formation of the spinel phase (Figure 3.1e, f) and are consistent with single crystal structures (SAED patterns on single RSNs show Von Laue patterns instead of Debye rings). These observations

show that RSNs are constituted of aggregated nanocrystals, which have similar crystallographic orientations.[46, 52, 67]

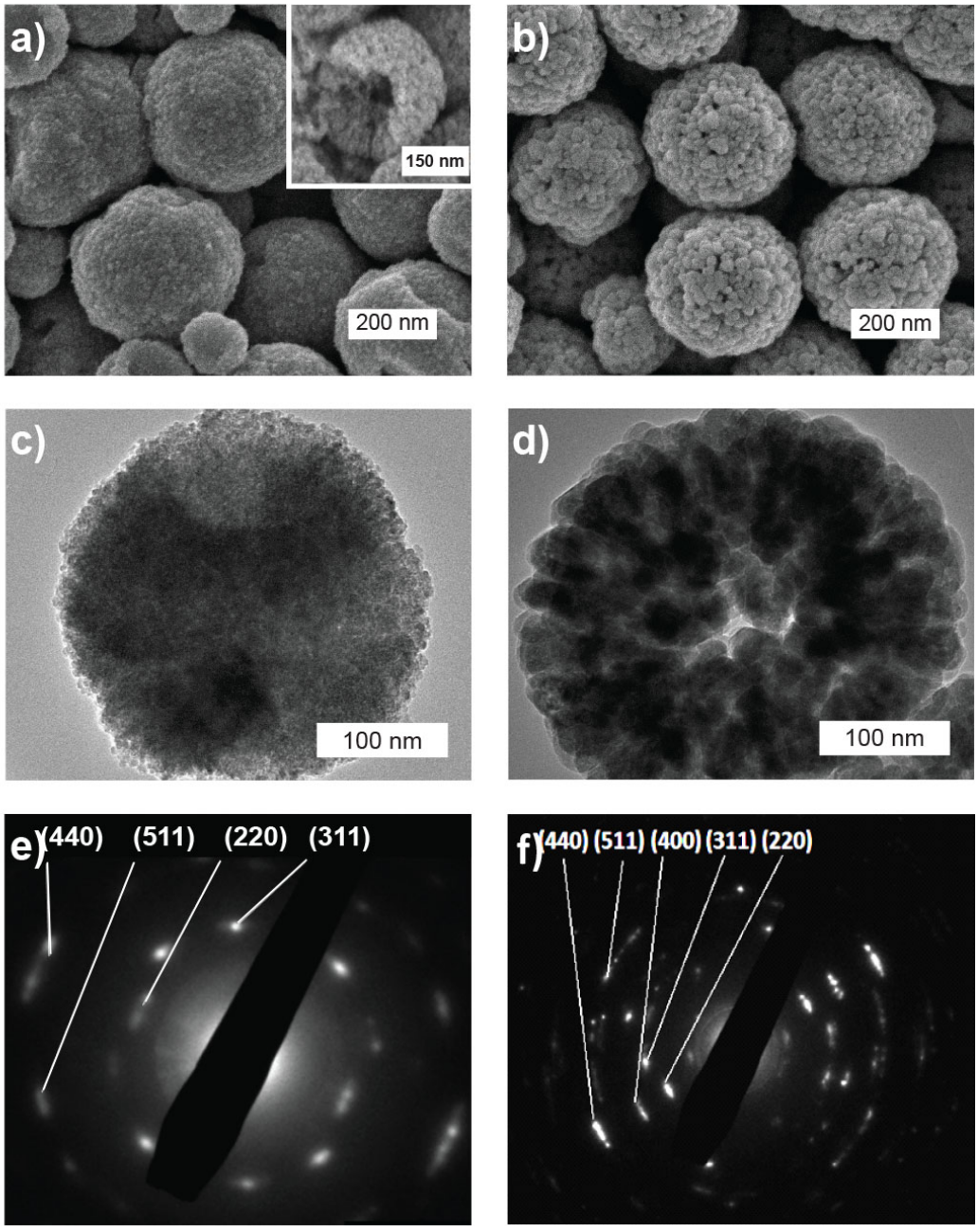

Figure 3.1 SEM images of citrate-capped RSNs reacted for a) 7 hours, and b) 13 hours. TEM images of citrate-capped RSNs reacted for c) 7 hours, and d) 13 hours. SAED patterns of citrate-capped RSNs reacted for e) 7 hours, and f) 13 hours. The high resolution SEM image of citrate-capped RSN reacted for 7 hours is given as an inset.

The detailed characterization of the RSNs microstructure has showed that RSN fillers allowed to react for 7 hours (RSN5) have finer nanocrystal size than fillers allowed to react for 13 hours (RSN25) (Figure 3.1). From TEM micrographs, a mean nanocrystal size of 5 and 25 nm is determined for RSN5 and RSN25 respectively while crystallite sizes calculated from Rietveld analysis of X-Ray Diffraction (XRD) patterns (Figure 3.2b) are respectively 14 ± 1 and 15 ± 1 nm. Such discrepancies between both measurements were related to the monocrystalline nature of the RSNs and the presence of defects or dislocation induced during the synthesis process. Indeed SAED patterns (Figure 3.1.e, f) and HRTEM of nanocrystal interfaces (Figure 3.2a) confirms the monocrystalline structure of RSNs, which is established with aggregates of nanocrystals with similar crystal orientations. However, the extended Von Laue spots in SAED patterns evidenced a slight misalignment in the orientation of these nanocrystals. In addition, Fast Fourier Transform (FFT) analysis performed on SAED patterns of RSNs has demonstrated the presence of defects.[66] XRD patterns of RSNs display characteristic peaks of the iron oxide spinel structure (Figure 3.2b). Lattice parameter deduced from XRD pattern is very close to that of stoichiometric magnetite for RSN25 and indicates an oxidized state for RSN5. In addition, Mössbauer spectroscopy confirmed that RSN fillers with smaller crystal size have a maghemite-rich composition ($Fe_{2.78}O_4$, 70% (vol/vol) of maghemite) while those with large crystal size are mainly constituted of magnetite Fe_3O_4 phase ($Fe_{2.90}O_4$, 70% (vol/vol) of magnetite).[66] These variations in composition is explained by the surface oxidation of magnetite, which might be elevated due to smaller crystal size of maghemite-rich RSN fillers.[113]

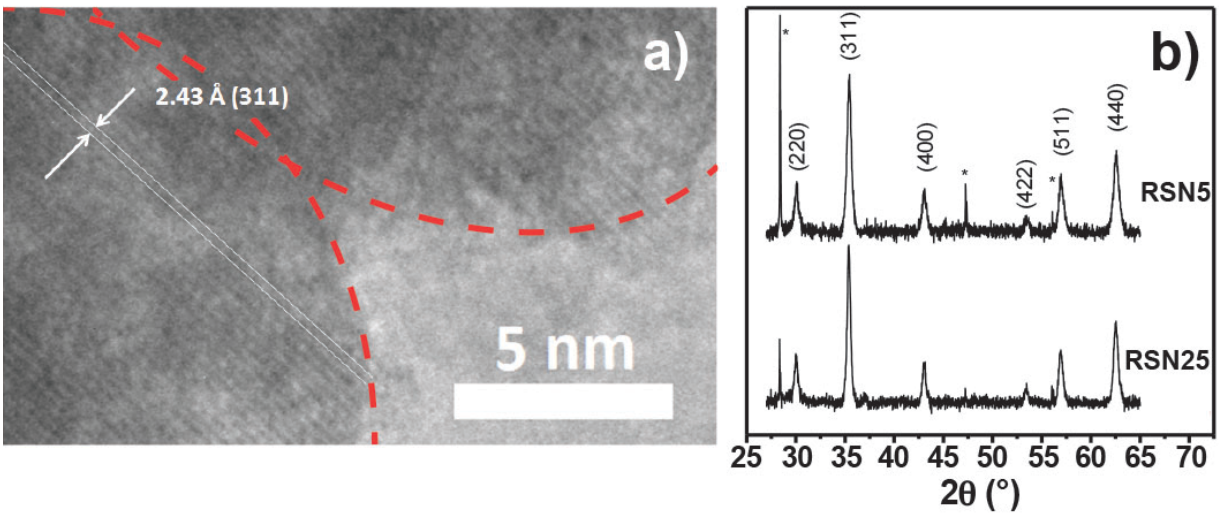

Figure 3.2 a) HRTEM image of RSNs which shows on the nanostructure border that several nanocrystals display the same crystalline orientation. b) XRD data for RSN5 and RSN25.

The characterization of the magnetic properties of RSN fillers correlates well with their structure and composition. The RSNs are superparamagnetic at 300K as the coercivity of both magnetite- and maghemite-rich RSNs at 5K remains below 300 Oe (Figure 3.3-insets), which is indicative of small nanocrystal size.[26, 64] The citrated RSN25 have demonstrated a M_s of 88 emu/g, which is comparable to the bulk M_s of magnetite (92 emu/g) and that of RSN5 is around 74 emu/g which is closed to bulk maghemite (Figure 3.3a,b).[46] In contrast to RSNs, individual magnetite nanoparticles with a similar nanocrystal size have a saturation magnetization between 45 emu/g and 70 emu/g due to defects, surface and volume spin canting.[26, 64, 107, 108] In fact, the structuration of RSNs, which display aggregated orientation of nanocrystals has a critical role for improving the structural and magnetic order, limiting the influence of surface and volume spin canting.[26, 46, 63, 65, 112]

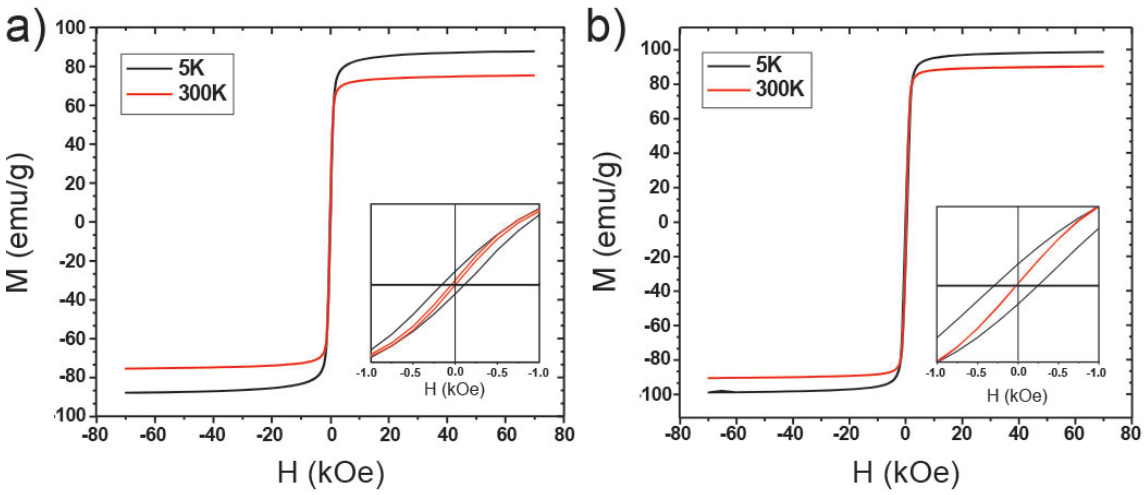

Figure 3.3 Magnetization curves for a) maghemite-rich (RSN5) and b) magnetite-rich (RSN25) RSNs at 5 K and 300K.

The strong dipolar interactions between nanocrystals forming RSNs favors the coupling of spins at the grain surface, which reduces the magnetic and structural disorder arising commonly from defects or broken bonds in the surface of iron oxide nanocrystals.[66] Because of the strong dipolar interactions between nanocrystals, and the common crystallographic orientation of grains, RSNs exhibit higher crystal quality, and lower spin canting than individual iron oxide nanoparticles, which leads to magnetization values matching bulk materials.

The influence of citrate capping on the surface charge of the RSNs was quantified using zeta potential experiments. The RSNs exhibited zeta potential values close to zero prior to attachment of the citrate capping agent, which is in agreement with the isoelectric point of iron oxide (IEP=6.8). The zeta potential of RSNs reached -56 mV with citrate capping, which results in better colloidal stability with the help of electrostatic interactions. These citrate-capped RSNs with a negative surface charge were easily dispersed in a polydimethylsiloxane (PDMS) elastomer matrix and cross-linked to form

stretchable magneto-dielectric composites. Dynamic mechanical analysis was performed to evaluate the mechanical properties of these composites.

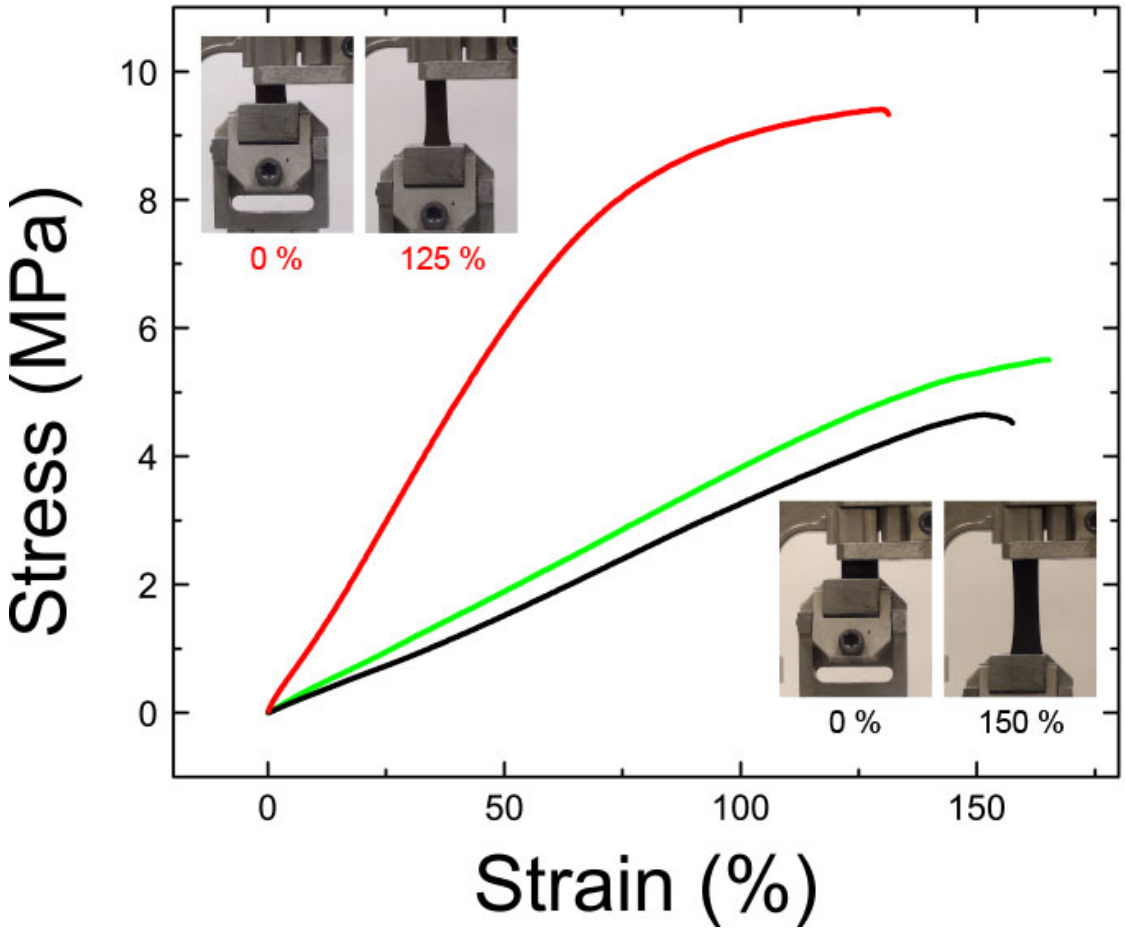

Figure 3.4 Stress/strain curves for PDMS (green), small-grain (red) and large-grain (black) hollow iron oxide nanostructure polymer composites with 60 wt% nanoparticle loading. The images of elongated composites are shown as an inset.

The elastic modulus, as calculated from stress/strain curves, of stretchable composites prepared with small-grain (8.5 MPa) was higher than that of bare PDMS (1.7 MPa) (Figure 3.4).[117] Moreover, stretchable composites prepared with large-grain (1.68 MPa) exhibit similar modulus to bare PDMS. This is indicative of favorable interactions between the nanostructures and the PDMS matrix. The elastic modulus was also dependent on grain size. The higher surface area of the small-grain size nanostructures

(57.3 m^2/g), in comparison to the large-grain nanostructures (27.3 m^2/g), causes more interactions between filler and matrix material and lead to a higher modulus.[27, 118, 119] Additionally, stretchable composites prepared with small-grain (130%) and large-grain (155%) iron oxide nanostructures demonstrated elongation at break values slightly lower than bare PDMS (Figure 3.4).[117]

The permittivity (ε), permeability (μ) and electromagnetic loss values for the composites were measured at a frequency range of 1 KHz to 1 GHz. The permittivity values remained stable and free of dielectric resonance and relaxation for both composites in this frequency range (Figure 3.5a). The composites prepared with large-grain and magnetite-rich RSNs demonstrated permittivity values reaching 9, which is higher than composites prepared with small-grain and maghemite-rich RSNs. Magnetite fillers are known to generate composites with higher permittivity compared to composites prepared with maghemite fillers.[5, 47]

Permeability measurements showed a distinct peak with a maximum value of 2.32 centered at 420 MHz for composites with small-grain nanostructures (Figure 3.5a). The permeability of composites prepared using large-grain iron oxide nanostructures increased with frequency, reaching a maximum permeability value of 2.1 at 1 GHz. The described stretchable magneto-dielectric composites have demonstrated permeability values exceeding that of any reported polymer nanoparticle composites prepared with maghemite[47] or magnetite[107] nanoparticles using similar filler concentration in this frequency range. We believe the high permeability values achieved by these composites originate from the high saturation magnetization of the hollow iron oxide nanostructures.

The dielectric ($\tan\delta_\varepsilon=\varepsilon'/\varepsilon''$) and magnetic ($\tan\delta_\mu=\mu'/\mu''$) loss values for composites were measured to investigate electromagnetic loss characteristics and resonances at the frequency range of interest (1 KHz to 1 GHz). The dielectric loss values of composites fabricated using both maghemite-rich small-grain and magnetite-rich large-grain RSNs do not demonstrate a dielectric resonance in the range 1 KHz to 1 GHz. Additionally, dielectric loss values remain below 0.1 for either composite. The frequency dependence of magnetic loss values for composites prepared with maghemite-rich small-grain RSNs show local maxima between 400 MHz and 600 MHz, as the slope of the curve drops drastically at 480 MHz, which is indicative of a magnetic resonance (Figure 3.5b). This local maxima is masked by the presence of a second magnetic resonance at frequencies higher than 600 MHz, which could potentially be caused by the structure oriented gyromagnetic resonance reported at 1.5 GHz for maghemite nanoparticles.[120] The magnetic loss characterization of composites prepared with the magnetite-rich RSNs show an increase in loss values between 600 MHz and 1 GHz. In concert with permeability measurements, the magnetic loss measurements indicate a magnetic resonance at a frequency slightly higher than 1 GHz. Further characterization revealed that the magnetic loss value for composites assembled with maghemite-rich RSNs was 0.11 at 420 MHz. Composites prepared with magnetite-rich RSNs had a magnetic loss value of 0.13 at 1 GHz.

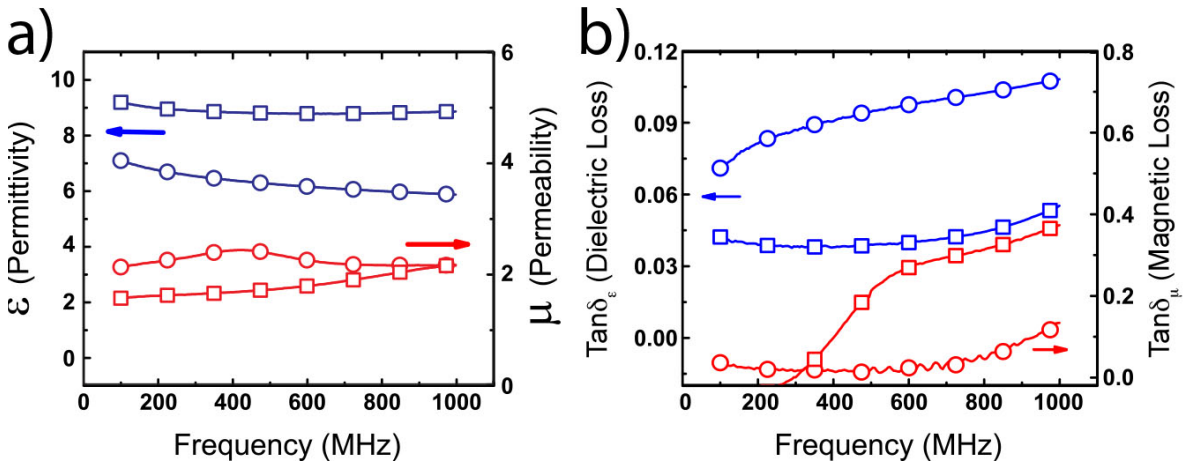

Figure 3.5 Frequency dependence of a) permittivity (ε), permeability (μ) and b) dielectric and magnetic loss values of large grain (squares) and small-grain (circles) hollow iron oxide nanostructure polymer composites with 60 wt% nanoparticle loading.

The theoretical ferromagnetic resonance frequency of spherical maghemite and magnetite is calculated to identify the origin of the magnetic resonances in these magneto-dielectric composites.[121]

$$f_r = \gamma H_k \tag{5}$$

The magnetocrystalline anisotropy field (H_k) is calculated by assuming cubic symmetry for both maghemite and magnetite particles.[107, 122]

$$H_k = \frac{2|K_1|}{\mu_0 M_S} \tag{6}$$

The gyromagnetic ratio ($\gamma/2\pi$) of electrons was used for these calculations (28 GHz/T).[121] Magnetocrystalline anisotropy constant (K_1), saturation magnetization (M_S) values along with calculated ferromagnetic resonance frequencies for maghemite and magnetite nanoparticles are given in Table 3.1.

Table 3.1:

	Maghemite nanoparticles [122]	Magnetite nanoparticles [107]
K_1 (J/m^3)	$4.6x10^3$	$-1.2x10^4$
M_S (A/m)	$4x10^5$	$4.6x10^5$
Theoretical f_r (MHz)	480 MHz	1.46 GHz
Experimental f_r (MHz)	600 MHz	1.3 GHz

Previous experimental studies have demonstrated that ferromagnetic resonance frequency for maghemite nanoparticles is 600 MHz, which is slightly higher than the theoretical ferromagnetic resonance of maghemite nanoparticles, and maghemite-rich magneto-dielectric composites.[122] In addition, the experimentally determined ferromagnetic resonance frequency for magnetite nanoparticles is 1.3 GHz, which is slightly lower than theoretical ferromagnetic resonance frequency of magnetite nanoparticles.[107] The difference in calculated resonance frequencies of magnetite and maghemite nanoparticles, and experimentally determined resonance conditions for the type of nanoparticle, and RSN based composites possibly originate from the heterogeneous composition of filler materials, which leads to changes in the magnetocrystalline anisotropy constants.[107, 122, 123]

The permeability peak at 420 MHz, and the drastic increase in magnetic loss from 400 MHz to 600 MHz for composites prepared with maghemite-rich RSNs (small grains) are most probably stemming from the ferromagnetic resonance of maghemite at 480

MHz. In addition, the increase in permeability and magnetic loss starting from 600 MHz for composites consisting of magnetite-rich RSNs (large grains) can be explained by the natural ferromagnetic resonance of magnetite (1.46 GHz) as the permeability and magnetic loss starts to increase prior to resonance frequency. [107] Therefore, it is possible that the composition of the filler material defines the magnetic resonance frequency for the composites with large- and small-grain RSNs. This composition dependence can be used to change the magnetic resonance frequency of the composites by altering the level of oxidation of RSNs with reaction time of the solvothermal synthesis. These low loss values possibly stem from limited coercivity of the iron oxide nanostructures.

3.4 Conclusions

In summary, stretchable magneto-dielectric composites with high permeability, low magnetic loss were demonstrated using iron oxide RSN fillers with high M_s and low coercivity. Iron oxide RSN fillers consisting of magnetic nanocrystals aggregated with common crystallographic orientations displaying higher M_s in comparison to individual iron oxide nanoparticles with coercivity values smaller than 300 Oe. This allowed magneto-dielectric composites to achieve permeability values reaching 2.3 with magnetic loss values that did not exceed 0.4. Iron oxide RSNs with different composition and crystal size have resulted in magneto-dielectric composites with distinct magnetic resonance. Additionally, the citrate capping of iron oxide nanostructures ensured uniform distribution of the filler in the elastomer (PDMS) matrix, which prevented formation of conductive losses in composites and provided the ability to stretch up to 155% strain. Imparted with excellent stretchability, these unique

magneto-dielectric characteristics provide evidence that such composites can be utilized to fabricate high efficiency flexible antennas operating at distinct RF frequencies.

Chapter 4: Sprayable Elastic Conductors Based on Block Copolymer Silver Nanoparticle Composites

4.1 Introduction

Stretchable conductor research has expanded significantly due to interest in mechanically deformable circuitry for use in flexible electronics. Such materials have applications in stretchable displays,[22] solar cells,[124] field effect transistors,[125] radio frequency antennas,[39] strain and tactility sensors,[126-129] and epidermal electronics.[15, 20, 74, 76, 130] Current approaches use assemblies of conductive and elastomeric components to produce materials that maintain electrical properties under strain. However, the mechanical properties of the conductive component often cause a decrease in elasticity when composites reach high electrical conductivities.[131]

Stretchable conductors have been demonstrated using networks of nanowires or nanotubes back-filled with elastomers,[9, 132-134] polymer nanoparticle composites,[11, 38] liquid metal filled elastomeric channels,[39, 69, 70, 135] conductive networks on pre-strained or buckled substrates,[136, 137] and metallic fractal or microwire patterns on polymer substrates.[76, 138] Metallic nanowire and carbon nanotube based materials have shown mechanical and electrical robustness under cyclic deformation.[132, 133] However, when these systems reach high conductivities there is a significant reduction in maximum tensile strain due to increased rigid filler content.[133, 139] Polymer nanoparticle composites have demonstrated enhanced mechanical elasticity and high conductivity, but require higher filler content when compared to nanowire and nanotube based materials with similar conductivities.[38] Elastomers containing channels of liquid metal

compromise overall material strength due to the inherent mechanically poor nature of the conductive component. Metallic patterns are able to maintain the bulk electrical properties of the conductive component under strain with limitations for the ultimate achievable strain values originating from the pattern geometry.[76]

Another important consideration in the development of elastic conductors is the ease of fabrication and deposition of the material onto non-planar substrates. This is particularly important for applications such as epidermal electronics[76] and smart textiles.[140] Current methodologies utilize complex lithographical methods,[17, 68, 141, 142] printing,[77, 143, 144] or spray techniques,[127] and require transfer from a planar fabrication substrate to a non-planar substrate of interest. These methods have been utilized to transfer flexible electronic devices onto a variety of contoured substrates such as concave,[68] convex,[145, 146] and other curved surfaces.[15, 17] The deformation that occurs when a planar elastic conductor is placed conformally onto a non-planar substrate leads to degradation of the material's electrical properties.[146] To our knowledge, direct deposition of stretchable conductors on non-planar substrates has not yet been demonstrated.

Here we report a method to fabricate highly conductive elastic composites with electrical properties that vary minimally under high levels of strain. This fabrication process allows for conformal deposition on non-planar substrates utilizing a combination of solution blow spinning[147] and spray coating or printing. The deposition process is direct, and does not require transfer from a separate substrate. The resulting stretchable conductor consists of an elastomeric fiber mat silver nanoparticle composite. Initially, a fiber mat is blow spun from a solution of poly(styrene-block-isoprene-block-styrene) (SIS) block copolymer in tetrahydrofuran (THF) (Figure 4.1). To establish

conductivity, a silver precursor solution is applied to a pre-spun mat and is nucleated into a network of silver nanoparticles, forming conductive pathways. The resulting composite achieves a conductivity of 2000 ± 200 S/cm at zero applied strain, with only a 12% increase in resistance after 400 cycles at 150% strain. These stable electrical properties are attributed to conductive pathways maintained through silver nanoparticle stabilized fiber-to-fiber contacts and strain induced structural changes. We have also demonstrated the ability to tune the strain dependence of the electrical properties by adjusting nanoparticle precursor concentration or localized nanoparticle nucleation. The versatility of this approach was demonstrated by constructing a stretchable light emitting diode (LED) circuit and a strain sensor on planar and non-planar substrates.

4.2 Experimental

4.2.1 Stretchable conductor fabrication

Solutions of poly(styrene-block-isoprene-block-styrene) (SIS) (Sigma Aldrich, 22 wt% styrene content) and tetrahydrofuran (THF) (Fisher Scientific, 99.9%) were prepared and fed with a constant feed rate (10 ml/hr) through the nozzle of the solution blow spinning setup constructed from a transfer pipette and a flat tipped 18G needle connected to a syringe pump and compressed air line (Figure 4.1b). The air pressure was kept constant during the blow spinning process at 50 psi. Elastomeric fibers were accumulated on a metal mesh. The resulting polymer fiber construct was lifted from the metal mesh and immersed in a previously prepared organometallic solution consisting of silver trifluoroacetate (STFA) (Sigma Aldrich, 98%) and ethanol (Pharmco-Aaper, 99%) for 30 minutes, then dried in a vacuum desiccator. Silver nanoparticle nucleation

was initiated via drop-wise addition of reducing solution consisting of hydrazine hydrate (50% (vol/vol)) (Sigma Aldrich, 50%-60%), deionized water (25% (vol/vol)) and ethanol (25% (vol/vol)). The resultant conductive fiber composite was washed thoroughly with water to eliminate any unbound nanoparticles and dried overnight under vacuum.

4.2.2 Characterization

Scanning Electron Microscopy (SEM) (Hitachi SU-70) and Transmission Electron Microscopy (TEM) (JEOL 2100F) were used to characterize the microstructure of the block copolymer nanoparticle composites. The TEM sample used for cross-section analysis was prepared using a microtome (Leica EM UC-6). Fiber diameter is reported as an average of 50 measurements taken from three SEM images. Nanoparticle diameter is reported as an average of 150 measurements taken from three TEM images. A dynamic mechanical analyzer (TA Instruments Q800) and an Instron tensile tester (model 3345) were used to characterize the mechanical properties of the stretchable conductors. Energy dissipation was calculated from the area of the hysteresis loops of cyclic stress/strain curves for both SIS fiber mats and conductive composites (n=3, error bars represent standard deviation). The electrical conductivity of the stretchable conductor samples were measured using a custom built automated 4-point probe measurement system connected to a Keithey 2400 Sourcemeter (n=5, error bars represent standard deviation). The normalized resistance measurements under mechanical strain were performed using a high precision optical stage and an Ohmmeter (Amprobe 33XR-A).

4.2.3 Device fabrication and patterning

Strain sensors were fabricated via fiber mat deposition on a nitrile glove and subsequent nanoparticle nucleation. Once the glove was completely covered with elastomeric fibers, lines were drawn on each finger using a flow-pen (Paasche F-I/32) filled with STFA solution (25% (wt/vol)). The conductive lines were formed after hydrazine hydrate solution was applied drop wise onto the STFA patterned lines. The strain sensing measurements were performed using an Ohmmeter (Amprobe 33XR-A) attached to the conductive lines on the glove with alligator clips. The conductive composite connecting the LEDs was stretched using a precision optical stage, while being powered with a DC source (Hewlett Packard E3630A) with constant voltage required to initiate luminescence of the LED (5V). The parallel lines were patterned on 300 μm thick planar elastomeric fiber mats by spray coating 25% (wt/vol) STFA solution with a bottom feed airbrush (40 psi air pressure, 20 ml/hr solution feed) through a micromachined shadow mask and subsequently nucleated by spray coating hydrazine hydrate solution. For elastomeric fiber mat thicknesses exceeding 500 μm the precursor solution did not diffuse through the entire cross-section leading to non-uniform patterning. The pattern resolution is currently restricted to 300 μm as the swelling of the fiber mat prohibits fabrication of patterns with higher resolution. The patterned stretchable conductor was washed with water and dried under vacuum overnight prior to characterization.

4.3 Results and Discussions

The process of block copolymer nanoparticle composite fabrication consists of elastomeric fiber mat deposition, introduction of silver nanoparticle precursor, and nanoparticle nucleation (Figure 4.1a). Solution blow spinning was used to generate non-woven block copolymer fiber mats, allowing for rapid deposition on non-planar substrates (Figure 4.1b).[147-149] This technique requires only a simple apparatus, high-pressure gas source, and a concentrated polymer solution in a volatile solvent.[147] Analogous to other solution processed spinning techniques, fiber generation is achieved above a critical solution concentration, corresponding to polymer chain overlap.[150] An elastomeric block copolymer was utilized because the presence of the rigid block, in this case polystyrene, allows the material to remain structurally stable without crosslinking. Upon the introduction of the silver nanoparticle precursor solution, fiber mats swell and become translucent. This is indicative of a preferable interaction between nanoparticle precursor and polymer, as swelling does not take place when solvent alone is introduced. This affinity is explained by the specific interactions of transition metal ions with unsaturated hydrocarbons, such as the double bonds on isoprene, that form weak charge transfer complexes.[151] Finally, nanoparticles are nucleated through reduction of the silver ions associated with isoprene creating a conductive composite.

Microstructure characterization by scanning electron microscopy (SEM) revealed that a fiber network structure was achieved for SIS/THF solutions with a concentration of 20% (wt/vol) (Figure 4.2a). The average diameter of elastomeric fibers after spinning was 1.66 ± 0.70 μm as measured by SEM. This network structure, consisting of high

aspect ratio cylindrical fibers, facilitates homogeneous nanoparticle distribution. The fiber mats were swollen in silver nanoparticle precursor solution containing various concentrations of silver trifluoroacetate (STFA) in ethanol.

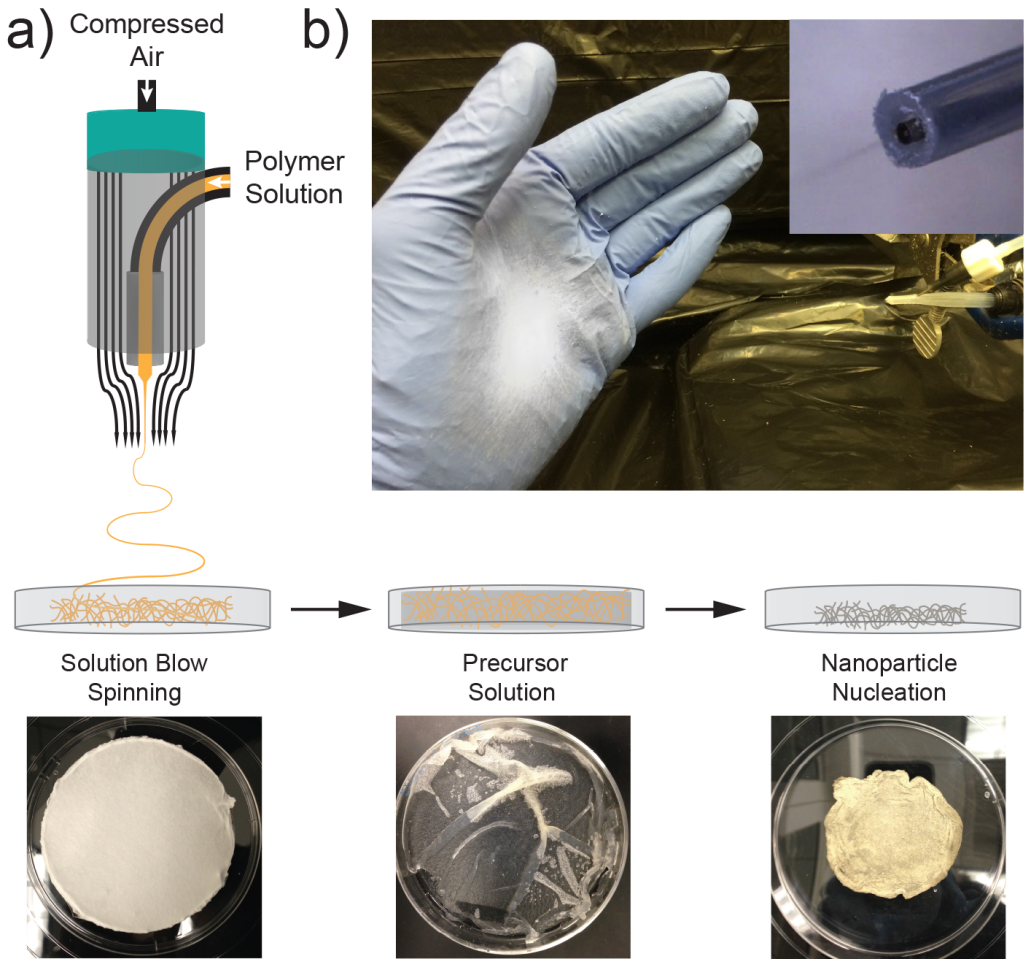

Figure 4.1 a) Schematic illustration of poly(styrene-block-isoprene-block-styrene) (SIS) block copolymer solution blow spun fiber network fabrication and images of the as spun fiber network, fiber mat swollen with silver nanoparticle precursor solution, and conductive polymer-nanoparticle composite after nanoparticle nucleation. b) Image of the direct deposition of SIS fibers onto a gloved hand (solution blow spinning nozzle in use-inset).

Through this process the fiber diameter increased to an average of 3.28 ± 1.51 μm and fiber-to-fiber contact was enhanced by the formation of additional fiber junctions (Figure 4.2b). Hydrazine hydrate solution was then used to reduce the silver ions in the

precursor-swollen mats, forming silver nanoparticles with an average diameter of 37.6 ± 14.2 nm as measured by transmission electron microscopy (TEM) (Figure B.1).

Individual fiber diameter decreased in comparison to the swollen state and bound fiber-to-fiber connections were stabilized with nanoparticles subsequent to their nucleation (Figure 4.2c). TEM of the silver nanoparticle polymer fiber composite cross-section revealed that nanoparticles populate the outer surface of fibers (Figure 4.2d). Styrene content also had a major effect on composite morphology. A fiber mat fabricated with 14 wt% styrene SIS irreversibly lost fiber morphology during precursor swelling and nanoparticle nucleation (Figure B.2).

The nanoparticle precursor solution concentration effect on conductivity was assessed by measuring bulk conductivity of the polymer nanoparticle composites (Figure 4.3a). Maximum conductivity values (~2000 S/cm) were achieved with a precursor concentration range between 25% and 35% (wt/vol). Fabrication of composites with 30% and 35% (wt/vol) STFA solutions led to increased variability in conductivity, 2000 ± 300 S/cm and 1700 ± 400 S/cm respectively. This variability can be attributed to trapped nitrogen gas formed during the nucleation reaction that creates voids and results in fiber mat delamination and structural heterogeneity. This was further reflected in elastic recovery experiments, where these materials yielded before completing cycling up to 150% strain (Figure B.3). Materials fabricated with 25% (wt/vol) and lower STFA solutions all survived cycling to 150% strain with no significant difference between the elastic recovery of conductors fabricated with 25% (wt/vol) STFA solution and SIS fiber mats (Figure B.3).

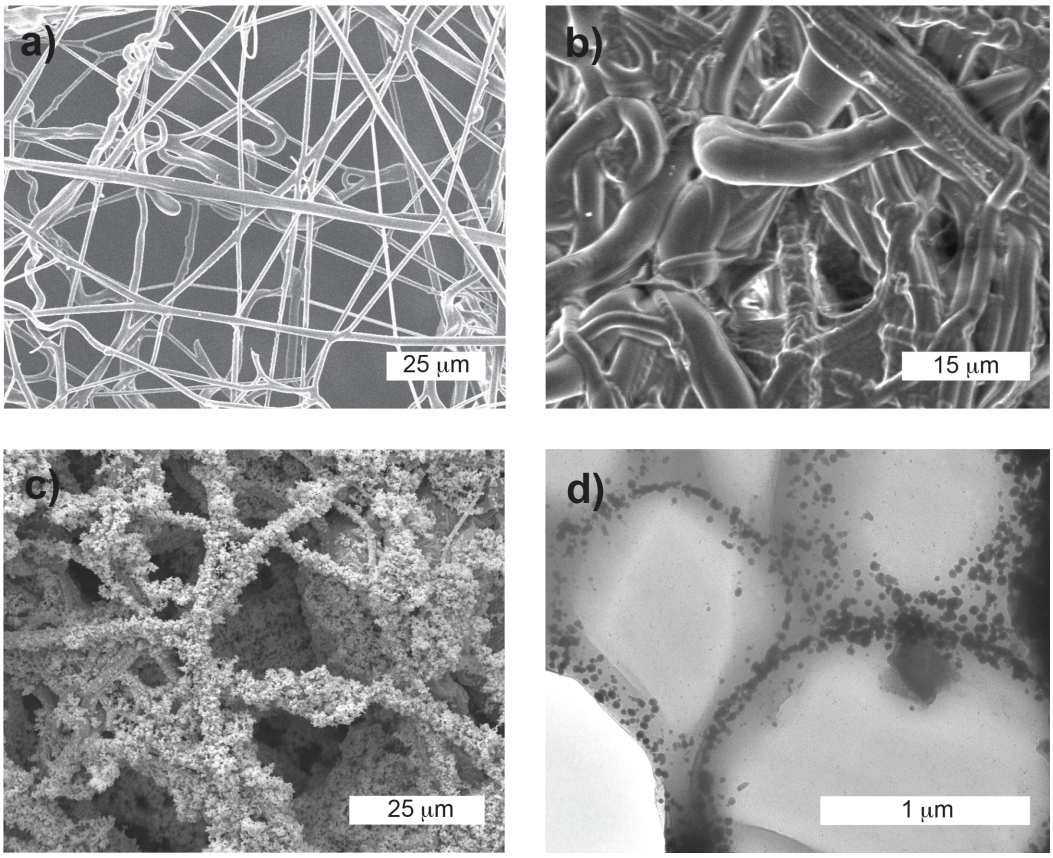

Figure 4.2 a) SEM images of SIS blow spun fiber network, b) swollen with silver precursor solution, c) conductive composite decorated with silver nanoparticles, d) cross-section TEM image of conductive block copolymer nanoparticle composite fibers.

Electrical properties under cyclic strain were characterized for conductive composites. Precursor concentration markedly influenced electromechanical behavior. The normalized resistance (R/R_0) values of polymer nanoparticle composites fabricated with 10% (wt/vol) STFA solutions reach 1.85 at 150% strain with appreciable hysteresis beginning at 40% strain (Figure **4.**3b). When STFA concentration is increased to 25% (wt/vol) normalized resistance at 150% strain decreases to 1.06 with a significant reduction in hysteresis after a single cycle (Figure **4.**3b). This stable electrical behavior under strain was additionally observed by a minimal resistance increase after 400 cycles of 100% (R/R_0=1.06) and 150% strain (R/R_0=1.12) (Figure 4.3c, d). Stretchable

conductors with similar and higher bulk conductivity have not achieved comparable stability of electrical properties under mechanical deformation ((σ_0/σ=4.0, σ_0=1670 S/cm, 150% strain),[152] (σ_0/σ=4.6, σ_0=11000 S/cm, 110% strain),[38] (σ_0/σ =8.9, σ_0=5400 S/cm, 140% strain)[11]). Additionally, the resistance of the conductive composites at 0% strain remains unchanged with repetitive deformation (Figure 4.3c).

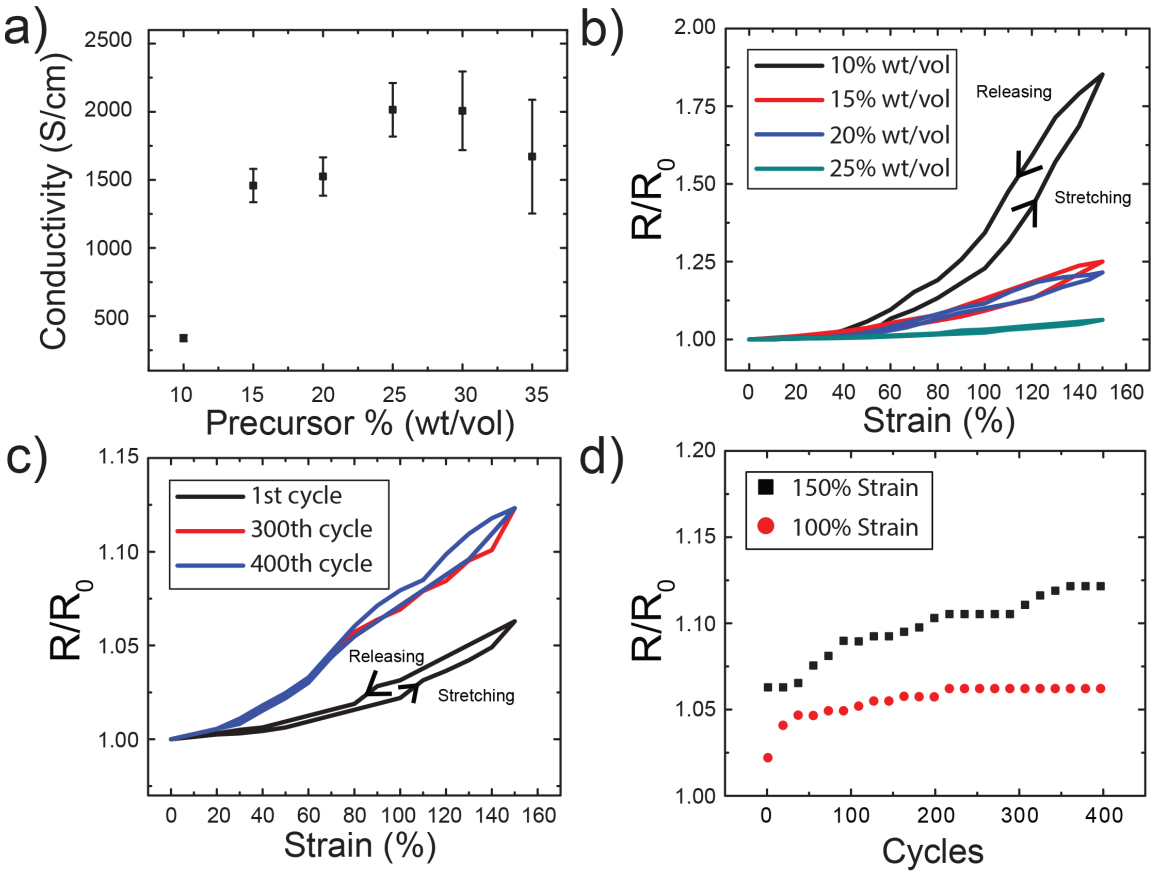

Figure 4.3 a) Average electrical conductivity of stretchable conductors as a function of STFA concentration. b) Normalized resistance values as a function of uniaxial tensile strain for various STFA concentrations. c,d) Normalized resistance values as a function of uniaxial tensile strain and cycle number.

This indicates that changes in electrical properties are recoverable when undergoing strain cycling up to 150% strain. In order to evaluate the influence of the fiber network

on the electromechanical properties, conductive SIS films were fabricated via drop casting, swollen with silver precursor, and nucleated. The electrical conductivity of these films is lost before reaching 55% strain, which is prior to mechanical failure of the film (Figure B.4). We believe the electromechanical characteristics of the elastomeric fiber based conductors are primarily the result of structural changes during mechanical deformation.

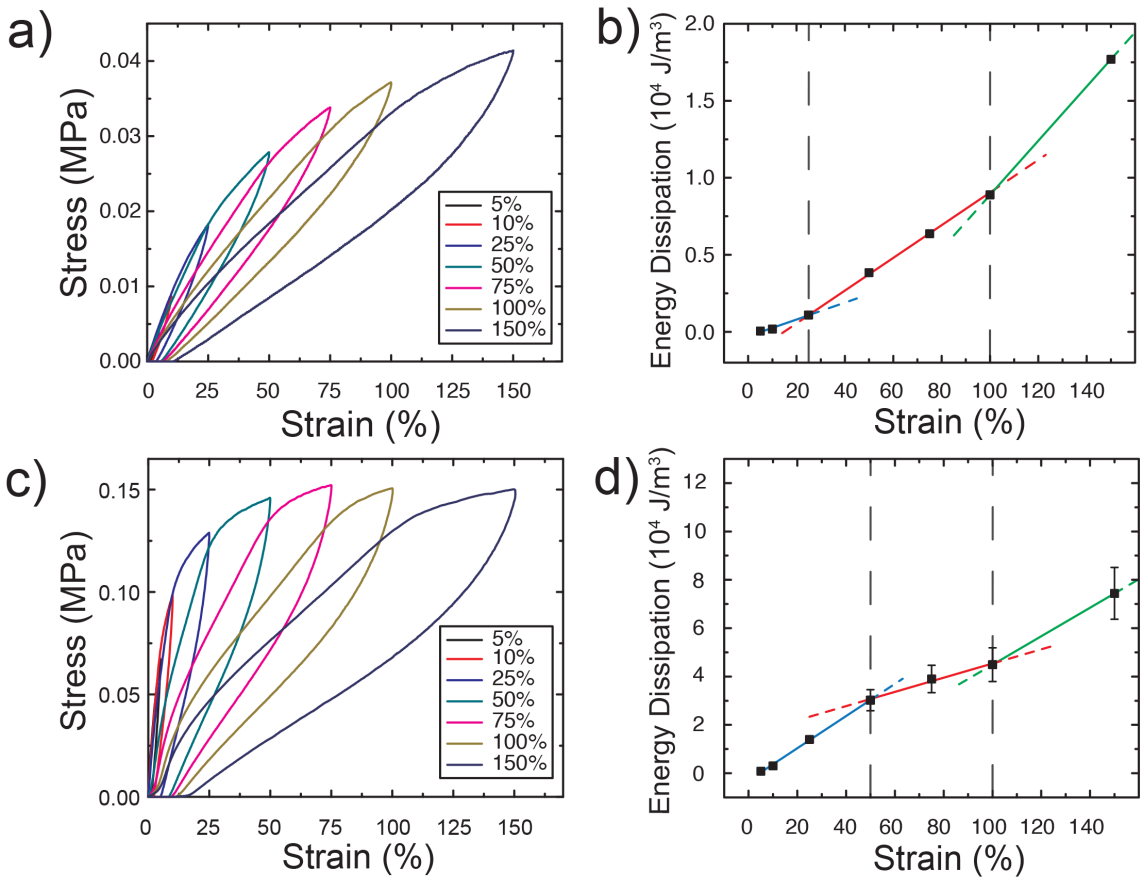

Figure 4.4 a) Stress/strain cycling curves and b) average energy dissipation values and corresponding linear fits for pure SIS fiber mats. c) Stress strain cycling curves and d) average energy dissipation values and corresponding linear fits for elastic conductors fabricated with 25% (wt/vol) STFA solutions. Linear correlations relating energy dissipation to strain describe different regions of strain induced structural changes (blue, red, and green lines).

To investigate this influence, energy dissipation was calculated from the area of the hysteresis loops of cyclic stress/strain curves for both SIS fiber mats and conductive composites (Figure 4.4, B.5). This analysis revealed the presence of three distinct regions corresponding to strain induced structural changes (Figure 4.4b, d). These regions were determined using linear correlations relating energy dissipation to strain. Changes in slope are indicative of a structural transition. In SIS fiber mats, increasing strain led to an increase in slope after each transition. At strain levels below 25%, minor structural changes occur in which fibers rearrange. Bound fiber connections break when strain values increase to greater than 25%. These connections are known to contribute significantly to the mechanical strength of elastomeric fiber mats.[153, 154] As strain values continue to increase to above 100% strain, individual fibers begin to deform. Different strain dependent mechanical properties are evident in the conductive composites.

In contrast to the pure SIS fiber mats, large changes in dissipative losses occur at strains below 50%. These large changes possibly stem from breakage of particle-to-particle contact in silver nanoparticle reinforced fiber junctions. At strain values beyond 50%, diminishing influence of these reinforced junctions allow fibers to rearrange. Fiber rearrangement results in less drastic changes in energy dissipation for strain values between 50 and 100%. At strains values above 100%, individual fibers deform and silver nanoparticle coverage becomes discontinuous. This results in an increased rate of dissipative loss at high strain values.

The described structural changes were confirmed by imaging conductive composites at region-specific strain values of 0%, 50%, 100%, and 150% (Figure 4.5). At 50% strain, there are no discernable changes in structure except for breakage at silver nanoparticle

reinforced fiber junctions (Figure 4.5b-inset). As strain is increased to 100% fibers are able to rearrange in the direction of applied strain (Figure 4.5c). At strain values exceeding 100%, fibers elongate and the silver nanoparticle coating becomes intermittent (Figure 4.5d).

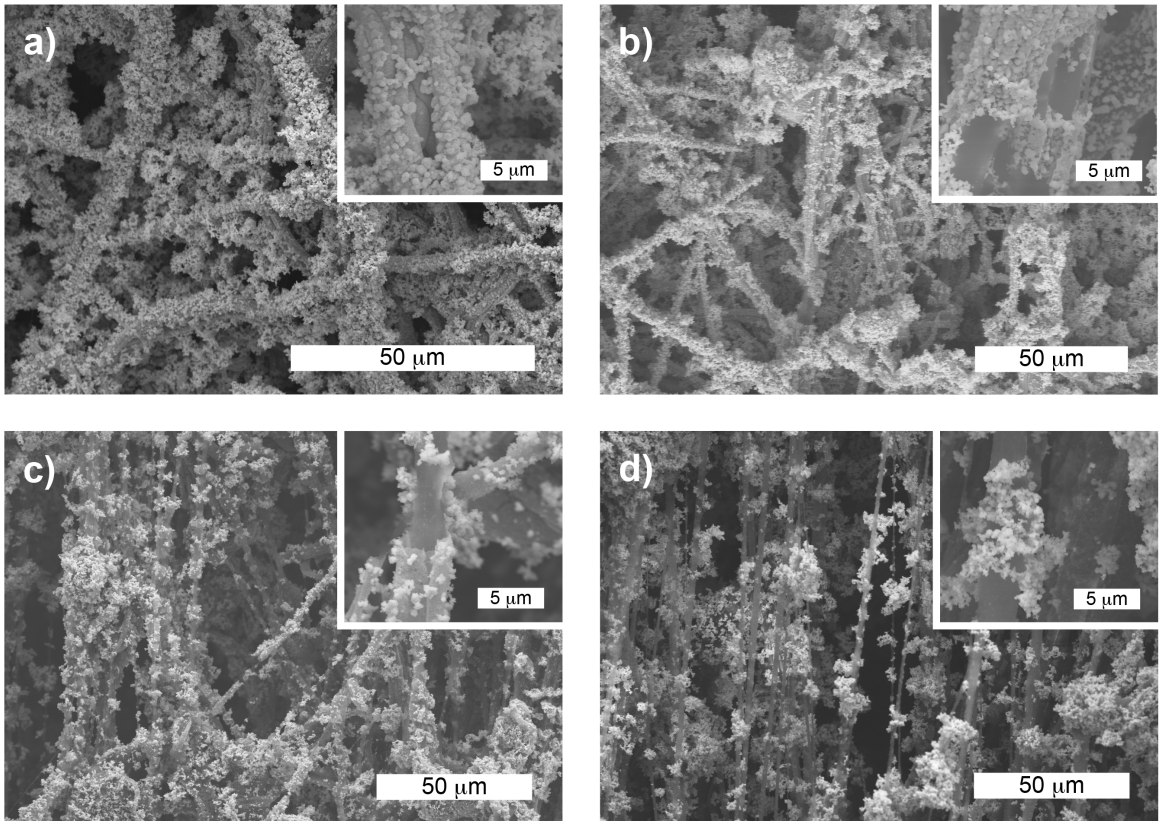

Figure 4.5 SEM images of conductive composites fabricated using 25% (wt/vol) STFA solutions under a) 0% strain, b) 50% strain, c) 100% strain, and d) 150% strain. Higher magnification SEM images of individual fibers for respective conductive composites under different strain values are provided in the inset.

Structural and mechanical analysis of the conductive composites is in agreement with the previously described electromechanical properties. The onset of hysteresis in electrical properties during initial mechanical deformation is concurrent with structural changes originating from fiber rearrangement (Figure 4.3b, c). Structural rearrangement

in the direction of applied strain has been previously shown to cause electrical hysteresis in conductive elastomer nanocomposites due to anisotropic network deformation that leads to a decrease in conductive component connectivity.[33] While undergoing cyclic strain testing to 150%, strain dependence of electrical properties increases up to the 300th cycle as fibers irreversibly deform. After the 300th cycle, electrical properties stabilize due to the previously incurred plastic deformation (Figure 4.3c). This is also reflected in Figure 4.3d, where normalized resistance values for the conductive composite increase as function of cycle number until reaching the 300th cycle of 150% strain. Fibers do not irreversibly deform If only cycled to 100% strain. Fiber rearrangement causes initial increases in normalized resistance values, resulting in electrical property stabilization after the 50th cycle (Figure 4.3d). When strained beyond 150%, electrical properties rapidly deteriorate, reaching a normalized resistance value of 81.1 at mechanical failure (~400% strain, Figure B.6).

Using the described approach for depositing and patterning elastic conductors on non-planar surfaces requires three separate deposition steps and compatibility considerations. The solution blow spun elastomeric fibers must first adhere to the substrate of interest. SIS and other styrene block copolymers, in combination with other additives, have been investigated and used as adhesives.[155, 156] The physically anchored block copolymer structure combines low elastic modulus (isoprene block) and creep resistance (styrene block) imparting inherent adhesiveness to SIS.[155, 157] Solution blow spun SIS fiber mats adhered to a variety of substrates, including glass, metal mesh, silicon wafer, polystyrene, and aluminum foil. The second major consideration regarding direct deposition and patterning through spray coating or printing is solvent

and chemical compatibility. Ethanol sensitive substrates, such as polymers containing hydroxyethyl methacrylate or vinylpyridine, could deform during nanoparticle precursor application. During nucleation, hydrazine reactive substrates, such as polyesters, could be damaged through aminolysis.[158]

A proof of concept device utilizing this approach was demonstrated by depositing and patterning strain sensors. An elastomeric fiber mat was first solution blow spun directly on a nitrile glove (Figure 4.6a). A solution pen (Paasche F-I/32) with adjustable flow rate was then used to deposit a line of precursor solution (25% (wt/vol)) along each finger. The patterned lines were then nucleated into silver nanoparticles, thereby forming stretchable conductive lines corresponding to each finger. Resistance of each conductive line was measured while performing multiple hand gestures, where normalized resistance values corresponded to individual finger movements (Figure 4.6a). Glove strain sensors have also been shown previously using other materials.[33, 135] The strain dependence of electrical properties was evaluated separately to identify the difference between patterned stretchable conductors and bulk stretchable conductors (Figure B.6). This reveled that electrical properties resulting from localized nanoparticle nucleation have higher strain dependence as compared to bulk stretchable conductors, allowing for utilization as a strain sensor for relatively low strain conditions ($\varepsilon<50\%$).

A basic circuit consisting of 2 LEDs connected with a stretchable conductor prepared using 25% (wt/vol) STFA solution was also constructed (Figure 4.6b). The illumination of both LEDs remained stable while the conductive composite was stretched up to 150% strain (Figure 4.6b). Patternability and processability on planar substrates was demonstrated with spray techniques. A planar substrate with minimal surface

roughness, such as a silicon wafer, allows for the use of a shadow mask. Utilizing this approach, a stretchable fiber mat on top of a silicon wafer was patterned with conductive parallel lines by applying precursor solution (25% (wt/vol) STFA) with a bottom feed airbrush through a shadow mask. Silver nanoparticles were then nucleated to form defined lines with a thickness of 300 mm and a conductivity of 1300 S/cm (Figure 4.6c).

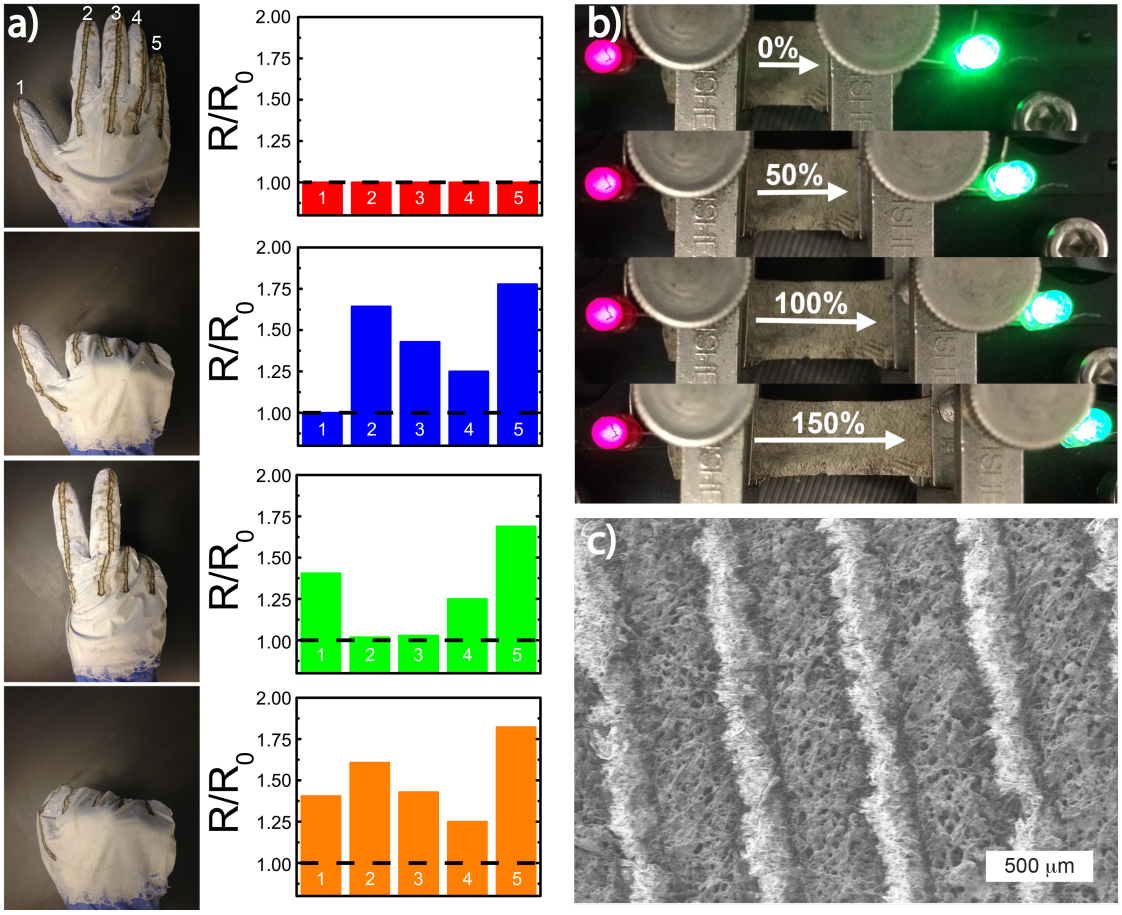

Figure 4.6 a) Images of hand gestures performed wearing a nitrile glove coated with elastomeric fiber mat and patterned with conductive lines. Normalized resistance values for conductive lines patterned on each finger numbered from 1 to 5. b) Images of LED circuit operating under various strain conditions c) SEM image of parallel conductive lines patterned using spray coating.

4.4 Conclusions

We have developed a method to deposit conformal stretchable conductive fiber mats using solution blow spinning and metallic nanoparticle nucleation on non-planar substrates. The stretchable fiber mats were able to combine electrical conductivity values as high as 2000 S/cm with R/R_0 values as low as 1.12 after 400 cycles of 150% strain. The stable electrical properties of these stretchable conductors potentially stem from conductive pathways maintained through silver nanoparticle stabilized fiber-to-fiber contacts and strain induced structural changes. Additionally, the strain dependence of the electrical properties was tuned via localized nanoparticle nucleation or reduction in precursor concentration. Control of electromechanical properties allows for materials to be tailored for specific applications. To demonstrate the utility of this method we employed stretchable conductors in simple devices including strain sensors on nitrile gloves and stretchable electrodes connecting LEDs.

Chapter 5: Solution-processed Stretchable Conductors Based on Block Copolymer Fibers with Dual Silver Nanoparticle Networks

5.1 Introduction

Materials with the ability to maintain high electrical conductivity under large deformations are necessary for the fabrication of stretchable electrical circuits with high performance. Elastic conductors have been utilized in a variety of stretchable electronic devices including displays,[22] solar cells,[124] supercapacitors,[159] batteries,[160] radio-frequency antennas,[11, 39, 45] smart textiles,[12, 13, 32] and epidermal sensors.[15, 74, 75] The inherently brittle nature of conductive materials, and poor electrical properties of elastomers necessitates the use of composites in the development of elastic conductors.[23, 29] The most common approaches utilize composite structures such as liquid metal filled channels within soft elastomer matrixes[39, 70, 72] or conductive networks composed of nanowires[161, 162] or nanotubes[9, 10] backfilled with an elastomeric component. In the first case, since the metal alloy is in a liquid state it is able to take the shape of the channels fabricated in soft elastomeric matrix and maintain electrical conductivity under deformation. However, liquid metal-based elastic conductors have reliability concerns due to the extremely poor mechanical properties and risk of leakage of the conductive component.[29, 72] Elastomer backfilled conductive nanowire or nanotube networks have similar advantages and deficiencies with the ability to maintain high electrical conductivity at the cost of poor mechanical properties. In these materials the large amount of conductive component required for high conductivity leads to limited elongation at failure.[9, 33, 139, 162] Certain limitations of these approaches have been resolved by patterning the metallic component in specific geometries including

springs,[163, 164] wavy,[77, 136, 163] and fractal patterns.[76] These patterns are able to maintain high conductivities under moderate strains but have finite maximum strains that arise from the limitations of the chosen geometry.[76, 77]

More recently, elastic conductors made using composites composed of elastomers and conducive nanoparticles have proven to be an effective means of developing high performance materials for use in stretchable device applications.[11, 86] Even though these materials require higher filler concentration of the conductive component when compared to nanowires or nanotubes to establish conductivity, the spherical geometry provides improved particle mobility within the polymer matrix when undergoing strain.[29, 38] Increased particle mobility allows these composites to maintain a large percentage of their initial conductivity under tension due the dynamic formation of alternate conductive pathways during deformation. The elastic properties of these composites still considerably diminish with increasing nanoparticle content, which is required to reach high conductivity values.[38] Using polymer fibers as the elastomeric portion of the composite has partially addressed this shortcoming.[11, 86] Confining nanoparticles in a cylindrical geometry enables the composites to reach higher electrical conductivity values with the same filler content due to a lower percolation threshold.[11] The fiber network also provides a mechanism to establish alternative conductive pathways under tensile deformation through fiber rearrangement.[165] Elastic conductors based on polymer fiber networks have displayed a variety of material properties ranging from highly deformable materials with limited electrical conductivity[86] to highly conductive composites with strain-sensitive electrical properties.[11] The difficulties in achieving both a highly deformable and highly

conductive material arise from nanoparticle localization at the fiber surface and/or low volumetric concentration of the nanoparticles in the composite.[11, 86]

Here we demonstrate solution-based fabrication of highly conductive composites consisting of block copolymer fiber networks and conductive nanoparticles. High nanoparticle loading is achieved by including separate nanoparticle networks on the surface and within the cross-section of the fibers. Specifically, poly(acrylic acid) capped silver nanoparticles (Ag-PAA) were synthesized using an aqueous synthesis method. The synthesized Ag-PAA nanoparticles are then dispersed in a solution of poly-(styrene-block-isoprene-block-styrene) block copolymer (SIS) dissolved in tetrahydrofuran (THF). This solution is then used to deposit a polymer fiber network containing in-fiber nanoparticles using a technique called solution blow spinning. This technique allows polymer fiber networks to be rapidly deposited on a substrate of interest, including synthetic and biological interfaces.[86, 166] A second population of nanoparticles is introduced to the polymer-nanoparticle composite through the addition and nucleation of an organometallic precursor, leading to the formation of an interconnected network of conductive nanoparticles throughout the composite. The resulting material reaches a maximum initial conductivity value of 9000 ± 200 S/cm, which drops slightly to 5100 S/cm ± 250 S/cm after 500 cycles at 100% strain. The high electrical conductivity of the composites can be explained by the high silver nanoparticle concentration distributed in and around the elastomeric fiber matrix. In addition, the elastomeric fiber matrix helps to sustain a significant portion of the electrical conductivity under cyclic tensile deformation by facilitating the formation of alternative conductive pathways.

5.2 Experimental

5.2.1 Synthesis of poly(acrylic acid) capped silver nanoparticles

Poly(acrylic acid) (PAA) capped silver nanoparticles were synthesized using $AgNO_3$, monoethanolamine (MEA), and PAA. Initially, 100 mmol $AgNO_3$ (Sigma-Aldrich, 99%), 400 mmol MEA (Sigma-Aldrich, 99%), and 7.2 ml PAA (Acros Organics, 50 wt % water solution) were dissolved in 75 ml deionized water and stirred for 30 minutes. The solution was placed in an oil bath with temperature set to 60 °C and rigorously stirred for 2 hours. The particles were precipitated using 250 ml ethanol (Pharmco-Aaper, 99%), and washed several times with ethanol to remove excessive reagents. The resulting nanoparticles were dried under vacuum at 60 °C for 24 hours.

5.2.2 Elastic conductor fabrication

Solution blow spinning solutions consisting of PAA capped nanoparticles, poly-(styrene-block-isoprene-block-styrene) (SIS) (Sigma-Aldrich, 22% wt/wt styrene content), and tetrahydrofuran (THF) (Fisher Scientific, 99.9%) were prepared and fed with a constant rate (10 ml/h) through the nozzle of the solution blow spinning apparatus. The apparatus was constructed from a flat tipped 18G needle, syringe pump, and compressed air-line. The air pressure has kept constant at 50 psi during the deposition process. The composite mat was deposited on a mesh, which was then immersed into an organometallic solution consisting of silver trifluoroacetate (STFA) (Sigma-Aldrich, 98%) and ethanol (Pharmco-Aaper, 99%) for 30 minutes. The STFA concentration in ethanol is kept at 25% (wt/vol) for each composite mat. Because this

precursor concentration has enabled fabrication of elastic conductors with highest electrical conductivity combined with less variability in electrical properties and elongation at break. The swollen mat was them vacuum dried in a desiccator. The nucleation of the second silver nanoparticle network was initiated with a reducing solution consisting of hydrazine hydrate (50% (vol/vol)) (Sigma-Aldrich, 50%-60%), deionized water (25% (vol/vol)) and ethanol (25% (vol/vol)). The resulting conductive composites were rinsed thoroughly with water to wash away any unbound nanoparticles and dried under vacuum for 24 hours.

5.2.3 Characterization

Scanning electron microscopy (SEM) (Hitachi SU-70) and Transmission Electron Microscopy (TEM) (JEOL 2100F) were used to characterize the structure of the block copolymer nanoparticle composites. The TEM sample used for cross-section analysis was prepared using a cryo-microtome (Leica EM UC-6) with a 100 nm sample thickness. Nanoparticle diameter is reported as an average of 150 measurements taken from three TEM images (Figure C.1). A dynamic mechanical analyzer (TA Instruments Q800) was used to characterize the mechanical properties of the elastic conductors. Energy dissipation was calculated from the area of the hysteresis loops of cyclic stress/strain curves for both SIS fiber mats and conductive composites (n=3, error bars represent standard deviation). Thermogravimetric analysis was performed under nitrogen to identify the volume fraction of silver in the composite (Netzsch F3 Jupiter). The electrical conductivity of the elastic conductor samples were measured using a home made automated 4-point probe measurement system connected to a Keithey 2400

Sourcemeter (n=5, error bars represent standard deviation). The normalized conductivity measurements under mechanical strain were performed using a custom built electromechanical characterization system consisting of a motorized stage with built-in 4- point probe measurement system connected to Agilent 34420A Micro-Ohm Meter, and National Instruments PXI4065 Digital Multimeter (n=3, error bars represent standard deviation) (Figure C.2). The conductivity of the stretchable composites was measured after each stretching step corresponding to 0.25% strain for samples with a size of 0.25 inch.

5.3 Results and Discussion

Elastic conductors were fabricated by a multistep process consisting of synthesis of poly(acrylic acid) capped silver nanoparticles (Ag-PAA) followed by the preparation of an Ag-PAA containing polymer solution and subsequent deposition of a composite fibrous network through solution blow spinning. An organometallic precursor solution was then infused into the material and reduced to form a second population of silver nanoparticles, this resulted in the formation of a conductive composite (i.e. elastic conductors).

A freestanding composite polymer fiber mat containing Ag-PAA is shown in Figure 5.1a showing similar morphology to SIS polymer fiber mats Figure 5.1b. Polymer fiber generation through this method only requires a simple apparatus, high-pressure gas source, and viscous spinning solution.[147, 150] Similar to other solution-processed fiber spinning techniques, fiber geometry is achieved after exceeding a critical solution concentration, resulting in polymer chain overlap.[150] The inclusion of inorganic

nanoparticles into the spinning solution can alter optimal spinning parameters.[167] The use of poly(acrylic acid) capping on silver nanoparticles enabled dispersion of nanoparticles in the spinning solution, allowing for the generation of fiber morphologies up to a critical nanoparticle concentration. The solutions prepared with Ag-PAA concentrations exceeding 35% (wt/vol) did not generate a fibrous morphology under the same deposition conditions. This limit can be attributed to high solution viscosity leading to clogging at the spinning apparatus.

After polymer deposition, the fiber mats were immersed in an organometallic precursor solution. The composite fiber mats swelled drastically (310% increase in weight of the dry mat after swelling) without releasing silver nanoparticles. The weight of the dry fiber mat only increased by 10% when the organometallic precursor was not present in the solution. This preferable interaction between the precursor solution and SIS is explained by attraction between charged transition metal ions and unsaturated hydrocarbons, such as positively charged silver ions and the double bonds contained in the isoprene block of SIS.[151] In the final step, a conductive network of silver nanoparticles was formed throughout the composite material through the introduction of a reducing solution (Figure 5.1 c-d).

Structural characterization performed by scanning electron microscopy (SEM) showed that the ability to form a fiber network is maintained after addition of Ag-PAA into the spinning solution up to a concentration of 35% (wt/vol) (Figure 5.1e). The average diameter of the composite block copolymer fibers was found to be 1.88 ± 0.5 μm, which is comparable to block copolymer fibers spun from a solution simply containing SIS (1.66 ± 0.7 μm) (Figure 5.1e, f). The Ag-PAA forms chain-like

assemblies in the fibers; this potentially results from the direction of flow during the solution blow spinning process (Figure 5.1e-inset). After the introduction of the organometallic precursor and subsequent nucleation by the addition of a hydrazine hydrate solution, a silver nanoparticle network forms around the composite block copolymer matrix generating conductive pathways (Figure 5.1g). This nanoparticle network covers the entire surface of the composite fibers prepared from a spinning solution with 35% (wt/vol) Ag-PAA concentration (Figure 5.1g). For these conductive composites, it becomes difficult to identify the fiber morphology after nucleation (Figure 5.1g), which remains visible for composites prepared using block copolymer fiber mats that do not contain Ag-PAA (Figure 5.1h). This is potentially due to higher accumulation of precursor solution for fiber mats containing Ag-PAA (310% weight increase) relative to block copolymer mats deposited using SIS alone (190% weight increase). In addition, TGA analysis performed on the elastic conductors demonstrated that elastic conductors containing Ag-PAA could establish filler concentrations (81wt%, 27.4% (vol/vol)) higher than elastic conductors without Ag-PAA (52%wt, 8.8% (vol/vol)) (Figure C.3). The cross-section TEM image of these elastic conductors revealed that silver nanoparticles also nucleate in between the existing Ag-PAA in the fiber cross-section (Figure 5.1g-inset, Figure C.1c) This is in contrast to the mats not containing Ag-PAA, which is limited to nanoparticle nucleation at fiber surface (Figure 5.1h-inset). This result indicates that Ag-PAA facilitates silver nanoparticle nucleation in block copolymer fibers. The size distribution of Ag-PAA and silver nanoparticles in elastic conductors were measured using cross-section TEM images as 150 nm ± 50 nm and 37.6 ± 14.2 nm, respectively (Figure 5.1h-inset, Figure C.1c).

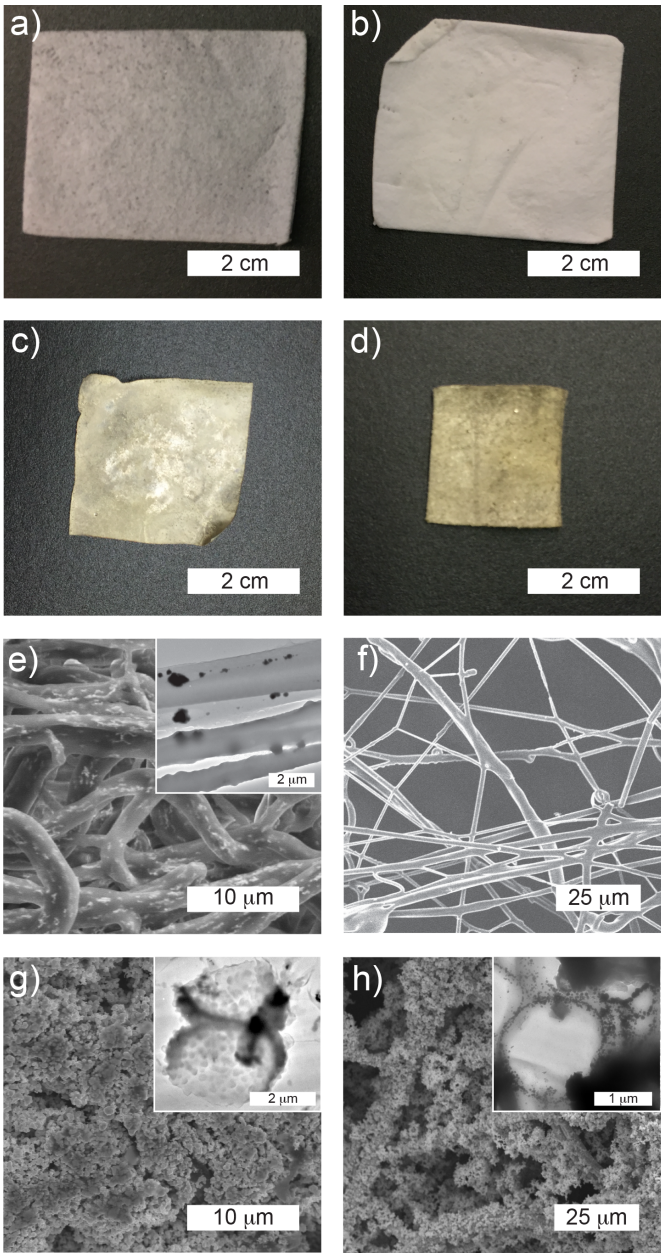

Figure 5.1 a) Images of a composite blow spun fiber network, b) freestanding block copolymer blow spun fiber network, c) elastic conductor with Ag-PAA, d) elastic conductor without Ag-PAA. e) SEM images of a composite blow spun fiber network, f) freestanding block copolymer blow spun fiber network, g) elastic conductor with Ag-PAA, h) elastic conductor without Ag-PAA. e) TEM image of composite fiber network, g) cross-section TEM image of elastic conductors with Ag-PAA and h) without Ag-PAA are provided in the inset.

The mechanical properties of elastic conductors prepared using spinning solutions with different Ag-PAA concentrations were characterized to investigate the influence of nanoparticle content on tensile modulus, and elongation at break. Increased Ag-PAA concentration in the spinning solutions of elastic conductors resulted in more brittle composites with lower elongation at break (Figure 5.2a), and higher tensile modulus (Figure 5.2b). The effect of Ag-PAA concentration on overall conductivity and strain dependence of electrical properties was also assessed. Maximum conductivity values reached 9000 ± 200 S/cm when testing composite fiber mats with the highest Ag-PAA concentration (35% (wt/vol) in the spinning solution) that could be deposited in a fibrous morphology. Electrical conductivity measurements during tensile deformation revealed that these elastic conductors with high volumetric fraction of silver (27.4% (vol/vol) (Figure C.3) can maintain 52% of their initial conductivity (σ_0) prior to mechanical failure at 302% strain (Figure 5.2d). The electrical conductivity dependence on tensile strain increased drastically with decreasing Ag-PAA concentration, as elastic conductors fabricated using spinning solutions with only 10% (wt/vol) Ag-PAA lost 99% of their initial conductivity at 300% strain (Figure 5.2d).

A small increase in electrical conductivity with increasing tensile strain was observed for elastic conductors at strain values reaching 70%. This can be explained by strain mediated stiffening effects and the fiber network structure of the elastic conductors (Figure 5.2d).[38] Strain induced stiffening effects are known to generate a denser nanoparticle distribution in the polymer matrix leading to higher electrical conductivity for polymer-nanoparticle composites during tensile deformation.[38, 168] Another explanation for this material behavior is the fibrous network structure of the block

copolymer matrix. The electrical conductivity of fiber networks can increase under tensile strain, due to increased number of fiber-to-fiber contacts.[165] Elastic conductors with higher nanoparticle content extend this trend up to higher strain values (Figure 5.2d) because they are potentially able to establish more conductive pathways that can be rearranged to increase the number of fiber-to-fiber or particle-to-particle contacts during tensile deformation.[38, 165]

Changes in electrical conductivity under cyclic deformation were also evaluated by deforming elastic conductors with various Ag-PAA concentrations to 100% strain for 500 cycles (Figure 5.2e, f). The elastic conductors composed of high concentrations of Ag-PAA (35%, 30%, 25% (wt/vol) in the spinning solution) maintained at least 70% of their initial conductivity (Figure 5.2e) after cyclic testing. This is in contrast to elastic conductors consisting of low concentrations of Ag-PAA (20%, 15%, 10% (wt/vol) in the spinning solution), which decreased more drastically with consecutive tensile strain cycling (Figure 5.2e). Electrical conductivity values at 100% strain for elastic conductors with low Ag-PAA content deteriorated to below 20% of their initial conductivity after 10 cycles of tensile deformation up to 100% strain (Figure 5.2f).

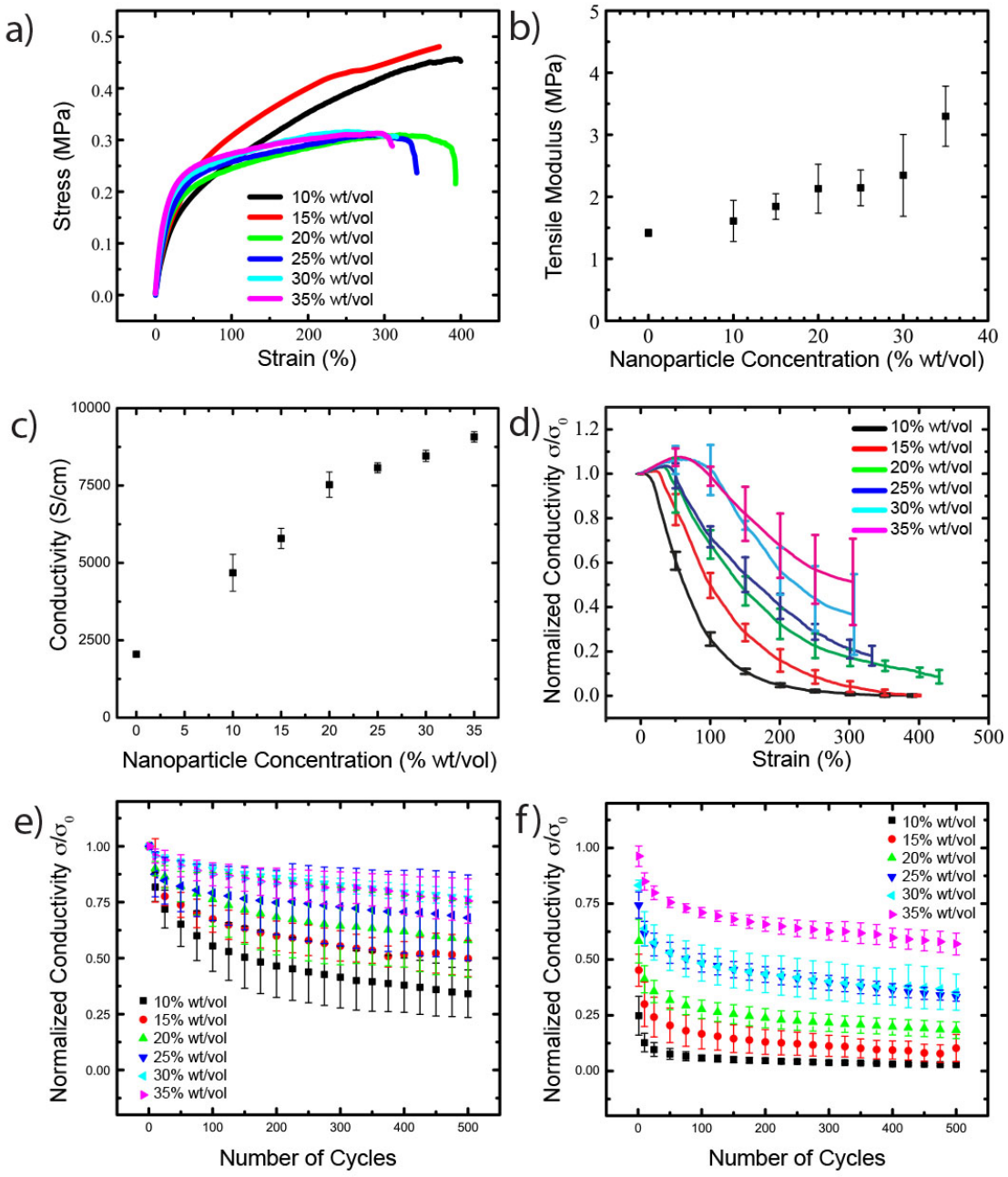

Figure 5.2 a) Stress/strain curves and b) tensile modulus, c) electrical conductivity of elastic conductors prepared using spinning solutions with different Ag-PAA concentrations. d) Normalized electrical conductivity (σ/σ_0) values for elastic conductors prepared using spinning solutions with different Ag-PAA concentration under uniaxial tensile strain. Normalized electrical conductivity values at e) released state (0% strain) and f) stretched state (100% strain) for elastic conductors prepared using spinning solutions with different Ag-PAA concentration as a function of cycle number. (n=3 for all groups, error bars represent standard deviation).

Further mechanical characterization of the conductive composites was performed using stress/strain cycling to evaluate the extent of plastic deformation (Figure 5.3a, b). The elastic conductors prepared using higher Ag-PAA concentrations demonstrated a slightly lower elastic recovery in comparison to elastic conductors fabricated using low Ag-PAA concentrations (Figure 5.3a, b, Figure C.4). Energy dissipation values were calculated from the area under the stress/strain curve at each maximum strain value. Linear correlations of energy dissipation with increasing strain correspond to structural deformation mechanisms (Figure 5.3c, d, Figure C.5).[86, 153, 154] Elastic conductors fabricated from composite mats with low Ag-PAA concentrations (20%, 15%, 10% (wt/vol) in the spinning solution) demonstrated three distinct regions corresponding to strain induced structural changes, which has been established for fibrous polymer-nanoparticle composites (Figure 5.3c, Figure C.5a, b).[86] The initial structural changes originate from breakage of fiber-to-fiber junctions established during silver nanoparticle nucleation up to tensile strain of 50%. As the fibers gain sufficient freedom to be rearranged for strain values higher than 50%, the structural deformations generate a less drastic increase in energy dissipation along the second strain region until reaching 100% strain. Individual fiber deformation dominates the structural deformation for strain values exceeding 100%, this results in an increased rate of energy dissipation due to loss of filler to polymer and filler-to-filler contact. In contrast, elastic conductors prepared using high Ag-PAA concentrations (35%, 30%, 25% (wt/vol) in the spinning solution) demonstrated a single linear correlation region with higher slope. This continuous increase in energy dissipation can be explained by the physical interpretation of strain softening effect (Mullins effect) for composites with high filler

concentration, which occurs for strain values higher than elastic tensile deformation limit.[169, 170] The physical models developed to describe the Mullins effect in elastomeric nanocomposites consist of deformation mechanisms including rupture of bonds between nanoparticles and polymer, rearrangement of nanoparticles, and detachment of nanoparticles.[169] The dominant structural deformation mechanism for composites consisting of high filler concentration is detachment of particle-to-particle contacts (Figure 5.3d, Figure C.5c, d).[170]

Electron microscopy was used to further investigate the difference in deformation mechanisms between low and high nanoparticle loading composites. Elastic conductors with differing Ag-PAA concentrations were imaged under 0%, 50%, and 100% strain to visualize differences in the progression of the material's morphology under strain (Figure 5.4). The SEM images of elastic conductors assembled using fiber spinning solutions with 10% (wt/vol) Ag-PAA show that these composites demonstrate the deformation mechanics of fibrous polymer-nanoparticle composites (Figure 5.4a, b, c).[86] The SEM images of these elastic conductors at 50% strain indicates that fibers orient along the direction of tensile deformation by breaking fiber-to-fiber junctions, as the majority of the nanoparticles covering the surface remains intact (Figure 5.4b). At 100% strain, the fibers orient completely in the direction of tensile strain, and surface coverage of nanoparticles becomes discontinuous, indicating the onset of individual fiber deformation (Figure 5.4c). Whereas the fibrous network structure of elastic conductors prepared using fiber spinning solutions with 35% (wt/vol) Ag-PAA concentration is not discernible at 0% strain, as the surface is completely covered with silver nanoparticles (Figure 5.4d). At 50% strain, the fiber network structure becomes

visible in between the cracks that are formed during deformation (Figure 5.4e). The SEM images of these highly conductive elastic conductors under 100% strain indicate this fiber network stabilized with particle-to-particle contact detach into individual fibers with discontinuous nanoparticle coverage. This also supports the single mode of structural change, loss of particle-to-particle contacts, shown previously by a linear increase in energy dissipation with strain.

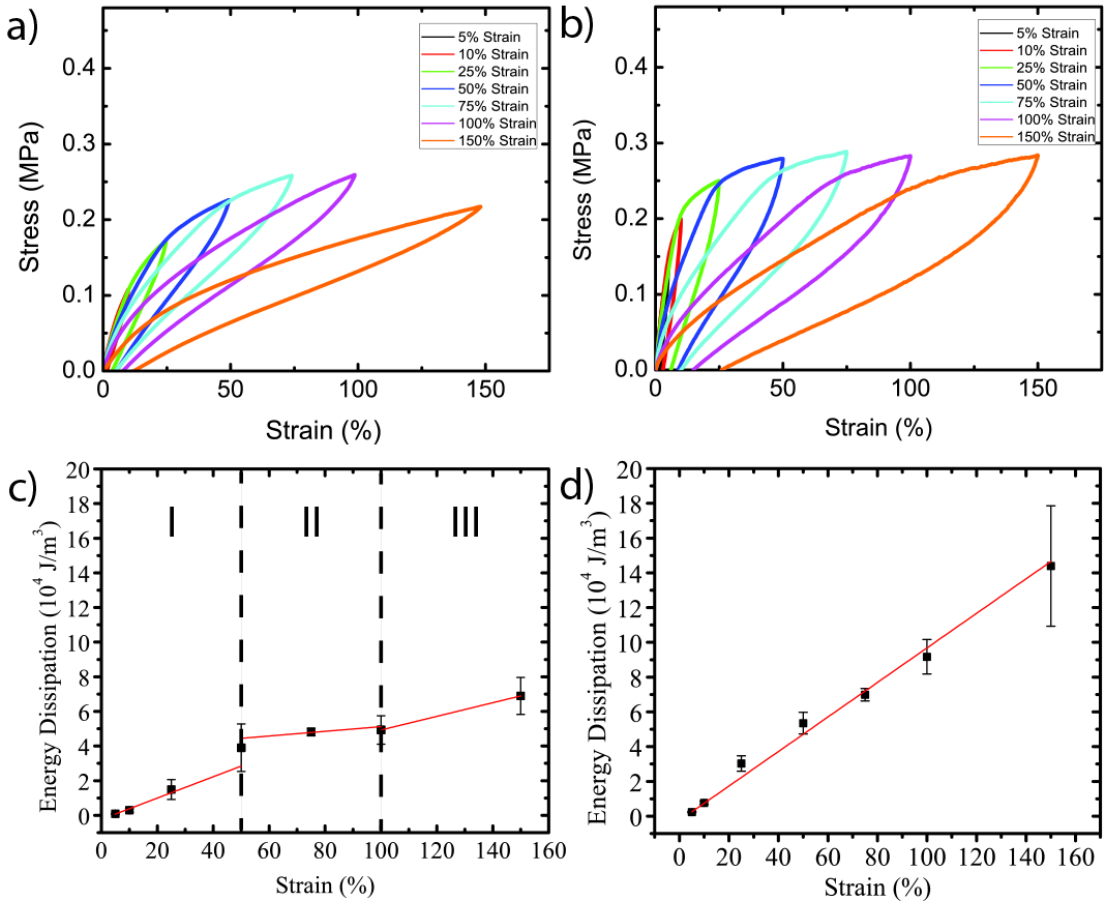

Figure 5.3 Stress/strain cycling curves for elastic conductors prepared using spinning solutions with a) 10% (wt/vol) and b) 35% (wt/vol) Ag-PAA concentration. Average energy dissipation values and corresponding linear fits for elastic conductors prepared using spinning solutions with c) 10% (wt/vol) and d) 35% (wt/vol) Ag-PAA concentration (n=3 for energy dissipation data, error bars represent standard deviation).

To visualize these structural deformations of the elastic conductors with high Ag-PAA concentration in a broader perspective, low magnification SEM images were acquired under strain values of 0%, 25%, 50%, and 100% (Figure C.6). The unstrained condition shows a composite surface densely covered by silver nanoparticles (Figure C.6a). As this composite is stretched to slightly above its elastic deformation limit, it begins to form cracks separating large blocks of conductive composites, yet still the majority of the composite remains connected with nanoparticles (Figure C.6b). Once, the strain values reached 50% strain, the number of cracks and separation between large composite blocks increases (Figure C.6c). The conductive fiber networks, which were previously demonstrated in the high magnetization SEM images, connect these large composite blocks during deformation (Figure C.6c). This highlights the influence of fiber network on the strain-dependent electrical properties of elastic conductors at strain values exceeding elastic deformation limit (20% strain). Further stretching of elastic conductors reaching strain values of 100% resulted in a morphology consisting smaller conductive composite blocks connected with individual fibers with discontinuous nanoparticle coverage, as highlighted by the low and high magnification SEM images (Figure C.6d, Figure 5.4f).

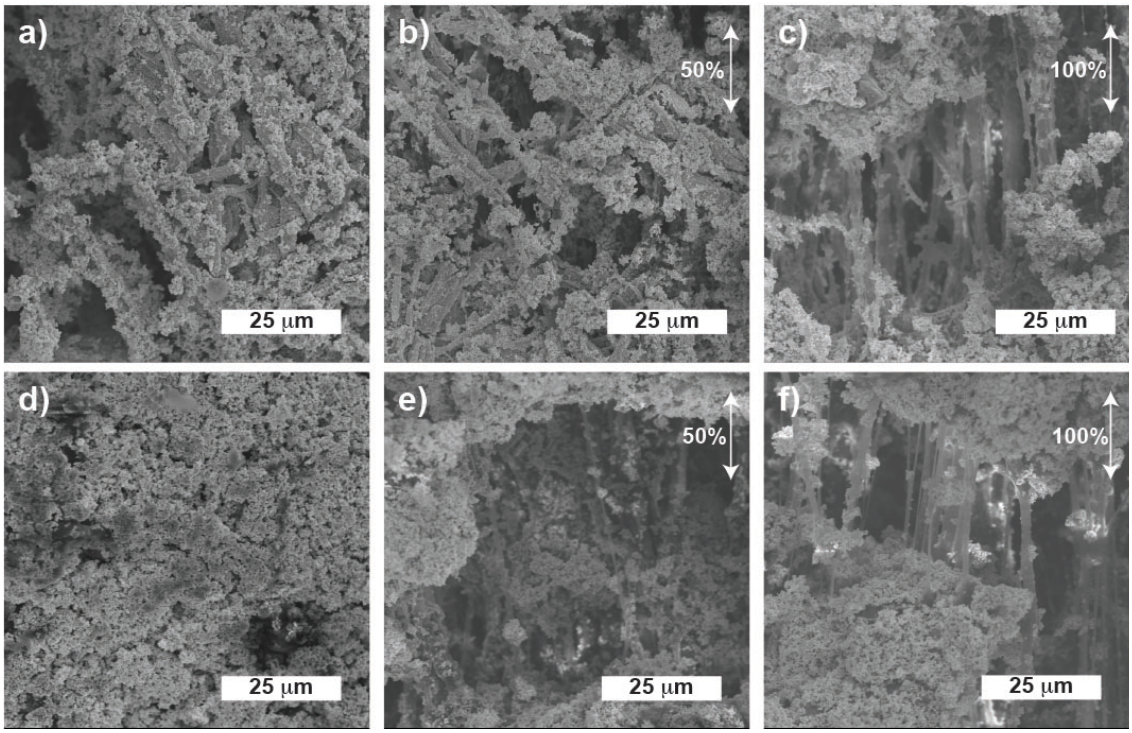

Figure 5.4 SEM images of elastic conductors prepared using spinning solutions with 10% (wt/vol) Ag-PAA concentration under a) 0% strain, b) 50% strain, c) 100% strain. SEM images of elastic conductors prepared using spinning solutions with 35% (wt/vol) Ag-PAA concentration under d) 0% strain, e) 50% strain, f) 100% strain. The arrows indicate the direction of uniaxial tensile strain.

5.4 Conclusions

We have demonstrated solution-processed elastic conductor with high nanoparticle loading by employing large silver nanoparticles (150 nm ± 50 nm) in a spinning solution generate a fibrous composite template for initiating a secondary silver nanoparticle nucleation (37.6 ± 14.2 nm). The resulting materials reach conductivity values of 9000 S/cm that only decreases to 4900 S/cm after 500 cycles of 100% strain. The high electrical conductivity of these composite materials originates from the high volumetric fraction of conductive fillers (27.4% vol/vol) that are assembled in and around the elastomeric fiber matrix of SIS. The random fibrous network structure of

these composites stemming from elastomeric fiber matrix also helps them to sustain significant portion of their electrical conductivity during cyclic tensile deformation. We have additionally demonstrated control over strain-dependent electrical properties of the elastic conductors by decreasing the Ag-PAA concentration employed in elastic conductors. This versatility enables adjusting material properties for specific applications.

Chapter 6: Outlook and Future Directions

6.1. Outlook

In this work we have demonstrated synthesis of magnetic nanostructures with high saturation magnetization and low coercivity to prepare flexible magneto-dielectrics with high permeability, high permittivity and low dielectric, and magnetic loss at microwave frequencies (1 MHz to 6 GHz). In addition, we have established a fabrication method for depositing highly conductive polymer-nanoparticle composites with strain-stable electrical properties on non-uniform surfaces. These two distinct projects investigating polymer-nanoparticle composites for different applications has paved the way towards new possibilities to further improve the properties and utility of polymer-nanoparticle composites as flexible magneto-dielectrics, and stretchable conductors.

6.2. Solvent studies in magneto-dielectric composites

While surface functional groups govern the interactions between nanoparticles and polymers at lower nanoparticle concentrations, the mobility of nanoparticles becomes more restricted with increasing filler concentration. This results in conductive losses due to aggregation of nanoparticles in polymer matrix. The aggregation also increases the viscosity of polymer-nanoparticle mixture prior to cross-linking of polymer matrix, which hinders the ability to process composites in desired form or shape. These restrictions limit the achievable nanoparticle concentration, consequently ultimate magneto-dielectric properties of the composite. A detailed investigation on the influence of various solvents on the viscosity of polymer-nanoparticle mixture prior to

curing might result in an enormous increase in achievable filler concentration. The improved concentration of fillers can drastically increase permeability of the flexible magneto-dielectric composites, without increasing magnetic loss values.

6.3. Composites with magnetoelectric properties

Magneto-dielectric composites consisting of magnetic filler materials and polymer matrix demonstrate high permeability, high permittivity and low electromagnetic loss. However, these properties are inherently constant for magneto-dielectric composites, unless they exhibit magnetoelectric effect.[6, 171] Magnetoelectric materials exhibit electrical properties that can be altered using a magnetic field (direct magnetoelectric effect) or magnetic properties that can be changed using an electric field (converse magnetoelectric effect).[171] These magnetoelectric effects can be established using various material approaches including dispersing magnetic nanomaterials in a polymer matrix.[172] Similar to magneto-dielectric properties, magnetoelectric response of the polymer nanoparticle composites are highly dependent on the magnetic properties of the filler materials, the magnetic filler concentration, the interface between magnetic fillers and polymer.[172-175] A detailed study on magnetoelectric properties of the magneto-dielectric composites proposed in this dissertation will be useful for demonstrating functional materials with tunable permeability and permittivity using magnetic or electric fields. In addition, employing a ferroelectric polymer like poly[(vinylidenefluoride-co-trifluoroethylene] (P(VDF-TrFE)) as a matrix can help improve the magnetoelectric response of these composites. Adequate separation of the fillers in P(VDF-TrFE) matrix can be accomplished by solution processing and high energy sonic bath processing. After nanoparticles are uniformly dispersed in P(VDF-

TrFE) solution, it is possible to cast composite films into molds and remove the solvent by heating under vacuum. The resulting materials can be prepared using different nanoparticle concentrations, which can help develop a correlation between magneto-dielectric properties and the magnetoelectric coefficient of the composites. In addition, electron microscopy studies, magnetic loss, and dielectric loss measurements can help identify the distribution of nanomaterials in the ferroelectric polymer matrix. This investigation is particularly important, as the aggregation of nanomaterials deteriorates magnetoelectric effect in these composites.[172] These magnetoelectric composites with tunable permittivity and permeability can be utilized in micro patch microwave antennas to establish radio frequency communication devices with tunable electromagnetic response.

6.4. Polymer composites with magnetically controlled filler distribution

The demonstration of in-fiber percolation to improve the quantity of conductive pathways has proven to be effective, but simply dispersing nanoparticles in spinning solution provides limited control over nanoparticle distribution in the fibers. Employing magnetic forces to gain control over nanoparticle distribution in polymer fibers can expand the vision of the fabrication method designed to deposit elastic conductors. A solution blow-spinning setup with a controlled magnetic field system can help aligning and guiding magnetic nanoparticles in fibers during the spinning process. This controlled alignment of nanoparticles in polymer matrix can help further decreasing the percolation threshold of polymer-nanoparticle composites, and consequently improving conductivity. In addition, the magnetic field as a parameter can also be employed to

alter the separation between magnetic nanoparticles in fibers, which can be employed to fabricate composites with high magnetic anisotropy.

Moderate magnetic fields can be established using a Helmholtz coil, which provides control over field intensity using current. Due to moderate magnetic field conditions, it is necessary to employ magnetic nanoparticles with low coercivity to establish control over nanoparticles. It is also important to align the spinning tip with the magnetic field generated by Helmholtz coil, as the field intensity is only homogeneous at the center of the coil. To properly perform this alignment, it is necessary to conclude a detailed study involving structural characterization of fibers fabricated with different distances between the spinning tip and the center of the Helmholtz coil. This study will also provide insight regarding the balance between magnetic forces and molecular interactions governing the structure of the composite fibers.

6.5. Transparent Stretchable Electrodes

Polymer-nanoparticle stretchable conductors can also be fabricated using transparent SIS films with thicknesses smaller than 10 μm. Initial studies we performed have demonstrated homogeneous nanoparticle nucleation throughout the entire cross-section of the polymer film. The resulting composite achieved electrical conductivity values reaching 1620 S/cm. The next step can be identifying parameters including optimum precursor solution concentration and minimum pattern feature size for the proposed stretchable conductor system. Because these parameters will be unravel the potential of these composites as transparent electrodes.

Film thickness and styrene content are expected to have major implications in stretchable transparent electrode fabrication that can be attributed to differences in nanoparticle nucleation. It is also possible to investigate film-casting parameters including styrene content of SIS and film thickness, which can be quantified using ellipsometry. After identification of the correlation between styrene content, spinning speed, spinning duration, and solution concentration with film thickness, it is essential to initiate a study on conductivity, transparency, and mechanical properties of transparent conductors processed using different film thicknesses. This work will be detrimental for establishing an optimal film thickness. This optimal thickness can help identifying the critical diffusion length of reducing agent for each SIS polymer with different styrene content. Once the optimal thickness for each SIS block copolymer is determined, it will be possible to start characterization of the mechanical properties of the composite film and the stability of the electrical conductivity during continuous strain cycling.

Chapter 7: Contributions

The research described in this dissertation has resulted in two publications that are in press or accepted and three publications that are currently in the preparation or submission processes. This same work has been presented 7 times at different conferences, and workshops organized by Materials Research Society, Applied Power Electronics Conference, and Mid-Atlantic Soft Matter Workshops. The studies on magneto-dielectric materials presented in Chapter 2 have provided a different material approach on miniaturization of microwave devices by investigating deformable composites. This work was highlighted on *Bloomberg Channel*. In addition, the investigation on conductive polymer-nanoparticle composite fabrication presented in Chapter 4 was the first study to demonstrate direct deposition and patterning of elastic circuits on the non-uniform substrates. This fabrication method has been covered as a story in Engineering.com and the University of Maryland Nanocenter website.

Appendices

Appendix A: Nanostructured Flexible Magneto-dielectrics

Elemental Analysis of Oxide Growth in Nanoparticles

Energy Dispersive X-ray Spectroscopy (EDS) of individual Fe/citrate and Fe/Ag core–shell nanoparticles was used to evaluate the possible oxide layer growth. The oxidation characteristics of Fe nanoparticles with a citrate shell were investigated by exposing thermally annealed and non-annealed samples in ambient atmosphere at room temperature for 6 months. The EDS analysis shows that the non-annealed Fe nanoparticles are resistant to oxidation with their citrate shell remaining intact (Figure A.1a). However, the annealed Fe nanoparticles develop an oxide shell in the absence of the citrate shell over this time period. (Figure A.1b).

EDS analysis also reveals that thermal annealing aids in preventing oxidation of Fe/Ag core-shell nanoparticles. The Fe/AG core-shell nanoparticles remain unoxidized up to a week prior to thermal annealing (Figure A.2a). However, the discontinuous Ag shell layer of the Fe/Ag core-shell nanoparticles allows slow oxidation of the Fe core (Figure A.2b). As a result of slow oxidation, the oxide formation is detectable for core-shell nanoparticles that are not annealed and kept in ambient atmosphere for 6 months (Figure A.2b). Thermally annealed Fe/Ag core-shell nanoparticles that form the Fe/Ag heterostructures show no further oxidation after 6 months (Figure A.2c). Thermal annealing leads to a thicker and continuous Ag shell that provides better protection against oxidation.

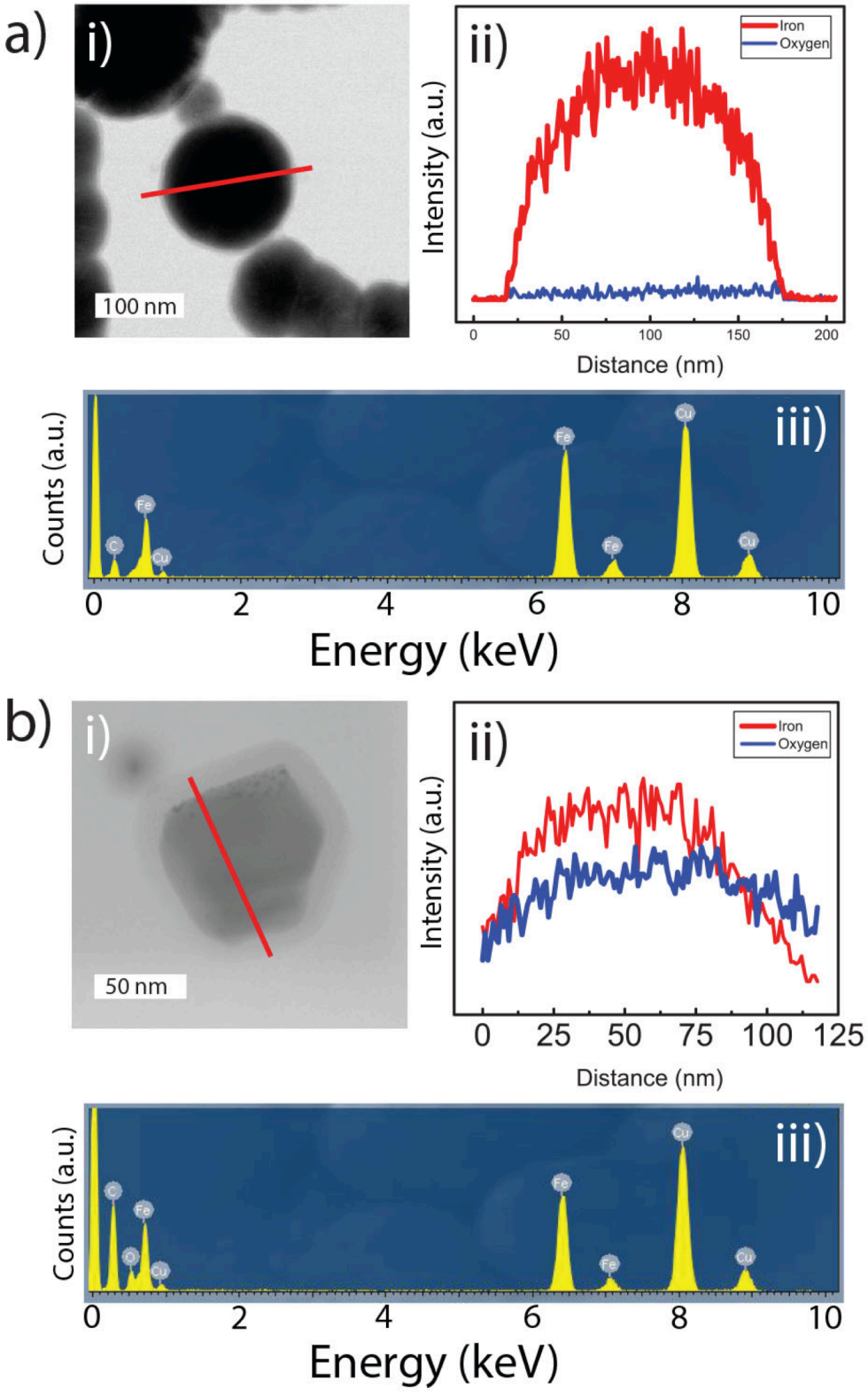

Figure A.1 a) Scanning Transmission Electron Microscope (STEM) image (i), EDS elemental line scan (ii), EDS energy spectrum (iii) of non-annealed Fe/citrate nanoparticle. b) Scanning Transmission Electron Microscope (STEM) image (i), EDS elemental line scan (ii), EDS energy spectrum (iii) of annealed Fe/citrate nanoparticle.

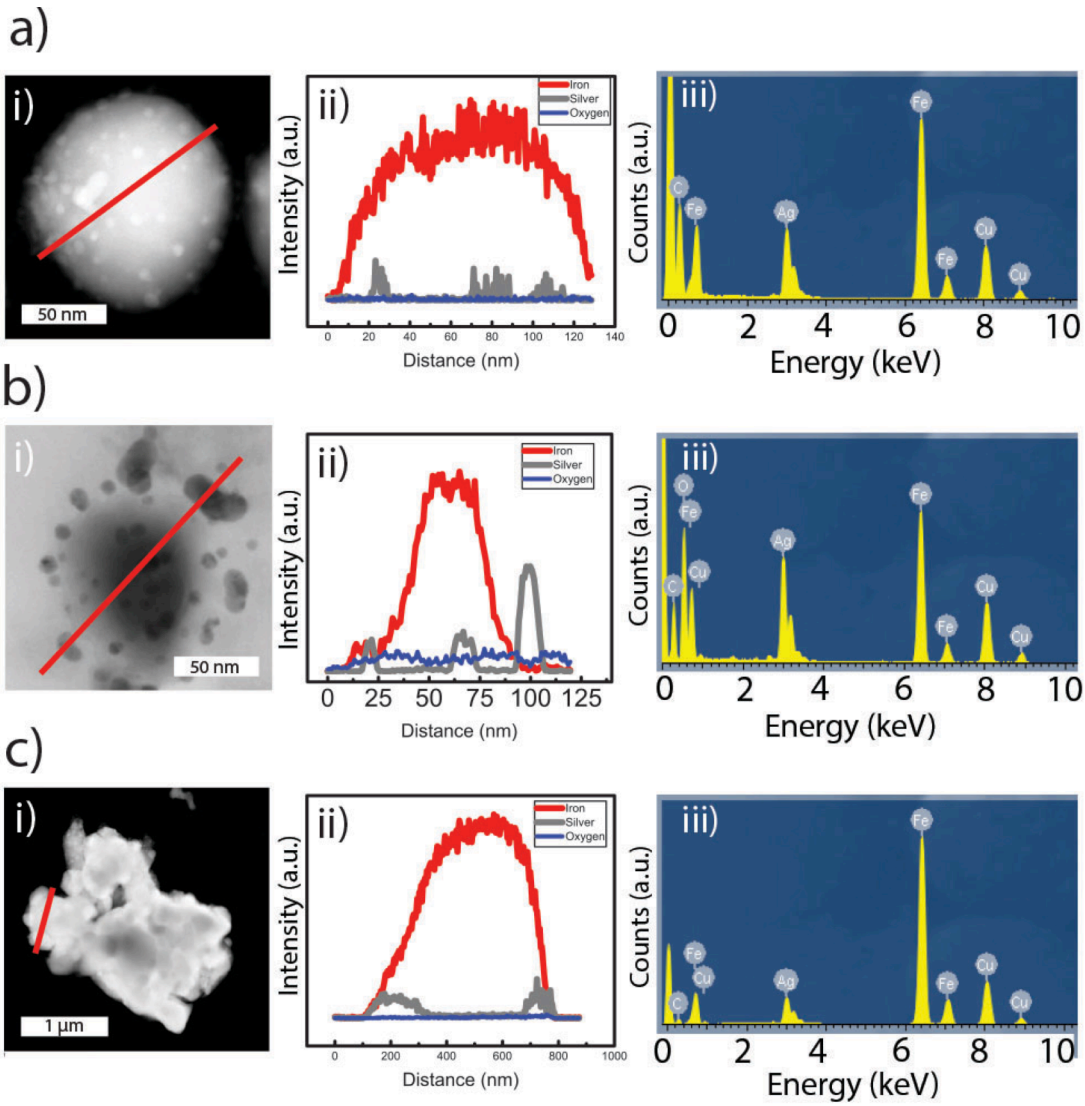

Figure A.2 a) Scanning Transmission Electron Microscope (STEM) image (i), EDS elemental line scan (ii), EDS energy spectrum (iii) of Fe/Ag core shell nanoparticle (1 week after synthesis). b) Scanning Transmission Electron Microscope (STEM) image (i), EDS elemental line scan (ii), EDS energy spectrum (iii) of Fe/Ag core-shell nanoparticle (6 months after synthesis). c) Scanning Transmission Electron Microscope (STEM) image (i), EDS elemental line scan (ii), EDS energy spectrum (iii) of Fe/Ag heterostructures (6 months post synthesis).

Embedded-Trough Patch Radio Frequency Antennas

The device performance of flexible magneto-dielectric composites was tested by fabricating embedded-trough patch antennas with Fe/citrate nanoparticle and Fe/Ag nanoparticle heterostructure composites (75 wt% nanoparticle loading). The flexible magneto-dielectric composites were placed in the trough of a patch antenna as illustrated at Figure A.3a and the reflected intensity spectrum was measured (Figure A.3b). The RF patch antenna with Fe/citrate nanoparticle composite placed in the trough has a bandwidth of 12% at -10 dB. The bandwidth of the RF patch antenna with Fe/Ag heterostructure composites was measured as 9.6% at -10 dB. The slightly higher bandwidth demonstrated by the Fe/citrate nanoparticle composite could be attributed to a higher μ/ε ratio. The RF antennas exhibit resonance at 1.7 GHz for the Fe/citrate nanoparticle composite trough and 1.9 GHz for the Fe/Ag heterostructure composite trough. The resultant size reduction percentages, as calculated from the resonance frequencies of equal length troughs, are 44% for Fe/citrate nanoparticle composites and 38% for the Fe/Ag core-shell nanoparticle composites.

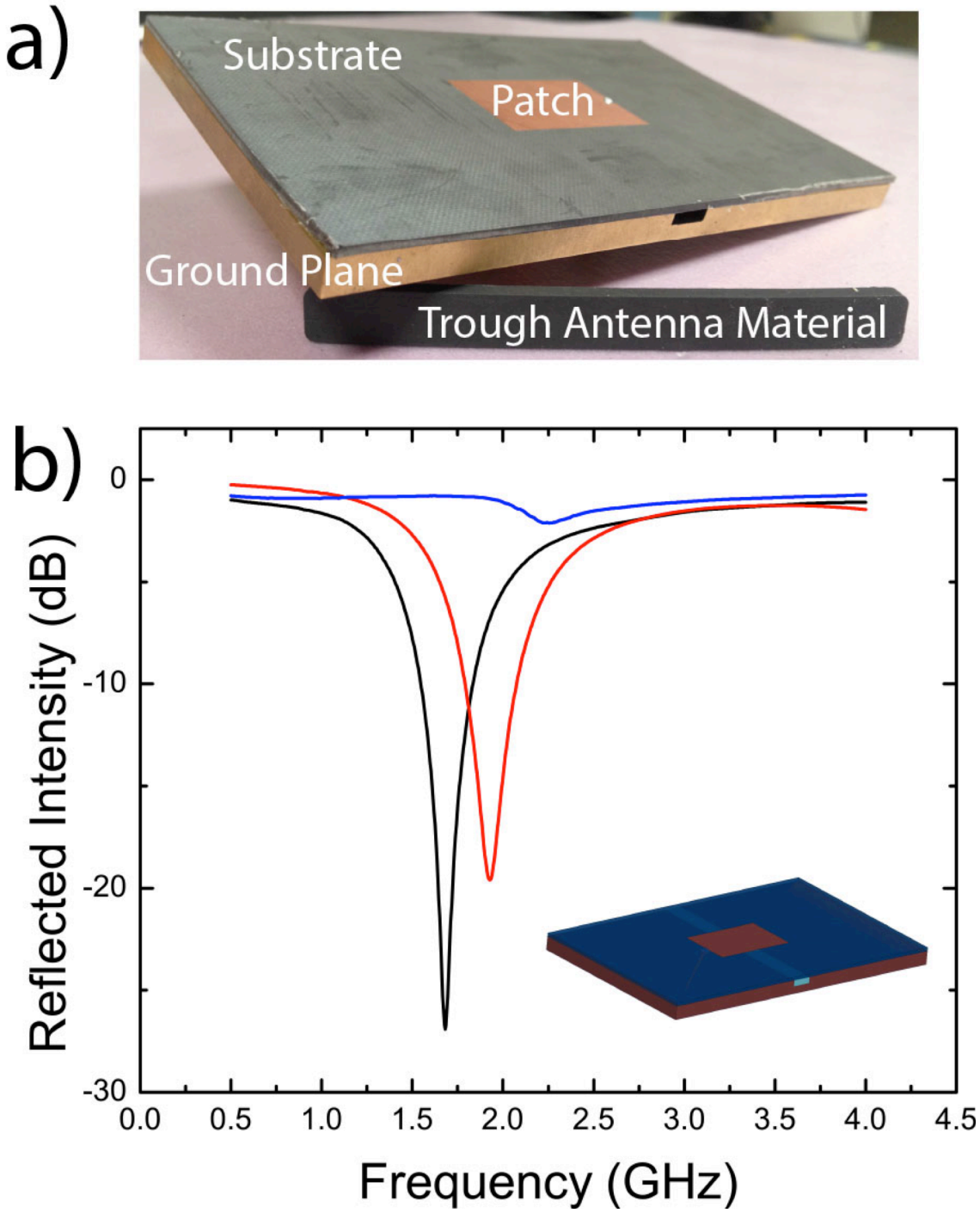

Figure A.3 a) Image of embedded trough radio frequency antenna assembly. b) Reflected electromagnetic intensity spectrum for RF antennas with air filled trough (blue), Fe/citrate nanoparticle composite filled trough (black) and Fe/Ag heterostructure composite filled trough (red).

Appendix B: Sprayable Elastic Conductors

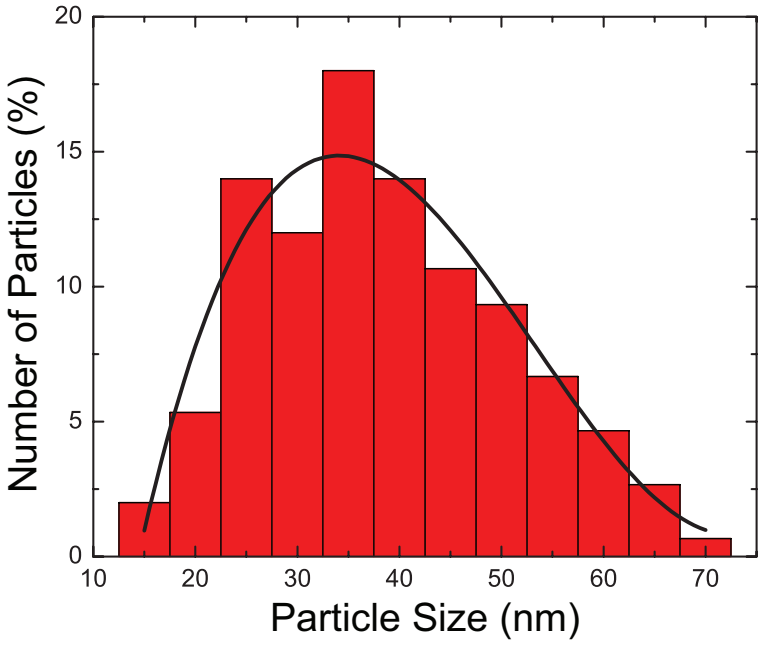

Figure B.1 Nanoparticle size distribution as measured by TEM (n=150).

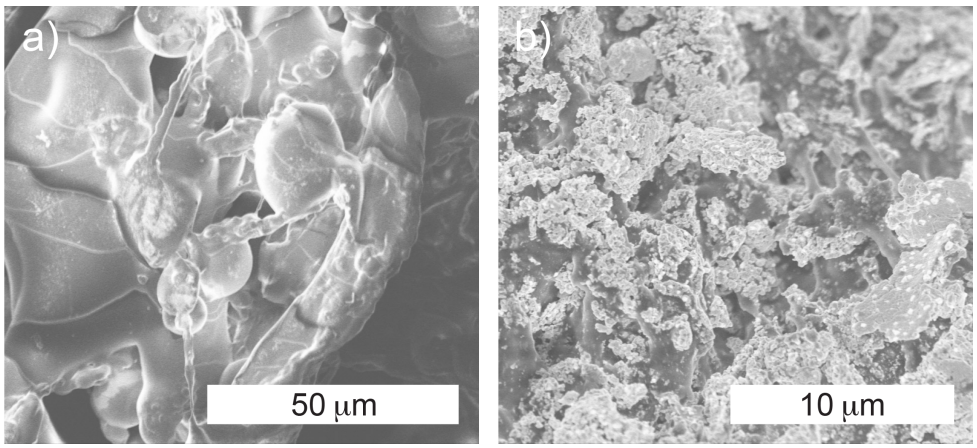

Figure B.2 Fiber structure was irreversibly lost during the fabrication process for SIS block copolymers with a styrene weight percentage lower than 22%. a) SEM image of solution blow spun polymer network of low styrene content SIS (14 wt% styrene) after being swollen with 25% (wt/vol) STFA solution, showing loss of fiber morphology. b) SEM image of the same polymer network after silver nanoparticle nucleation.

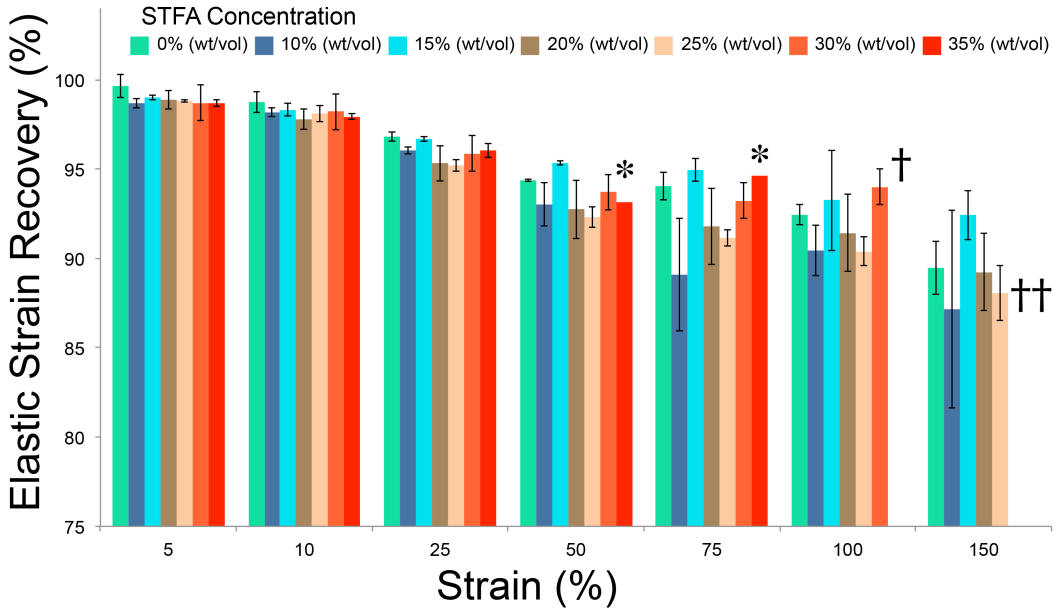

Figure B.3 Elastic recovery of SIS fiber mats and stretchable conductors fabricated from different precursor concentrations after consecutive strain cycling to increasing maximum strain values. (*) Indicates that 2 of 3 samples failed during that strain cycle for a specific experimental group. (†) Indicates that all of the samples have failed. (n=3) for all groups, error bars represent standard deviation.

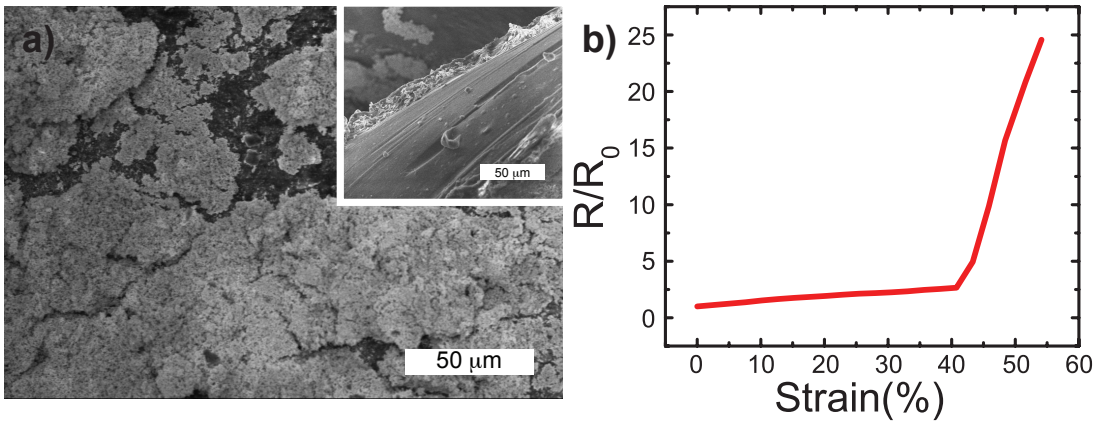

Figure B.4 a) SEM image of a drop cast SIS film nucleated with 25% (wt/vol) STFA solution (SEM image of cross section-inset). Silver nanoparticles were only formed on the outer surface of the film in a similar manner to individual SIS fibers. b) Normalized resistance values versus strain for polymer film silver nanoparticle composites.

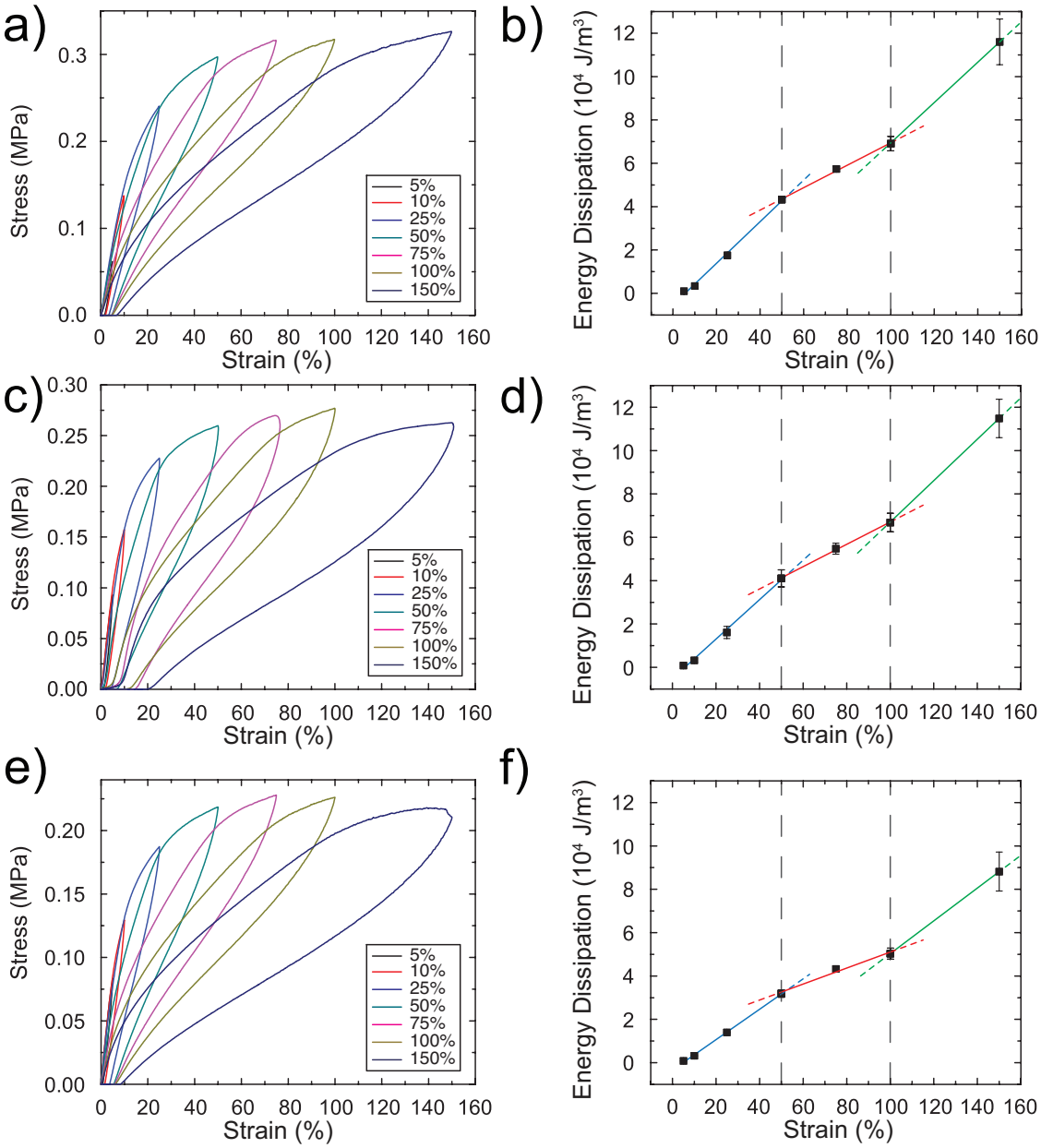

Figure B.5 a,c,e) Stress/strain cycling curves and b,d,f) energy dissipation values and corresponding linear fits for stretchable conductors fabricated with 10%, 15%, and 20% (wt/vol) STFA solution, respectively (n=3). Error bars represent standard deviation. Linear correlations relating energy dissipation to strain describe different regions of strain induced structural changes (blue, red, and green lines).

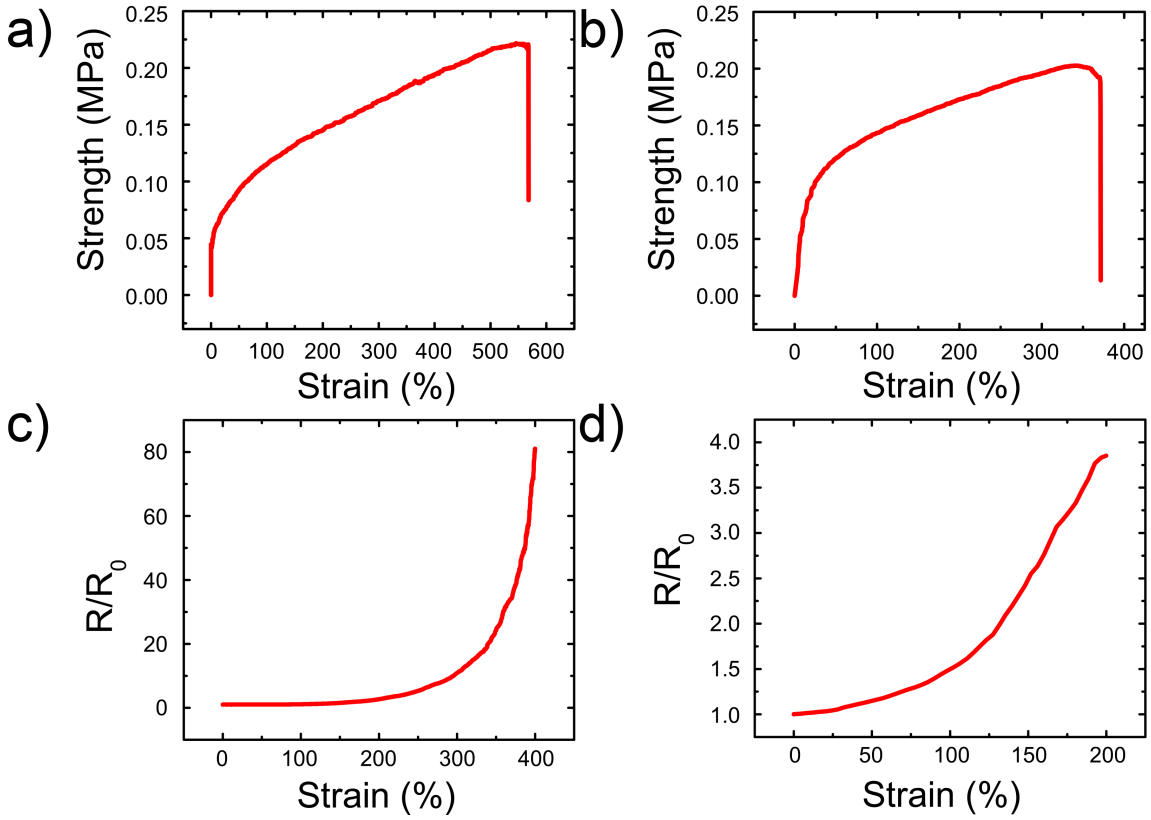

Figure B.6 Stress/strain curves for a) elastomeric fiber mats, b) conductive composites fabricated with 25% (wt/vol) solutions. Normalized resistance values of c) bulk and d) line patterns of conductive composites fabricated with 25% (wt/vol) STFA solutions. The bulk conductors failed between 370% and 400% strain, remaining conductive until mechanical failure.

Appendix C: Solution-Processed Elastic Conductors with Dual Nanoparticle Networks

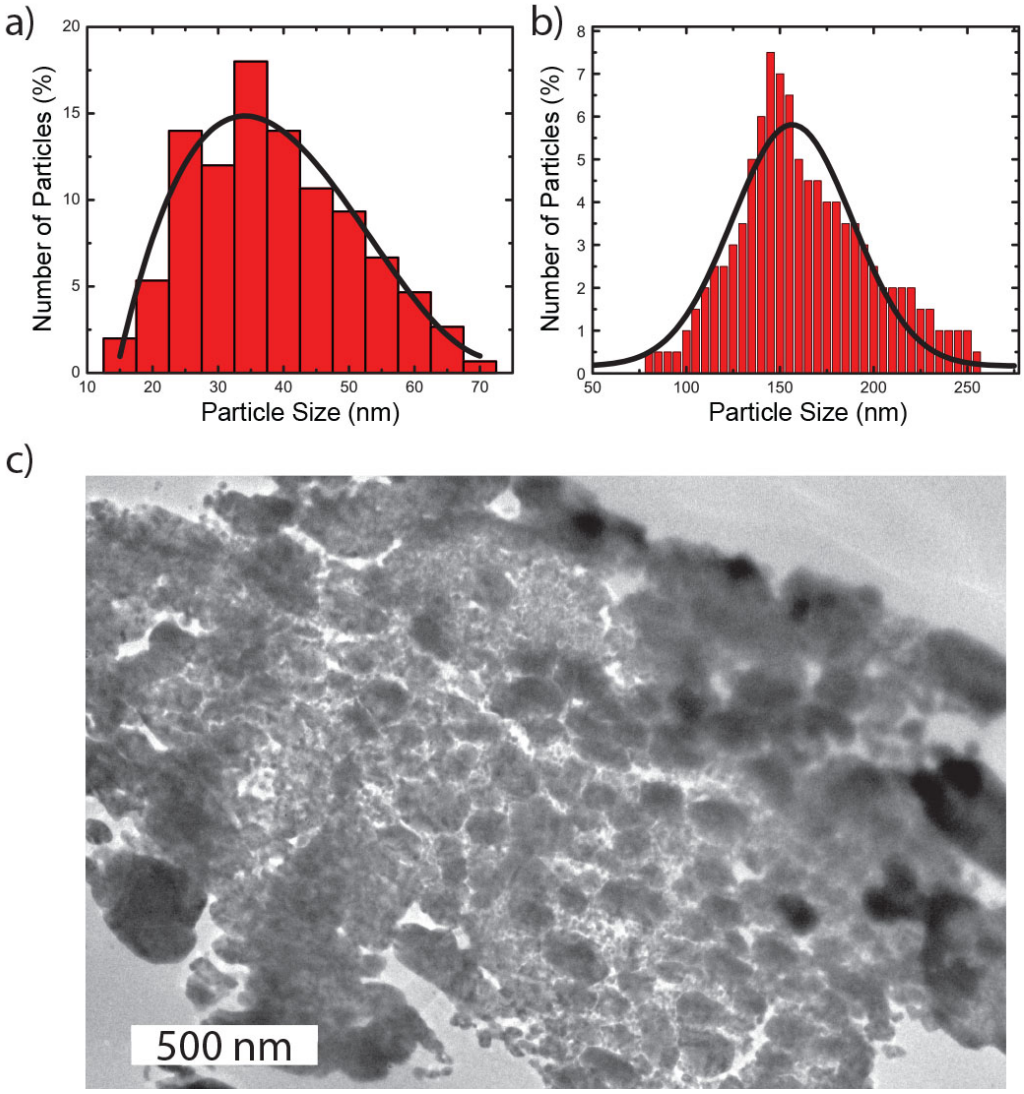

Figure C.1 Nanoparticle size distributions of elastic conductors prepared a) Ag-PAA and b) with Ag-PAA (35% (wt/vol) in spinning solution) as measured from cross-section TEM images (n=150). For elastic conductors with Ag-PAA, only the size distribution of large Ag-PAA nanoparticles was identified due to densely packed silver nanoparticle assembly. c) High resolution TEM image of stretchable conductors prepared with Ag-PAA (35% (wt/vol) in spinning solution).

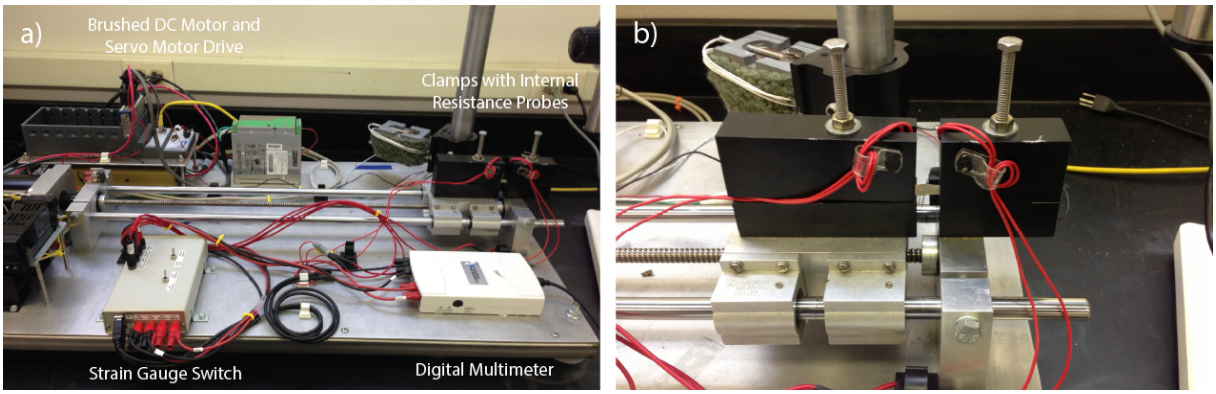

Figure C.2: a) Home-made system for measuring electrical resistance of materials under controlled strain. b) Clamps applying strain while measuring electrical resistance using a 4 point-probe configuration.

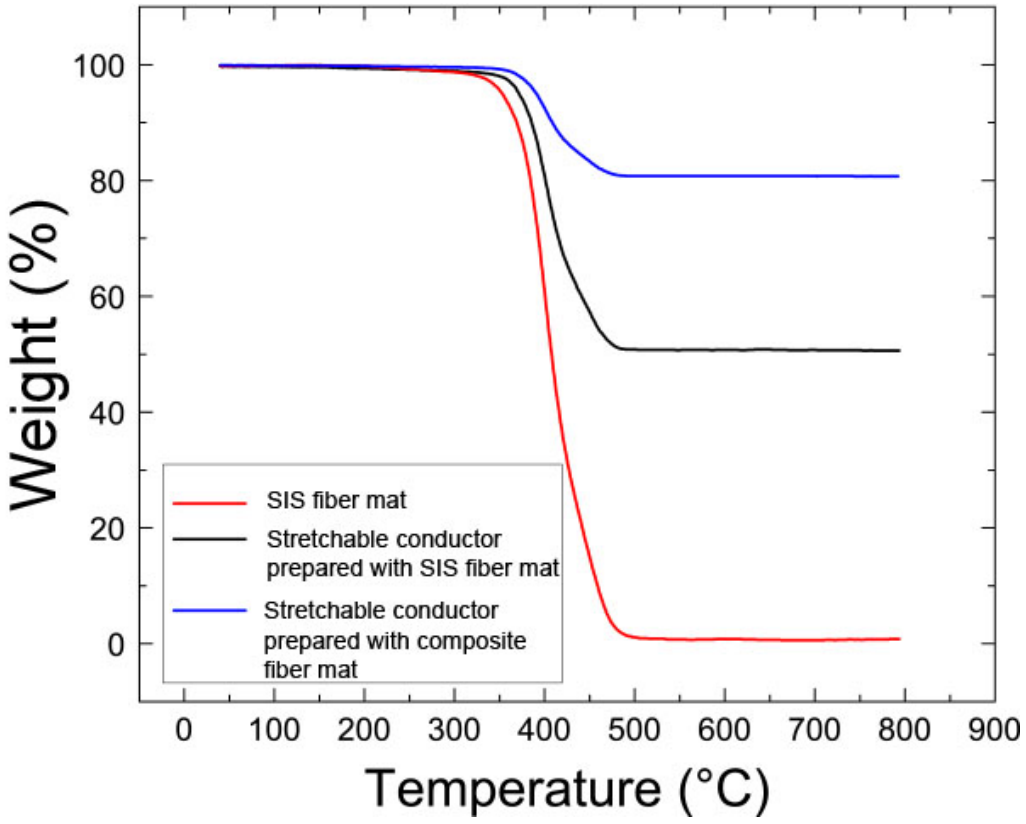

Figure C.3: Thermal gravimetric analysis (TGA) of block copolymer (SIS) fiber mat, elastic conductors prepared without Ag-PAA and with Ag-PAA (35% (wt/vol) in spinning solution).

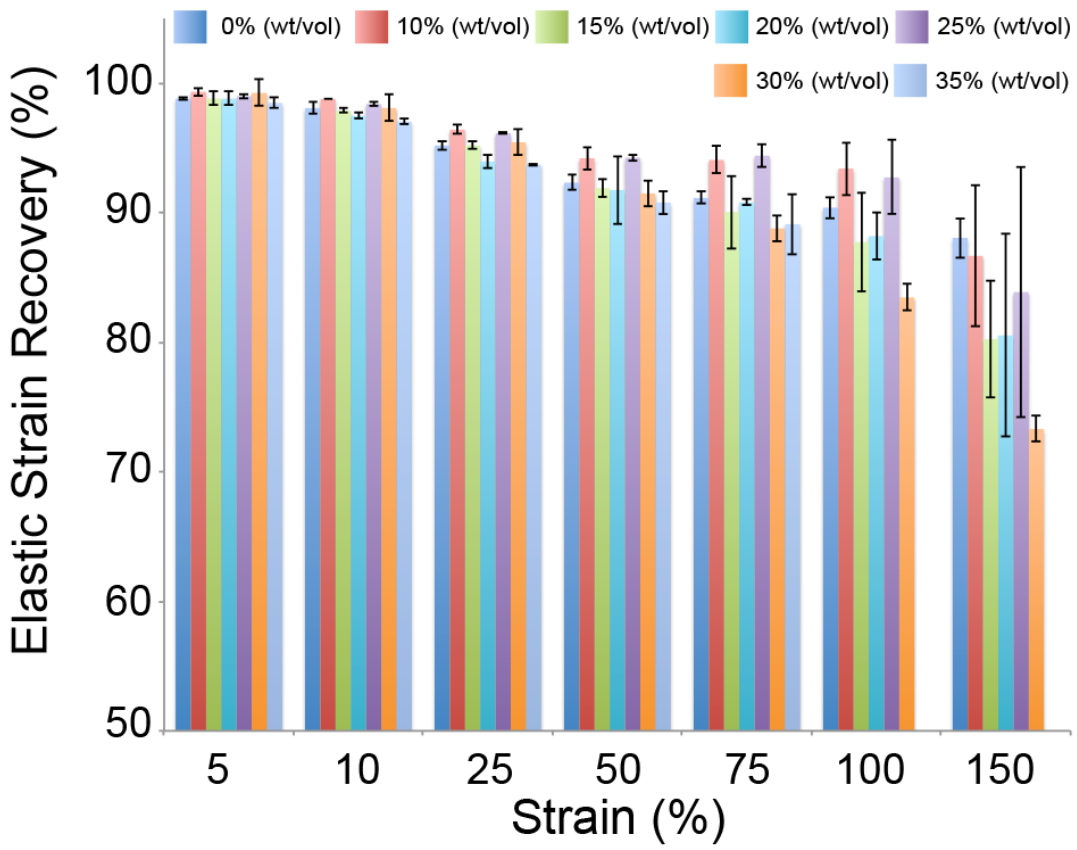

Figure C.4: Elastic recovery of elastic conductors fabricated from block copolymer fiber mat (0%), and composite mats prepared from spinning solutions with different Ag-PAA concentrations after consecutive strain cycling to increasing maximum strain values. (n=3) for all groups, error bars represent standard deviation.

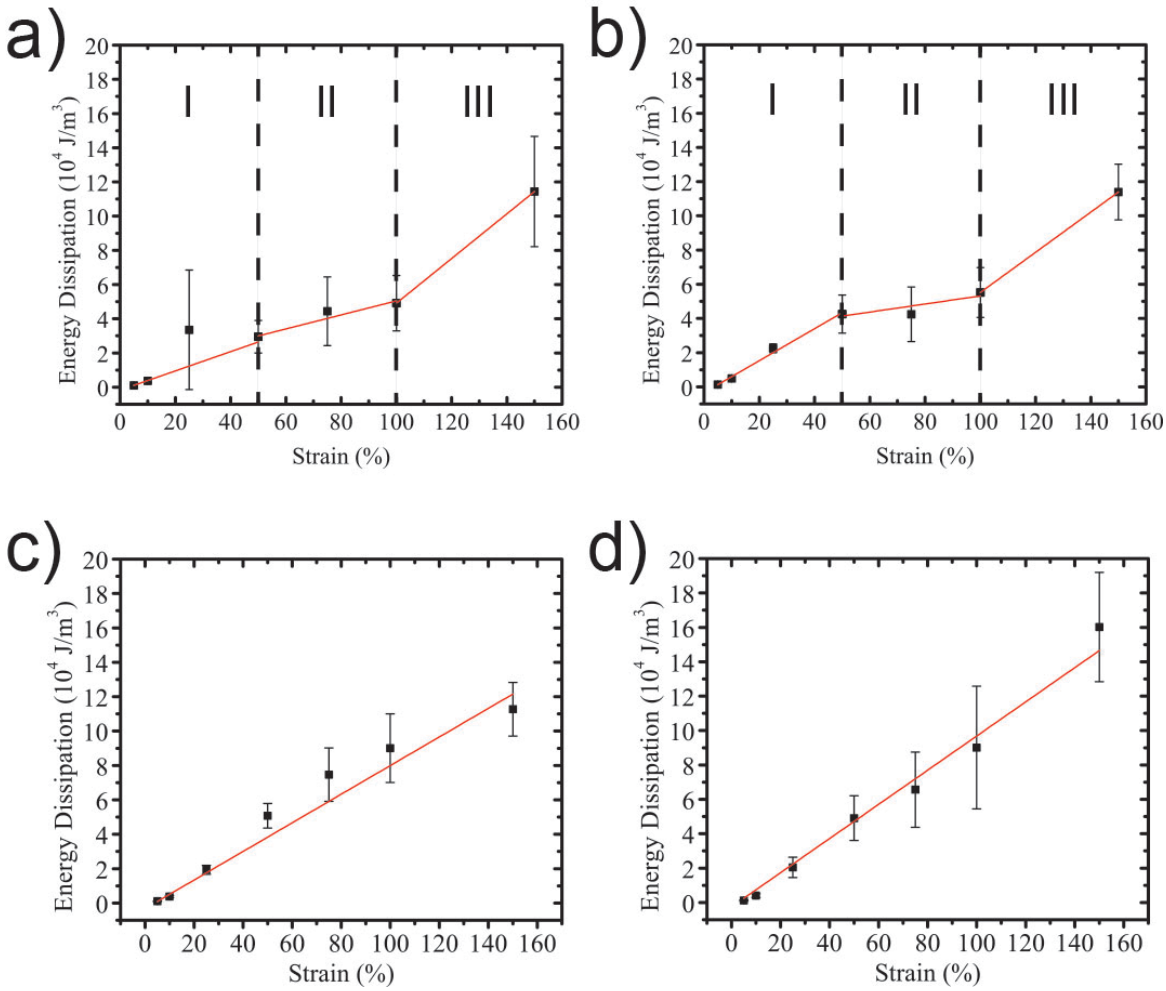

Figure C.5: Average energy dissipation values and corresponding linear fits for elastic conductors prepared from spinning solutions with a) 15% (wt/vol), b) 20% (wt/vol), 25% (wt/vol), and 30% (wt/vol) Ag-PAA concentration. (n=3) for energy dissipation data, error bars represent standard deviation.

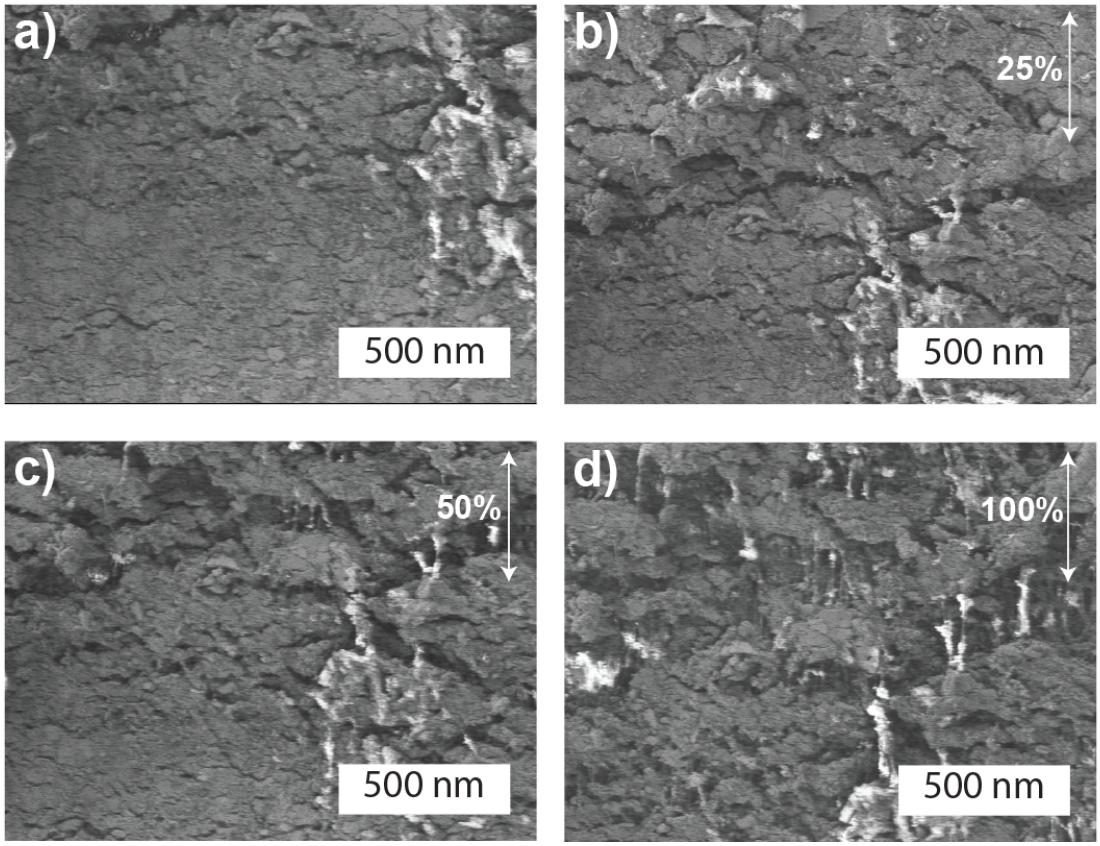

Figure C.6: Low magnification SEM images of elastic conductors prepared from spinning solutions with 35% (wt/vol) Ag-PAA concentration under a) 0% strain, b) 25% strain, c) 50% strain, and d) 100% strain. The arrows indicate the direction of uniaxial tensile strain.

Bibliography

1. A. O. Karilainen, P. M. T. Ikonen, C. R. Simovski and S. A. Tretyakov, *Ieee T Antenn Propag*, 2011, **59**, 3991-3998.
2. J. L. Wilson, P. Poddar, N. A. Frey, H. Srikanth, K. Mohomed, J. P. Harmon, S. Kotha and J. Wachsmuth, *J Appl Phys*, 2004, **95**, 1439-1443.
3. L. Z. Wu, J. Ding, H. B. Jiang, L. F. Chen and C. K. Ong, *J Magn Magn Mater*, 2005, **285**, 233-239.
4. R. Dosoudil, M. Usakova, J. Franek, J. Slama and V. Olah, *J Magn Magn Mater*, 2006, **304**, E755-E757.
5. T. I. Yang, R. N. C. Brown, L. C. Kempel and P. Kofinas, *J Magn Magn Mater*, 2008, **320**, 2714-2720.
6. C. Morales, J. Dewdney, S. Pal, K. Stojak, H. Srikanth, J. Wang and T. Weller, *Ieee Mtt S Int Micr*, 2010.
7. W. S. Wong and A. Salleo, *Journal*, 2008.
8. Z. N. Bao, Y. Feng, A. Dodabalapur, V. R. Raju and A. J. Lovinger, *Chem Mater*, 1997, **9**, 1299-&.
9. T. Sekitani, Y. Noguchi, K. Hata, T. Fukushima, T. Aida and T. Someya, *Science*, 2008, **321**, 1468-1472.
10. K. H. Kim, M. Vural and M. F. Islam, *Adv Mater*, 2011, **23**, 2865-+.
11. M. Park, J. Im, M. Shin, Y. Min, J. Park, H. Cho, S. Park, M. B. Shim, S. Jeon, D. Y. Chung, J. Bae, J. Park, U. Jeong and K. Kim, *Nat Nanotechnol*, 2012, **7**, 803-809.
12. J. Lee, H. Kwon, J. Seo, S. Shin, J. H. Koo, C. Pang, S. Son, J. H. Kim, Y. H. Jang, D. E. Kim and T. Lee, *Adv Mater*, 2015, **27**, 2433-2439.
13. N. Matsuhisa, M. Kaltenbrunner, T. Yokota, H. Jinno, K. Kuribara, T. Sekitani and T. Someya, *Nat Commun*, 2015, **6**.
14. R. Rahimi, M. Ochoa, W. Y. Yu and B. Ziaie, *Acs Appl Mater Inter*, 2015, **7**, 4463-4470.
15. D. H. Kim, N. S. Lu, R. Ma, Y. S. Kim, R. H. Kim, S. D. Wang, J. Wu, S. M. Won, H. Tao, A. Islam, K. J. Yu, T. I. Kim, R. Chowdhury, M. Ying, L. Z. Xu, M. Li, H. J. Chung, H. Keum, M. McCormick, P. Liu, Y. W. Zhang, F. G. Omenetto, Y. G. Huang, T. Coleman and J. A. Rogers, *Science*, 2011, **333**, 838-843.
16. D. H. Kim, J. Viventi, J. J. Amsden, J. L. Xiao, L. Vigeland, Y. S. Kim, J. A. Blanco, B. Panilaitis, E. S. Frechette, D. Contreras, D. L. Kaplan, F. G. Omenetto, Y. G. Huang, K. C. Hwang, M. R. Zakin, B. Litt and J. A. Rogers, *Nat Mater*, 2010, **9**, 511-517.
17. M. Kaltenbrunner, T. Sekitani, J. Reeder, T. Yokota, K. Kuribara, T. Tokuhara, M. Drack, R. Schwodiauer, I. Graz, S. Bauer-Gogonea, S. Bauer and T. Someya, *Nature*, 2013, **499**, 458-+.
18. M. Kaltenbrunner, G. Adam, E. D. Glowacki, M. Drack, R. Schwodiauer, L. Leonat, D. H. Apaydin, H. Groiss, M. C. Scharber, M. S. White, N. S. Sariciftci and S. Bauer, *Nat Mater*, 2015, **14**, 1032-+.

19. L. Z. Xu, S. R. Gutbrod, Y. J. Ma, A. Petrossians, Y. H. Liu, R. C. Webb, J. A. Fan, Z. J. Yang, R. X. Xu, J. J. Whalen, J. D. Weiland, Y. G. Huang, I. R. Efimov and J. A. Rogers, *Adv Mater*, 2015, **27**, 1731-+.
20. S. Xu, Y. H. Zhang, L. Jia, K. E. Mathewson, K. I. Jang, J. Kim, H. R. Fu, X. Huang, P. Chava, R. H. Wang, S. Bhole, L. Z. Wang, Y. J. Na, Y. Guan, M. Flavin, Z. S. Han, Y. G. Huang and J. A. Rogers, *Science*, 2014, **344**, 70-74.
21. S. C. B. Mannsfeld, B. C. K. Tee, R. M. Stoltenberg, C. V. H. H. Chen, S. Barman, B. V. O. Muir, A. N. Sokolov, C. Reese and Z. N. Bao, *Nat Mater*, 2010, **9**, 859-864.
22. T. Sekitani, H. Nakajima, H. Maeda, T. Fukushima, T. Aida, K. Hata and T. Someya, *Nat Mater*, 2009, **8**, 494-499.
23. J. A. Rogers, T. Someya and Y. G. Huang, *Science*, 2010, **327**, 1603-1607.
24. S. Borah and N. S. Bhattacharyya, *Compos Part B-Eng*, 2012, **43**, 1988-1994.
25. D. L. Huber, *Small*, 2005, **1**, 482-501.
26. X. Batlle, N. Perez, P. Guardia, O. Iglesias, A. Labarta, F. Bartolome, L. M. Garcia, J. Bartolome, A. G. Roca, M. P. Morales and C. J. Serna, *J Appl Phys*, 2011, **109**.
27. L. S. Schadler, S. K. Kumar, B. C. Benicewicz, S. L. Lewis and S. E. Harton, *Mrs Bull*, 2007, **32**, 335-340.
28. S. Merilampi, T. Bjorninen, V. Haukka, P. Ruuskanen, L. Ukkonen and L. Sydanheimo, *Microelectron Reliab*, 2010, **50**, 2001-2011.
29. M. Park, J. Park and U. Jeong, *Nano Today*, 2014, **9**, 244-260.
30. F. Dumestre, B. Chaudret, C. Amiens, P. Renaud and P. Fejes, *Science*, 2004, **303**, 821-823.
31. L. M. Lacroix, S. Lachaize, A. Falqui, M. Respaud and B. Chaudret, *J Am Chem Soc*, 2009, **131**, 549-557.
32. S. Gong, W. Schwalb, Y. W. Wang, Y. Chen, Y. Tang, J. Si, B. Shirinzadeh and W. L. Cheng, *Nat Commun*, 2014, **5**.
33. M. Amjadi, A. Pichitpajongkit, S. Lee, S. Ryu and I. Park, *Acs Nano*, 2014, **8**, 5154-5163.
34. S. Torquato, S. Hyun and A. Donev, *Phys Rev Lett*, 2002, **89**.
35. S. O. Kasap, *Principles of electronic materials and devices*, McGraw-Hill, Boston, 3rd edn., 2006.
36. G. L. Bir and G. E. Pikus, *Symmetry and strain-induced effects in semiconductors*, Wiley, New York,, 1974.
37. J. Bardeen and W. Shockley, *Phys Rev*, 1950, **80**, 72-80.
38. Y. Kim, J. Zhu, B. Yeom, M. Di Prima, X. L. Su, J. G. Kim, S. J. Yoo, C. Uher and N. A. Kotov, *Nature*, 2013, **500**, 59-U77.
39. M. Kubo, X. F. Li, C. Kim, M. Hashimoto, B. J. Wiley, D. Ham and G. M. Whitesides, *Adv Mater*, 2010, **22**, 2749-+.
40. J. Li and J. K. Kim, *Compos Sci Technol*, 2007, **67**, 2114-2120.
41. R. L. Crabb and F. C. Treble, *Nature*, 1967, **213**, 1223-&.
42. K. A. Ray, *Ieee T Aero Elec Sys*, 1967, **Aes3**, 107-&.
43. Z. F. Liu, S. Fang, F. A. Moura, J. N. Ding, N. Jiang, J. Di, M. Zhang, X. Lepro, D. S. Galvao, C. S. Haines, N. Y. Yuan, S. G. Yin, D. W. Lee, R. Wang, H. Y. Wang, W. Lv, C. Dong, R. C. Zhang, M. J. Chen, Q. Yin, Y. T. Chong, R.

Zhang, X. Wang, M. D. Lima, R. Ovalle-Robles, D. Qian, H. Lu and R. H. Baughman, *Science*, 2015, **349**, 400-404.
44. T. I. Yang, R. N. C. Brown, L. CKempel and P. Kofinas, *Nanotechnology*, 2011, **22**.
45. L. N. Song, A. C. Myers, J. J. Adams and Y. Zhu, *Acs Appl Mater Inter*, 2014, **6**, 4248-4253.
46. H. L. Yuan, Y. Q. Wang, S. M. Zhou and S. Y. Lou, *Chem Eng J*, 2011, **175**, 555-560.
47. Z. Guo, S. E. Lee, H. Kim, S. Park, H. T. Hahn, A. B. Karki and D. P. Young, *Acta Mater*, 2009, **57**, 267-277.
48. A. Demortiere, P. Panissod, B. P. Pichon, G. Pourroy, D. Guillon, B. Donnio and S. Begin-Colin, *Nanoscale*, 2011, **3**, 225-232.
49. J. S. Salazar, L. Perez, O. de Abril, T. P. Lai, D. Ihiawakrim, M. Vazquez, J. M. Greneche, S. Begin-Colin and G. Pourroy, *Chem Mater*, 2011, **23**, 1379-1386.
50. F. E. Luborsky, *J Appl Phys*, 1961, **32**, S171-&.
51. A. S. Edelstein and R. C. Cammarata, *Nanomaterials : synthesis, properties, and applications*, Institute of Physics Pub., Bristol ; Philadelphia, 1996.
52. H. B. Xia, P. Foo and J. B. Yi, *Chem Mater*, 2009, **21**, 2442-2451.
53. S. H. Xuan, Y. X. J. Wang, J. C. Yu and K. C. F. Leung, *Chem Mater*, 2009, **21**, 5079-5087.
54. A. S. Edelstein, B. N. Das, R. L. Holtz, N. C. Koon, M. Rubinstein, S. A. Wolf and K. E. Kihlstrom, *J Appl Phys*, 1987, **61**, 3320-3322.
55. J. M. D. Coey and Khalafal.D, *Phys Status Solidi A*, 1972, **11**, 229-&.
56. E. F. Kneller and F. E. Luborsky, *J Appl Phys*, 1963, **34**, 656-&.
57. S. Gangopadhyay, G. C. Hadjipanayis, B. Dale, C. M. Sorensen, K. J. Klabunde, V. Papaefthymiou and A. Kostikas, *Phys Rev B*, 1992, **45**, 9778-9787.
58. M. E. Schabes, *J Magn Magn Mater*, 1991, **95**, 249-288.
59. Y. W. Du, J. Wu, H. X. Lu, T. X. Wang, Z. Q. Qiu, H. Tang and J. C. Walker, *J Appl Phys*, 1987, **61**, 3314-3316.
60. K. Haneda and A. H. Morrish, *Nature*, 1979, **282**, 186-188.
61. T. J. Daou, G. Pourroy, S. Begin-Colin, J. M. Greneche, C. Ulhaq-Bouillet, P. Legare, P. Bernhardt, C. Leuvrey and G. Rogez, *Chem Mater*, 2006, **18**, 4399-4404.
62. M. Fang, V. Strom, R. T. Olsson, L. Belova and K. V. Rao, *Nanotechnology*, 2012, **23**.
63. T. J. Daou, J. M. Greneche, S. J. Lee, S. Lee, C. Lefevre, S. Begin-Colin and G. Pourroy, *J Phys Chem C*, 2010, **114**, 8794-8799.
64. W. Baaziz, B. P. Pichon, S. Fleutot, Y. Liu, C. Lefevre, J. M. Greneche, M. Toumi, T. Mhiri and S. Begin-Colin, *J Phys Chem C*, 2014, **118**, 3795-3810.
65. L. Lartigue, P. Hugounenq, D. Alloyeau, S. P. Clarke, M. Levy, J. C. Bacri, R. Bazzi, D. F. Brougham, C. Wilhelm and F. Gazeau, *Acs Nano*, 2012, **6**, 10935-10949.
66. O. Gerber, B. P. Pichon, C. Ulhaq, J. M. Greneche, C. Lefevre, I. Florea, O. Ersen, D. Begin, S. Lemonnier, E. Barraud and S. Begin-Colin, *J Phys Chem C*, 2015, **119**, 24665-24673.

67. P. Hu, L. J. Yu, A. H. Zuo, C. Y. Guo and F. L. Yuan, *J Phys Chem C*, 2009, **113**, 900-906.
68. H. C. Ko, M. P. Stoykovich, J. Z. Song, V. Malyarchuk, W. M. Choi, C. J. Yu, J. B. Geddes, J. L. Xiao, S. D. Wang, Y. G. Huang and J. A. Rogers, *Nature*, 2008, **454**, 748-753.
69. J. Park, S. D. Wang, M. Li, C. Ahn, J. K. Hyun, D. S. Kim, D. K. Kim, J. A. Rogers, Y. G. Huang and S. Jeon, *Nat Commun*, 2012, **3**.
70. S. Zhu, J. H. So, R. Mays, S. Desai, W. R. Barnes, B. Pourdeyhimi and M. D. Dickey, *Adv Funct Mater*, 2013, **23**, 2308-2314.
71. E. Palleau, S. Reece, S. C. Desai, M. E. Smith and M. D. Dickey, *Adv Mater*, 2013, **25**, 1589-1592.
72. M. D. Dickey, R. C. Chiechi, R. J. Larsen, E. A. Weiss, D. A. Weitz and G. M. Whitesides, *Adv Funct Mater*, 2008, **18**, 1097-1104.
73. T. S. Kasirga, Y. N. Ertas and M. Bayindir, *Appl Phys Lett*, 2009, **95**.
74. C. Dagdeviren, Y. W. Su, P. Joe, R. Yona, Y. H. Liu, Y. S. Kim, Y. A. Huang, A. R. Damadoran, J. Xia, L. W. Martin, Y. G. Huang and J. A. Rogers, *Nat Commun*, 2014, **5**.
75. C. Dagdeviren, Y. Shi, P. Joe, R. Ghaffari, G. Balooch, K. Usgaonkar, O. Gur, P. L. Tran, J. R. Crosby, M. Meyer, Y. W. Su, R. C. Webb, A. S. Tedesco, M. J. Slepian, Y. G. Huang and J. A. Rogers, *Nat Mater*, 2015, **14**, 728-+.
76. J. A. Fan, W. H. Yeo, Y. W. Su, Y. Hattori, W. Lee, S. Y. Jung, Y. H. Zhang, Z. J. Liu, H. Y. Cheng, L. Falgout, M. Bajema, T. Coleman, D. Gregoire, R. J. Larsen, Y. G. Huang and J. A. Rogers, *Nat Commun*, 2014, **5**.
77. B. Y. Ahn, E. B. Duoss, M. J. Motala, X. Y. Guo, S. I. Park, Y. J. Xiong, J. Yoon, R. G. Nuzzo, J. A. Rogers and J. A. Lewis, *Science*, 2009, **323**, 1590-1593.
78. J. Xiao, A. Carlson, Z. J. Liu, Y. Huang and J. A. Rogers, *J Appl Mech-T Asme*, 2010, **77**.
79. Z. W. Li, Y. Wang and J. L. Xiao, *Curr Opin Solid St M*, 2015, **19**, 171-189.
80. J. Li, P. C. Ma, W. S. Chow, C. K. To, B. Z. Tang and J. K. Kim, *Adv Funct Mater*, 2007, **17**, 3207-3215.
81. S. F. Wang and A. A. Ogale, *Compos Sci Technol*, 1993, **46**, 93-103.
82. S. S. Yao and Y. Zhu, *Adv Mater*, 2015, **27**, 1480-1511.
83. V. Mittal, J. K. Kim, K. Pal and SpringerLink (Online service), *Journal*, VIII, 388 p.
84. D. C. Hyun, M. Park, C. Park, B. Kim, Y. Xia, J. H. Hur, J. M. Kim, J. J. Park and U. Jeong, *Adv Mater*, 2011, **23**, 2946-+.
85. M. Vural, B. Crowgey, L. C. Kempel and P. Kofinas, *J Mater Chem C*, 2014, **2**, 756-763.
86. M. Vural, A. M. Behrens, O. B. Ayyub, J. J. Ayoub and P. Kofinas, *Acs Nano*, 2015, **9**, 336-344.
87. J. L. Snoek, *Physica*, 1948, **14**, 207-217.
88. B. D. Cullity and C. D. Graham, *Introduction to Magnetic Materials*, Hoboken: Wiley, 2009.
89. A. Caprile, M. Coisson, F. Fiorillo, P. Kabos, O. M. Manu, E. S. Olivetti, M. A. Olariu, M. Pasquale and V. A. Scarlatache, *Ieee T Magn*, 2012, **48**, 3394-3397.

90. Y. Shirakata, N. Hidaka, M. Ishitsuka, A. Teramoto and T. Ohmi, *Ieee T Magn*, 2008, **44**, 2100-2106.
91. C. Morales, J. Dewdney, S. Pal, S. Skidmore, K. Stojak, H. Srikanth, T. Weller and J. Wang, *Ieee T Microw Theory*, 2011, **59**, 302-310.
92. T. I. Yang, R. N. C. Brown, L. C. Kempel and P. Kofinas, *J Nanopart Res*, 2010, **12**, 2967-2978.
93. L. Yang, L. J. Martin, D. Staiculescu, C. P. Wong and M. M. Tentzeris, *Ieee T Microw Theory*, 2008, **56**, 3223-3230.
94. Z. Zhang, F. Zhou and E. J. Lavernia, *Metall Mater Trans A*, 2003, **34A**, 1349-1355.
95. H. S. Lim, J. W. Oh, S. Y. Kim, M. J. Yoo, S. D. Park and W. S. Lee, *Chem Mater*, 2013, **25**, 3315-3319.
96. D. D. Sarma, P. K. Santra, S. Mukherjee and A. Nag, *Chem Mater*, 2013, **25**, 1222-1232.
97. S. H. Sun and H. Zeng, *J Am Chem Soc*, 2002, **124**, 8204-8205.
98. C. R. Vestal and Z. J. Zhang, *Nano Lett*, 2003, **3**, 1739-1743.
99. A. Goyal, A. Kumar, P. K. Patra, S. Mahendra, S. Tabatabaei, P. J. J. Alvarez, G. John and P. M. Ajayan, *Macromol Rapid Comm*, 2009, **30**, 1116-1122.
100. N. A. Frey, M. H. Phan, H. Srikanth, S. Srinath, C. Wang and S. Sun, *J Appl Phys*, 2009, **105**.
101. Y. Shen, Y. H. Lin and C. W. Nan, *Adv Funct Mater*, 2007, **17**, 2405-2410.
102. Y. Kim, J. Zhu, B. Yeom, M. Di Prima, X. L. Su, J. G. Kim, S. J. Yoo, C. Uher and N. A. Kotov, *Abstr Pap Am Chem S*, 2014, **248**.
103. A. C. Balazs, T. Emrick and T. P. Russell, *Science*, 2006, **314**, 1107-1110.
104. L. Qi, B. I. Lee, S. H. Chen, W. D. Samuels and G. J. Exarhos, *Adv Mater*, 2005, **17**, 1777-1781.
105. Y. Shen, Z. X. Yue, M. Li and C. W. Nan, *Adv Funct Mater*, 2005, **15**, 1100-1103.
106. R. Lebourgeois, C. LeFur, M. Labeyrie, M. Pate and J. P. Ganne, *J Magn Magn Mater*, 1996, **160**, 329-332.
107. N. N. Song, H. T. Yang, H. L. Liu, X. Ren, H. F. Ding, X. Q. Zhang and Z. H. Cheng, *Sci Rep-Uk*, 2013, **3**.
108. P. Tartaj, M. P. Morales, T. Gonzalez-Carreno, S. Veintemillas-Verdaguer and C. J. Serna, *Adv Mater*, 2011, **23**, 5243-5249.
109. H. Yun, X. Y. Liu, T. Paik, D. Palanisamy, J. Kim, W. D. Vogel, A. J. Viescas, J. Chen, G. C. Papaefthymiou, J. M. Kikkawa, M. G. Allen and C. B. Murray, *Acs Nano*, 2014, **8**, 12323-12337.
110. F. L. Wang, J. R. Liu, J. Kong, Z. J. Zhang, X. Z. Wang, M. Itoh and K. Machida, *J Mater Chem*, 2011, **21**, 4314-4320.
111. H. Deng, X. L. Li, Q. Peng, X. Wang, J. P. Chen and Y. D. Li, *Angew Chem Int Edit*, 2005, **44**, 2782-2785.
112. Y. F. Zhu, W. R. Zhao, H. R. Chen and J. L. Shi, *J Phys Chem C*, 2007, **111**, 5281-5285.
113. C. M. Cheng, F. J. Xu and H. C. Gu, *New J Chem*, 2011, **35**, 1072-1079.
114. C. M. Cheng, Y. H. Wen, X. F. Xu and H. C. Gu, *J Mater Chem*, 2009, **19**, 8782-8788.

115. M. H. Lin, H. L. Huang, Z. T. Liu, Y. J. Liu, J. B. Ge and Y. P. Fang, *Langmuir*, 2013, **29**, 15433-15441.
116. H. F. Liu, S. F. Ji, Y. Y. Zheng, M. Li and H. Yang, *Powder Technol*, 2013, **246**, 520-529.
117. K. M. Choi and J. A. Rogers, *J Am Chem Soc*, 2003, **125**, 4060-4061.
118. S. Y. Fu, X. Q. Feng, B. Lauke and Y. W. Mai, *Compos Part B-Eng*, 2008, **39**, 933-961.
119. Z. Bartczak, A. S. Argon, R. E. Cohen and M. Weinberg, *Polymer*, 1999, **40**, 2347-2365.
120. C. Brosseau, J. Ben Youssef, P. Talbot and A. M. Konn, *J Appl Phys*, 2003, **93**, 9243-9256.
121. C. Kittel, *Phys Rev*, 1948, **73**, 155-161.
122. A. M. Konn, P. Laurent, P. Talbot and M. Lefloch, *J Magn Magn Mater*, 1995, **140**, 367-368.
123. R. Aragon, *Phys Rev B*, 1992, **46**, 5334-5338.
124. D. J. Lipomi, B. C. K. Tee, M. Vosgueritchian and Z. N. Bao, *Adv Mater*, 2011, **23**, 1771-+.
125. D. Y. Khang, H. Q. Jiang, Y. Huang and J. A. Rogers, *Science*, 2006, **311**, 208-212.
126. T. Yamada, Y. Hayamizu, Y. Yamamoto, Y. Yomogida, A. Izadi-Najafabadi, D. N. Futaba and K. Hata, *Nat Nanotechnol*, 2011, **6**, 296-301.
127. D. J. Lipomi, M. Vosgueritchian, B. C. K. Tee, S. L. Hellstrom, J. A. Lee, C. H. Fox and Z. N. Bao, *Nat Nanotechnol*, 2011, **6**, 788-792.
128. S. Jung, J. H. Kim, J. Kim, S. Choi, J. Lee, I. Park, T. Hyeon and D. H. Kim, *Adv Mater*, 2014, **26**, 4825-+.
129. D. Son, J. Lee, S. Qiao, R. Ghaffari, J. Kim, J. E. Lee, C. Song, S. J. Kim, D. J. Lee, S. W. Jun, S. Yang, M. Park, J. Shin, K. Do, M. Lee, K. Kang, C. S. Hwang, N. S. Lu, T. Hyeon and D. H. Kim, *Nat Nanotechnol*, 2014, **9**, 397-404.
130. A. H. Najafabadi, A. Tamayol, N. Annabi, M. Ochoa, P. Mostafalu, M. Akbari, M. Nikkhah, R. Rahimi, M. R. Dokmeci, S. Sonkusale, B. Ziaie and A. Khademhosseini, *Adv Mater*, 2014, DOI: 10.1002/adma.201401537.
131. T. Sekitani and T. Someya, *Adv Mater*, 2010, **22**, 2228-2246.
132. K. H. Kim, M. Vural and M. F. Islam, *Adv Mater*, 2011, **23**, 2865-2869.
133. F. Xu and Y. Zhu, *Adv Mater*, 2012, **24**, 5117-5122.
134. Y. Tang, S. Gong, Y. Chen, L. W. Yap and W. L. Cheng, *Acs Nano*, 2014, **8**, 5707-5714.
135. J. T. Muth, D. M. Vogt, R. L. Truby, Y. Menguc, D. B. Kolesky, R. J. Wood and J. A. Lewis, *Adv Mater*, 2014, DOI: 10.1002/adma.201400334.
136. N. Bowden, S. Brittain, A. G. Evans, J. W. Hutchinson and G. M. Whitesides, *Nature*, 1998, **393**, 146-149.
137. P. Lee, J. Lee, H. Lee, J. Yeo, S. Hong, K. H. Nam, D. Lee, S. S. Lee and S. H. Ko, *Adv Mater*, 2012, **24**, 3326-3332.
138. R. S. Guo, Y. Yu, Z. Xie, X. Q. Liu, X. C. Zhou, Y. F. Gao, Z. L. Liu, F. Zhou, Y. Yang and Z. J. Zheng, *Adv Mater*, 2013, **25**, 3343-3350.
139. K. Y. Chun, Y. Oh, J. Rho, J. H. Ahn, Y. J. Kim, H. R. Choi and S. Baik, *Nat Nanotechnol*, 2010, **5**, 853-857.

140. L. B. Hu, M. Pasta, F. La Mantia, L. F. Cui, S. Jeong, H. D. Deshazer, J. W. Choi, S. M. Han and Y. Cui, *Nano Lett*, 2010, **10**, 708-714.
141. D. H. Kim, Y. S. Kim, J. Wu, Z. J. Liu, J. Z. Song, H. S. Kim, Y. G. Y. Huang, K. C. Hwang and J. A. Rogers, *Adv Mater*, 2009, **21**, 3703-+.
142. D. H. Kim, J. L. Xiao, J. Z. Song, Y. G. Huang and J. A. Rogers, *Adv Mater*, 2010, **22**, 2108-2124.
143. J. T. Kim, J. Pyo, J. Rho, J. H. Ahn, J. H. Je and G. Margaritondo, *Acs Macro Lett*, 2012, **1**, 375-379.
144. S. Chung, J. Lee, H. Song, S. Kim, J. Jeong and Y. Hong, *Appl Phys Lett*, 2011, **98**.
145. T. Takahashi, K. Takei, A. G. Gillies, R. S. Fearing and A. Javey, *Nano Lett*, 2011, **11**, 5408-5413.
146. G. A. Salvatore, N. Munzenrieder, T. Kinkeldei, L. Petti, C. Zysset, I. Strebel, L. Buthe and G. Troster, *Nature communications*, 2014, **5**.
147. E. S. Medeiros, G. M. Glenn, A. P. Klamczynski, W. J. Orts and L. H. C. Mattoso, *J Appl Polym Sci*, 2009, **113**, 2322-2330.
148. W. Tutak, S. Sarkar, S. Lin-Gibson, T. M. Farooque, G. Jyotsnendu, D. B. Wang, J. Kohn, D. Bolikal and C. G. Simon, *Biomaterials*, 2013, **34**, 2389-2398.
149. A. M. Behrens, B. J. Casey, M. J. Sikorski, K. L. Wu, W. Tutak, A. D. Sandler and P. Kofinas, *Acs Macro Lett*, 2014, **3**, 249-254.
150. S. Srinivasan, S. S. Chhatre, J. M. Mabry, R. E. Cohen and G. H. McKinley, *Polymer*, 2011, **52**, 3209-3218.
151. B. Nikolova-Damyanova, *J Chromatogr A*, 2009, **1216**, 1815-1824.
152. G. D. Moon, G. H. Lim, J. H. Song, M. Shin, T. Yu, B. Lim and U. Jeong, *Adv Mater*, 2013, **25**, 2707-2712.
153. K. H. Lee, H. Y. Kim, Y. J. Ryu, K. W. Kim and S. W. Choi, *J Polym Sci Pol Phys*, 2003, **41**, 1256-1262.
154. K. Lee, B. Lee, C. Kim, H. Kim, K. Kim and C. Nah, *Macromol Res*, 2005, **13**, 441-445.
155. J. M. Widmaier and G. C. Meyer, *Polymer*, 1977, **18**, 587-590.
156. D. J. Kim, H. J. Kim and G. H. Yoon, *Int J Adhes Adhes*, 2005, **25**, 288-295.
157. C. Creton, G. J. Hu, F. Deplace, L. Morgret and K. R. Shull, *Macromolecules*, 2009, **42**, 7605-7615.
158. K. Fukatsu, *J Appl Polym Sci*, 1992, **45**, 2037-2042.
159. L. Hu, M. Pasta, F. L. Mantia, L. Cui, S. Jeong, H. D. Deshazer, J. W. Choi, S. M. Han and Y. Cui, *Nano letters*, 2010, **10**, 708-714.
160. S. Xu, Y. Zhang, J. Cho, J. Lee, X. Huang, L. Jia, J. A. Fan, Y. Su, J. Su, H. Zhang, H. Cheng, B. Lu, C. Yu, C. Chuang, T. I. Kim, T. Song, K. Shigeta, S. Kang, C. Dagdeviren, I. Petrov, P. V. Braun, Y. Huang, U. Paik and J. A. Rogers, *Nat Commun*, 2013, **4**, 1543.
161. S. Lee, S. Shin, S. Lee, J. Seo, J. Lee, S. Son, H. J. Cho, H. Algadi, S. Al-Sayari, D. E. Kim and T. Lee, *Adv Funct Mater*, 2015, **25**, 3114-3121.
162. F. Xu and Y. Zhu, *Adv Mater*, 2012, **24**, 5117-5122.
163. D. H. Kim, J. Z. Song, W. M. Choi, H. S. Kim, R. H. Kim, Z. J. Liu, Y. Y. Huang, K. C. Hwang, Y. W. Zhang and J. A. Rogers, *P Natl Acad Sci USA*, 2008, **105**, 18675-18680.

164. A. Bagal, E. C. Dandley, J. J. Zhao, X. A. Zhang, C. J. Oldham, G. N. Parsons and C. H. Chang, *Mater Horiz*, 2015, **2**, 486-494.
165. R. Ma, J. Lee, D. Choi, H. Moon and S. Baik, *Nano letters*, 2014, **14**, 1944-1951.
166. A. M. Behrens, N. G. Lee, B. J. Casey, P. Srinivasan, M. J. Sikorski, J. L. Daristotle, A. D. Sandler and P. Kofinas, *Adv Mater*, 2015, DOI: 10.1002/adma.201503691.
167. T. Jamnongkan, R. Shirota, S. K. Sukumaran, M. Sugimoto and K. Koyama, *Polym Eng Sci*, 2014, **54**, 1969-1975.
168. P. Podsiadlo, A. K. Kaushik, E. M. Arruda, A. M. Waas, B. S. Shim, J. D. Xu, H. Nandivada, B. G. Pumplin, J. Lahann, A. Ramamoorthy and N. A. Kotov, *Science*, 2007, **318**, 80-83.
169. J. Diani, B. Fayolle and P. Gilormini, *Eur Polym J*, 2009, **45**, 601-612.
170. M. Kluppel and J. Schramm, *Macromol Theor Simul*, 2000, **9**, 742-754.
171. Y. Wang, J. M. Hu, Y. H. Lin and C. W. Nan, *Npg Asia Mater*, 2010, **2**, 61-68.
172. P. Martins and S. Lanceros-Mendez, *Adv Funct Mater*, 2013, **23**, 3371-3385.
173. D. Guyomar, D. F. Matei, B. Guiffard, Q. Le and R. Belouadah, *Mater Lett*, 2009, **63**, 611-613.
174. J. X. Zhang, J. Y. Dai, L. C. So, C. L. Sun, C. Y. Lo, S. W. Or and H. L. W. Chan, *J Appl Phys*, 2009, **105**.
175. G. Evans, G. V. Duong, M. J. Ingleson, Z. L. Xu, J. T. A. Jones, Y. Z. Khimyak, J. B. Claridge and M. J. Rosseinsky, *Adv Funct Mater*, 2010, **20**, 231-238.

Permissions